

# UNIVERSITY OF TWENTE.

SCIENCE AND TECHNOLOGY FACULTY (TNW)  
NANOBIOPHYSICS GROUP

---

**Translocation of the food-related amyloid  
fibrils hen egg-white lysozyme and  
 $\alpha$ -Synuclein in *in vitro* cell models  
of the epithelial intestinal barrier**

*For the evaluation of risks associated with amyloid fibrils*

---

Master thesis at the department of Biomedical Engineering  
University of Twente

M.S. Doorn

May 20, 2021

---

**Graduation committee:**

Prof. dr. M.M.A.E. Claessens

Dr. C. Blum

Dr. A. Amanullah

Dr. K. Broersen

---



## Abstract

Amyloid fibrils are associated risks for the development of neurodegenerative diseases. Amyloid fibrils are not only naturally present in the human body, but are also found in food. Two amyloid fibril forming proteins found in food are the net positively charged hen egg-white lysozyme and  $\alpha$ -Synuclein, which is net negatively charged. Hen egg-white lysozyme and  $\alpha$ -Synuclein fibrils can cross-seed  $\alpha$ -Synuclein, present in for example neurons, which can lead to aggregation into amyloid fibrils. This makes exposure to fibrils of the food-related proteins a potential risk for neurodegenerative diseases if these fibrils find their way to the brain. For this research, the  $\alpha$ -Syn A53T variant of  $\alpha$ -Synuclein is used to model animal  $\alpha$ -Synuclein. The goal of this project was to examine the differences of lysozyme and  $\alpha$ -Syn A53T fibrils in permeability characteristics across *in vitro* cell models to evaluate the risk of amyloid fibril exposure. As a first step towards developing a methodology to quantify the permeability of the *in vitro* cell models of the epithelial intestinal barrier, polystyrene nanobeads were used.

The permeability of the *in vitro* cell model of the epithelial intestinal barrier to polystyrene nanobeads was quantified using Single Particle Tracking. Amyloid fibril length was analyzed using Atomic Force Microscopy. Quantification of amyloid fibrils was done using bulk fluorescence emission and Real-Time Quaking-induced Conversion (RT-QuIC). The latter was also used to differentiate between the presence of amyloid fibrils and monomers in the samples of the basolateral compartment of a Caco-2 model and the co-culture of Caco-2 and HT29MTX cells. With Fluorescence Correlation Spectroscopy (FCS), it was attempted to identify free dye and different sizes of lysozyme and  $\alpha$ -Syn A53T structures. With confocal microscopy, the location of the amyloid fibrils in the cell layers was examined and cytoskeletal remodelling due to the presence and uptake of the fibrils was examined.

The results showed that polystyrene nanobeads could permeate across the Caco-2 cell model, but this was only a very low amount of the total number of nanobeads. The PS nanobeads accumulated within the cytoplasm of the Caco-2 cells. The results showed that lysozyme fibrils could more easily permeate the cell models than  $\alpha$ -Syn A53T fibrils. However, it is expected that the basolateral samples contained mostly monomers, as there was no clear decrease of lag-time of the aggregation of  $\alpha$ -Synuclein wt monomers. Though, these results may be not reliable due to limitations of the RT-QuIC experiments. The FCS data suggests that there was probably no free dye present in the samples. In the basolateral samples, a relatively large species was found, which could be small fibrils, oligomers or proteins in the culture medium bound to labelled monomers. Internalization of lysozyme fibrils and remodelling of F-actin cortex was observed using confocal microscopy, while  $\alpha$ -Syn A53T fibrils seems to attach to the top side of the cell layer. This might be a possible explanation for the difference in permeability observed.

Altogether, the results of this research indicate that hen egg-white lysozyme, can cross the *in vitro* intestinal epithelial cell models used in this study more easily than  $\alpha$ -Syn A53T, which is used as a model for animal  $\alpha$ -Syn. This difference may be due to the charge difference, which can lead to different internalization properties. The exact nature of the permeated amyloid fibrils and the internalization mechanism should be further analyzed.

## Samenvatting

Amyloïde fibrillen worden geassocieerd met risico's voor de ontwikkeling van neurodegeneratieve ziekten. Amyloïden zijn niet alleen van nature aanwezig in het menselijk lichaam, maar komen ook voor in voedsel. Twee amyloïdvormende eiwitten die in voedsel worden aangetroffen, zijn lysozyme, afkomstig uit kippenwit en  $\alpha$ -synuclein. Lysozyme en  $\alpha$ -Synuclein-fibrillen kunnen met  $\alpha$ -Synuclein, aanwezig in bijvoorbeeld neuronen, aggregeren wat leidt tot formatie van amyloïde fibrillen. Dit maakt blootstelling aan fibrillen van de voedselgerelateerde eiwitten een potentieel risico voor neurodegeneratieve ziekten als deze fibrillen hun weg naar de hersenen vinden. Voor dit onderzoek wordt de A53T-variant van  $\alpha$ -Synuclein gebruikt om dierlijk  $\alpha$ -Synuclein te modelleren. Het doel van dit onderzoek was om de verschillen tussen lysozyme- en  $\alpha$ -Syn A53T-fibrillen te onderzoeken in mogelijkheid tot transport in *in vitro* cel-modellen om het risico van blootstelling aan amyloïden te evalueren. Als eerste stap in de ontwikkeling van een methodologie om de permeabiliteit van de *in vitro* celmodellen van de epitheliale darmbarrière te kwantificeren, werden polystyreen *nanobeads* gebruikt.

De permeabiliteit van het *in vitro* model van de epitheliale darmbarrière voor polystyreen *nanobeads* werd gekwantificeerd met behulp van *Single Particle Tracking*. De lengte van de amyloïde fibril werd geanalyseerd met behulp van *Atomic Force Microscopy*. Het kwantificeren van de concentratie van amyloïden werd uitgevoerd met behulp van bulk fluorescentie-emissie en *Real-Time Quaking-induced conversion*. Dit laatste werd ook gebruikt om onderscheid te maken tussen de aanwezigheid van fibrillen en monomeren in de basolaterale compartiment van een Caco-2-model en de co-kweek van Caco-2- en HT29MTX-cellen. Met *Fluorescence Correlation Spectroscopy* werd geprobeerd *free dye* en verschillende groottes lysozyme en  $\alpha$ -Syn A53T te identificeren. Met confocale microscopie werd de locatie van de amyloïde fibrillen in de cellen bepaald en werd de hermodellering van het cytoskelet door de aanwezigheid en opname van de fibrillen onderzocht.

De resultaten toonden aan dat polystyreen *nanobeads* door het Caco-2-model konden verplaatsen, maar dit was slechts een zeer kleine hoeveelheid van het totale aantal *nanobeads*. De PS *nanobeads* aggregeren in het cytoplasma van de cellen. De resultaten toonden aan dat lysozyme-fibrillen gemakkelijker de modellen konden doordringen dan  $\alpha$ -Syn A53T-fibrillen. De samples bevatten waarschijnlijk voornamelijk monomeren, aangezien er geen duidelijke afname van de *lag-time* van de aggregatie van  $\alpha$ -Synucleïne monomeren waargenomen is. Deze resultaten zijn echter mogelijk niet betrouwbaar vanwege beperkingen van de RT-QuIC-experimenten. De resultaten suggereren dat er waarschijnlijk geen *free dye* in de basolaterale compartiment aanwezig was. Internalisatie van lysozyme-fibrillen en hermodellering van F-actine cortex werden waargenomen.

Al met al, lijken de resultaten aan te tonen dat lysozyme, beter de *in vitro* intestinale epitheelmodellen kan passeren die in deze studie zijn gebruikt dan  $\alpha$ -Syn A53T, dat wordt gebruikt als een model voor dierlijk  $\alpha$ -Syn. Dit verschil kan te wijten zijn aan het ladingsverschil, dat tot verschillende internalisatie-eigenschappen kan leiden. De exacte aard van de amyloïden en het internalisatiemechanisme moeten verder worden geanalyseerd.

# Contents

<b>Abstract</b>	<b>2</b>
<b>Samenvatting</b>	<b>3</b>
<b>1 Introduction</b>	<b>7</b>
<b>2 Background</b>	<b>10</b>
2.1 Intestinal barrier . . . . .	10
2.1.1 Transport across epithelial cell barriers . . . . .	11
2.1.2 <i>In vitro</i> models of the intestinal epithelial cell barrier . . . . .	13
2.1.3 Evaluation of the <i>in vitro</i> cell models . . . . .	14
2.2 Amyloid fibrils . . . . .	16
2.2.1 Lysozyme . . . . .	17
2.2.2 $\alpha$ -Synuclein . . . . .	18
2.3 Principles of experimental methods . . . . .	19
2.3.1 Fluorescence . . . . .	19
2.3.2 Single Particle Tracking . . . . .	19
2.3.3 Real-Time Quaking-induced Conversion . . . . .	21
2.3.4 Atomic Force Microscopy . . . . .	23
<b>3 Methodology</b>	<b>24</b>
3.1 <i>In vitro</i> cell model of the intestinal epithelial barrier . . . . .	24
3.1.1 Cell culturing and seeding . . . . .	24
3.1.2 Monolayer integrity: Transepithelial Electrical Resistance . . . . .	24
3.1.3 Cell viability . . . . .	25
3.1.4 Fixation and Staining of the cells . . . . .	25
3.1.5 Confocal imaging . . . . .	26
3.2 Polystyrene nanobeads . . . . .	26
3.2.1 Single Particle Tracking . . . . .	26
3.2.2 Permeability . . . . .	27
3.3 Amyloid fibrils . . . . .	28
3.3.1 Aggregation and labelling . . . . .	28
3.3.2 Bulk fluorescence spectroscopy . . . . .	29
3.3.3 Real-Time Quaking-induced Conversion . . . . .	30
3.3.4 Atomic Force Microscopy . . . . .	31
3.3.5 Förster Resonance Energy Transfer . . . . .	31
3.3.6 Fluorescence Correlation Spectroscopy . . . . .	31
<b>4 Results and Discussion</b>	<b>33</b>
4.1 Polystyrene nanobeads . . . . .	33
4.1.1 Characterization and quantification . . . . .	33
4.1.2 Viability of Caco-2 cells during exposure to PS nanobeads . . . . .	35

---

4.1.3	Permeation of PS nanobeads through membranes with different pore sizes	36
4.1.4	Permeation of PS nanobeads through empty transwell membranes . . . . .	37
4.1.5	Permeation of PS nanobeads through the Caco-2 cell model . . . . .	40
4.1.6	Localization of the PS nanobeads in the Caco-2 cell layer . . . . .	43
4.1.7	Concluding remarks . . . . .	45
4.2	Amyloid fibrils . . . . .	46
4.2.1	Length and morphology of amyloid fibrils . . . . .	46
4.2.2	Cell layer integrity: Transepithelial Electrical Resistance . . . . .	48
4.2.3	Quantification of the concentration of amyloid fibrils . . . . .	52
4.2.4	Apparent permeability of amyloid fibrils in the Caco-2 and Caco-2+HT29MTX models . . . . .	55
4.2.5	Identification of amyloid fibrils and monomers in the basolateral samples .	59
4.2.6	Identification of free dye and lysozyme and $\alpha$ -Syn A53T species in the basolateral samples . . . . .	65
4.2.7	Internalization of amyloid fibrils by Caco-2 and HT29MTX cells . . . . .	68
4.2.8	Reorganization of cytoskeleton upon uptake of lysozyme fibrils . . . . .	72
<b>5</b>	<b>Conclusion</b>	<b>75</b>
<b>6</b>	<b>Recommendations</b>	<b>77</b>
	<b>Acknowledgements</b>	<b>79</b>
	<b>References</b>	<b>87</b>
	<b>Appendices</b>	<b>88</b>
	Appendix A: Sequence of $\alpha$ -Synuclein . . . . .	88
	Appendix B: Confluence of Caco-2 cell layer on different seeding days . . . . .	89
	Appendix C: Emission spectra lysozyme and $\alpha$ -Syn A53T fibrils . . . . .	90
	Appendix D: Excitation and emission spectra AF488 and AF647 . . . . .	91

## List of Abbreviations

$\alpha$ -Syn	$\alpha$ -Synuclein
$\alpha$ -Syn A53T	$\alpha$ -Synuclein variant with threonine at residue 53
AF	Alexa Fluor
Caco-2	Cancer coli-2 cell line
DMEM	Dulbecco's Modified Eagle Medium
DOL	Degree Of Labelling
FBS	Fetal Bovine Serum
HDR	High Dynamic Range imaging
HS	High Salt concentration
HSPG	Heparan Sulfate proteoglycan
HT29	Human colorectal adenocarcinoma cell line
LS	Low Salt concentration
MSD	Mean Square Displacement
MTX	Methotrexate
NAC	Non-Amyloidal Component
NaCl	Sodium Chloride
NaN <sub>3</sub>	Sodium azide
NEAA	Non-Essential Amino Acids
NHS	N-HydroxySuccinimide
NR	Nile Red
P/S	Penicillin-Streptomycin
PBS	Phosphate-Buffered Saline
PC	Polycarbonate
PFA	Paraformaldehyde
TJ	Tight Junction
wt	wild-type

## 1 Introduction

Protein molecules can adopt different conformational states between their synthesis and degradation within a living system. The conformational state of a protein does not only depend on its amino acid sequence but also the presence of molecular chaperones, the biological environment and degradation processes [1]. The native, or folded, state of a protein corresponds to the structure that is most thermodynamically stable. The shape into which the protein is folded is crucial for its function. For example, actin filaments provide mobility and shape to a cell by how they are assembled. Besides this, the folding and unfolding processes of proteins are functional for cellular activity, such as trafficking, secretion, immune response and regulation of the cell cycle [2]. Genetic mutations and oxidative stress are examples of processes that can cause misfolding of proteins, for example genetic mutations, translational errors or thermal or oxidative stress.

Misfolding of proteins can lead to different diseases. Some diseases result from the misfolded proteins not being able to exercise their function. In other cases, groups of proteins form aggregates within cells or the extracellular space [3]. An example of these proteins is amyloid fibrils. Amyloid fibrils are normally found in nature, playing a role in the host organism's survival [4]. However, they are also associated with different neurodegenerative diseases, such as Parkinson's Disease and Alzheimer's [1, 3, 5].

Amyloid fibrils are fibrillar structures containing cross- $\beta$ -sheets and are formed by a nucleation-dependent polymerization process [6]. Because of their fibrillar and stable structure, non-disease-related amyloid fibrils are often used in applications for (bio)nanotechnology. A few examples are nanowires [7], hydrogels for (stem) cell culture and networks for drug delivery [4]. Amyloid-forming-proteins and amyloid fibrils are also naturally present in food [8, 9, 10]. Two food-related amyloid fibril forming proteins are hen egg-white lysozyme and animal  $\alpha$ -Synuclein, present in pig, cow and fish among others [9, 11, 12]. In this study,  $\alpha$ -Synuclein with mutation A53T was used as a model for animal  $\alpha$ -Synuclein. In this mutation, alanine at residue 53 is replaced by threonine. *alpha*-Syn A53T fibrils, are directly related to the neurodegenerative disease Parkinson's [6].

Hen egg-white lysozyme, on the other hand, is in physiological conditions not dangerous to human health, but it can induce aggregation of disease-related amyloid fibrils and form a potential hazard [12]. The aggregation of the disease-related  $\alpha$ -Synuclein wild type (wt) monomers can be induced in the presence of lysozyme and  $\alpha$ -Syn A53T amyloid fibrils [12].  $\alpha$ -Syn wt monomers are abundant in several tissues in the human body, mainly in neuronal cells [13]. Amyloid fibrils formed by  $\alpha$ -Syn monomers can translocate via the vagus nerve to the brain, which was shown in animal studies [14]. This indicates that if lysozyme and  $\alpha$ -Syn A53T fibrils can pass biological barriers, they can be a potential risk to human health. Therefore, it is important to understand which properties of food-related amyloid fibrils determine the permeability characteristics across the biological barrier that protects the human body.

The most predominant barrier in the uptake for most substances is the luminal membrane in the gastrointestinal tract. After extensive research, no studies were found that have examined *in vitro* or *in vivo* transport of hen egg-white lysozyme and  $\alpha$ -Syn A53T across the intestinal barrier. However, several

transport studies of other amyloid fibrils or amyloid-forming proteins across epithelial barriers can be found in literature. Killinger et al. [9] summarize several routes of transport via which  $\alpha$ -Syn from food can infect a human host. It was found that M-cells, enterocytes and dendritic cells can actively absorb  $\alpha$ -Syn from the lumen. Furthermore, Bates et al. [15] have found that  $\alpha$ -Syn wt monomers can translocate across the blood-cerebrospinal fluid barrier, another epithelial cell barrier. Keaney et al. show that the paracellular pathway is involved in the transport of A $\beta$  monomers across the blood-brain-barrier. Amyloid- $\beta$  can enable enhanced movement by decreasing the levels of the tight junction-proteins claudin-5 and occludin [16].

Tight junctions form the intracellular barrier between cells to regulate the selective transport of substances across the barrier [17]. Kuan et al. found that the expression of tight junction proteins, such as ZO-1 and occludin can be down regulated by exposure to  $\alpha$ -Syn [18]. Puig et al. found that other types of amyloid fibrils, such as Amyloid- $\beta$  could decrease occludin levels in Caco-2 cells [19]. A decrease in occludin levels could disrupt the monolayer that is formed by tight junction complexes in between the cells. This indicates that amyloid fibrils can increase the permeability of epithelial layers by disruption of tight junction complexes. Next to this, it was found that it is possible for  $\alpha$ -Syn to penetrate mucus, in a hydrogel model containing gastric mucus [20]. Transport of  $\alpha$ -Syn molecules can also occur in porcine intestinal mucin [21]. Moreover, different types of amyloid fibrils can resist proteolysis. This implies that fibrils could remain intact when passing through the lumen in the intestines when fibril containing food is consumed [22]. This all leads to the hypothesis that it is possible for lysozyme and  $\alpha$ -Syn A53T to cross the intestinal cell barrier.

To study the permeability characteristics of amyloid fibrils, the concentration of the fibrils should be quantified. For the quantification, amyloid fibrils can be fluorescently labelled. However, it is difficult to quantify the concentration of amyloid fibrils in single particle methods, because amyloid fibrils are heterogeneous in size and have a tendency to cluster. The single particle quantification methods are usually limited, as the dynamic range of the camera should be broad enough to image large and small amyloid fibrils at the same time. Therefore, amyloid fibrils are not very suitable for the quantification using single particle methods. As a first step towards developing a methodology to quantify the permeability of the *in vitro* cell models of the epithelial intestinal barrier, the permeability of nanobeads was also tested in the first part of this research. Nanobeads are homogeneous in size, stable, easy to quantify and could be an indicator of substances that can cross the barrier.

Nanobeads are defined as spherical nanoparticles with a size between 1 and a few hundreds nanometers. Various materials are used for the production of nanobeads, such as metals and synthetic or natural polymers. Often, polystyrene (PS) nanobeads are used as they are available in a wide range of sizes. Furthermore, surface modifications are available to facilitate the coupling of various molecules and proteins to the surface of the nanobeads. Polystyrene nanobeads can be fluorescently stained which makes them easily quantifiable in single particle tracking methods or bulk fluorescence measurements.

In literature, PS nanobead uptake and translocation were measured for several types of (epithelial) barriers *in vitro*: pulmonary [23], placental [24] and blood-brain-barrier [25] models. In intestinal epithelial

cell models, the translocation of PS nanobeads has been examined for different cell models (mono-, co- and tri-culture), sizes of nanobeads and charges. Walczat et al. [26] have found that there was no significant difference between PS nanobead permeability in mono-, co- and tri-culture cell models with Caco-2, HT29MTX and M-cells. They did find that 50 nm PS beads translocated to a higher extent than 100 nm PS beads. PS beads without charge and negatively charged beads permeated more than positively charged PS beads. Bannanah et al. [27] et al. have found the same for 50 and 100 nm PS beads for a Caco-2 barrier. Domenech et al. tested whether PS nanobeads affect the permeability by measuring transepithelial Electrical Resistance and Lucifer Yellow transport after PS nanobeads exposure [28]. There was no cytotoxicity observed, and neither the integrity nor the permeability was affected by PS treatments. However, they did find that PS nanobeads of 50 and 200 nm are taken up by the cells and also permeate the barrier. More studies show that PS nanobeads are internalized but do not have a direct cytotoxic effect on the cells [29, 30]. Long-term effects, however, are not entirely known. Overall, it is believed that small and negatively charged PS nanobeads can transport efficiently across the intestinal barrier. This makes permeation of nanobeads a good preliminary experiment to test the single particle based quantification method.

To summarize, if food-related amyloid fibrils, such as lysozyme and  $\alpha$ -Syn fibrils, can cross the biological barrier that protects the human body, they can be a potential hazard for neurodegenerative diseases. The goal of this project was to examine whether lysozyme and  $\alpha$ -Syn A53T could translocate across *in vitro* cell models of the epithelial intestinal barrier to evaluate the risk of amyloid fibril exposure. Next to this, differences in permeability characteristics between the net positively charged lysozyme and net negatively charged  $\alpha$ -Syn will be examined. First, the permeability for PS nanobeads was determined as a preliminary model for the permeation of amyloid fibrils and to test the single particle quantification method.

## 2 Background

In this chapter, the background of this research is presented. First, an overview of the intestinal barrier, transport of substances across the epithelial cells and *in vitro* models of intestinal barriers are discussed. This is followed by a brief overview of amyloid fibril aggregation, amyloidogenic proteins like lysozyme and  $\alpha$ -Syn A53T and their associated risks. Finally, the principles of some experimental methods used in this research are explained in more detail.

### 2.1 Intestinal barrier

The gastrointestinal tract is part of the digestive system. The digestive system has three main functions: digestion of food, absorption of nutrients to the blood and elimination of solid food waste. The small and large intestines fulfil a major role in the gastrointestinal tract, especially in digestion and absorption of nutrients. The intestinal wall consists of four layers: mucosa, submucosa, muscular layer and adventitia, which are schematically depicted in Figure 2.1a.

The mucosa is an epithelial cell layer. The epithelial cell layer is not a straight layer but consists of crypts [33]. Enterocytes are the most abundant cell type in the mucosa: 80% of the cells are enterocytes. They have hair-like projections on the luminal side, called microvilli. Crypts and microvilli are depicted in Figure 2.1a. Microvilli increase the surface area that is available for absorption. Besides this, enterocytes form intracellular junction complexes which bind the cells together in a monolayer. Another major cell in the mucosa layer is goblet cells which produce and secrete mucus. Goblet cells comprise approximately 10% of the cells in the mucosa layer. Various other cell types in this layer are; M-cells, neuroendocrine cells and Paneth cells [33]. The different cells are depicted in Figure 2.1b. The mucosa layer absorbs useful substances, such as nutrients, but it also forms a barrier against harmful substances, such as pathogens and toxic foreign particles. As mentioned earlier, the goblet cells secrete mucus.

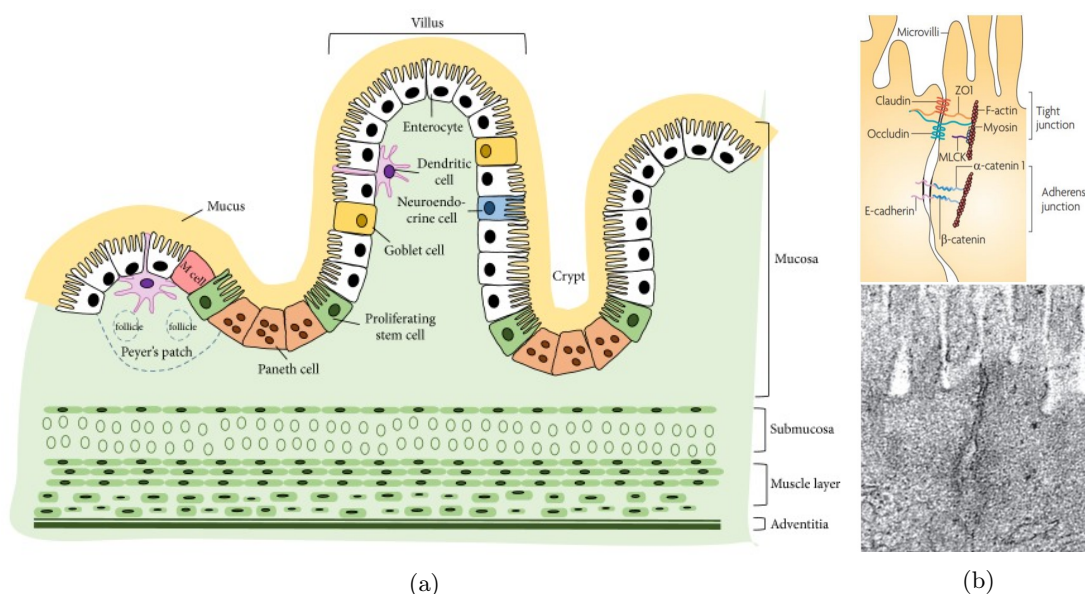


Figure 2.1: (a) Schematic representation of the cross-section of the intestinal barrier [31]. (b) An electron microscope image (bottom) of the junction complexes of intestinal epithelial cells and the corresponding schematic view (top) [32].

Mucus keeps the tissue moist and mucus is also a form of protection against harmful substances [31]. Mucus is a gel-like structure composed of water, ions, proteins and macromolecules. The major macromolecular component of mucus is the glycoprotein mucin [34].

Beneath the mucosa, the submucosa is located. The submucosa layer is a collagen-rich extracellular matrix and supports the mucosa. It contains blood vessels, nerves and lymphatics [35]. The submucosa joins the mucosa to the muscular layer, which is responsible for gut movement (peristalsis). Gut movement is necessary to propagate food in a forward direction. The outer layer is the adventitia, which consists of fibrous connective tissue [31].

### 2.1.1 Transport across epithelial cell barriers

There are two main distinct mechanisms for molecules to translocate across the intestinal epithelial barrier: the **paracellular** and **transcellular pathway** [36]. A third pathway can be found in pathological situations: the **unrestricted pathway** [37]. The type of transport depends on many characteristics of the substance, such as size, morphology, surface charge and hydrophobicity, and the potential to form (hydrogen) interactions [38].

**The paracellular pathway** is a passive route for molecules in which molecules move through the intercellular space of the intestinal cells. The pathway is restricted by tight junctions (TJ), positioned between the cells. The main function of TJ is to prevent the passage of molecules in-between cells. TJ-complexes allow only the passage of water, ions and small molecules [17]. All cells in the intestinal barrier are capable of forming TJ, but TJ-proteins are especially expressed in enterocytes. TJ form a complex of transmembrane proteins (e.g. occludins and claudins) and associated cytoplasmic proteins (e.g. zonula occludens proteins) that link the TJ to actin-filaments [17]. Figure 2.1b shows a simplified view of the most important TJ proteins. There are many more proteins involved in the TJ complexes [32, 39]. Figure 2.1b also shows adherens junctions. These are also strong adherent bonds, but their main function is intercellular interaction. Loss of adherens junctions can lead to disruption in the matrix, but also inefficient cell differentiation [32].

Within the paracellular pathway, there are two types of transport. The first route is the ‘pore pathway’ and is characterized by small pores that are defined by claudin associated proteins. The size of the pores is approximately 0.4 nm [32]. The second route is the ‘leaky pathway’. This allows larger particles to cross the intestinal barrier. The size of particles for this route is not precisely defined but the maximum size of particles is thought to be in the range of 10-20 nm [32, 39, 40]. There are several ideas proposed to explain the existence of the leaky pathway. The first is the loss of occludin and claudins. This is not necessarily pathological. Another possibility is that larger molecules can cross the TJ is a stepwise matter by temporary separation of the connections between TJ-proteins in the TJ-complex [41].

**Transcellular transport** occurs by transepytosis, a process in which substances are taken up by the cells by endocytosis and secreted by exocytosis. The transport occurs from the luminal (apical) side to the extracellular fluid (basolateral). The main function of transcellular transport is absorption and secretion of larger molecules, which cannot take place via the paracellular route [32].

There are several mechanisms by which cells can translocate substances via transcellular transport. The process of uptake is called endocytosis. There are several distinct types of endocytosis: phagocytosis, clathrin-mediated endocytosis, caveolin-mediated endocytosis, clathrin/caveolae-independent endocytosis, and macropinocytosis [32, 42]. Many membrane bound- and cytoskeletal proteins are involved in endocytosis [43]. Figure 2.2 depicts a schematic view of macropinocytosis showing the role of actin reorganisation in the uptake of substances. Enterocytes and M-cells are mainly responsible for transcellular transport [33].

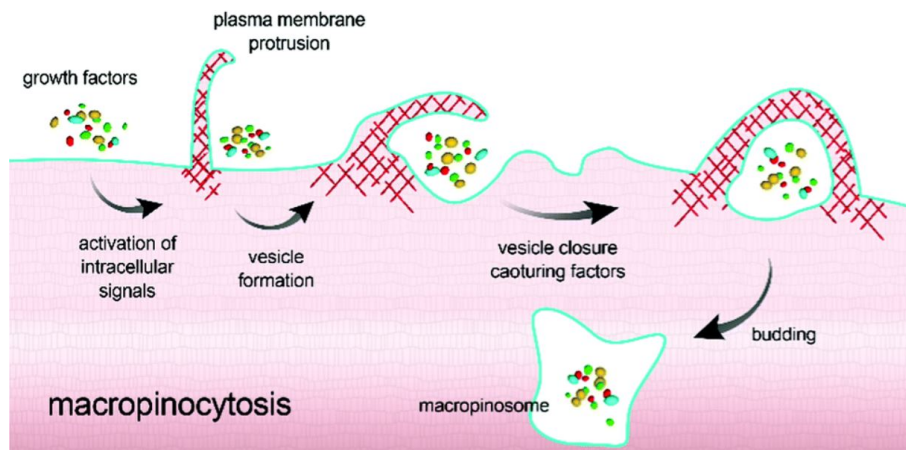


Figure 2.2: Schematic representation of macropinocytosis. The F-actin cortex reorganizes to take up substances [42].

Finally, **unrestricted transport** can occur in pathological situations. The function of the intestinal barrier is dependent on the cooperation of the components that make up the barrier. Under pathological conditions, the barrier can be compromised, for instance by infectious, ischemic or immune-derived stimuli. The paracellular pathway can become leaky because of a loss in transmembrane proteins. The transport can even become unrestricted by the total loss of the TJ-complexes. In unrestricted transport, large and small molecules can cross the barrier. Furthermore, bacteria and viruses can move towards the blood system, which can potentially be dangerous. Long-term damage is mostly avoided because of the rapid reformation of the epithelial barrier. When unrestricted transport occurs, surviving epithelial cells spread to cover the basement membrane before new cells can be generated by proliferation [37].

To summarize, the intestinal barrier contains the mucosa layer. The mucosa layer is an epithelial cell barrier with a few important functions. The first is to absorb nutrients. Secondly, the cells form a barrier against harmful substances, such as pathogens and foreign particles. There are different routes substances take to cross the epithelial barrier. The type of transport depends on particle properties, with size being one of the crucial properties. Only small substances with a diameter up to 10-20 nm can cross the barrier via the paracellular pathway. Larger molecules are transported via the transcellular pathway or in pathological conditions by the unrestricted pathway.

### 2.1.2 *In vitro* models of the intestinal epithelial cell barrier

To study the transport of molecules across the intestinal barrier, several *in vitro* models found in literature, such as organs-on-chip or organotypic models. These systems replicate functional units of organs to model organ (patho)physiology *in vitro*. A commonly used intestinal barrier model is *in vitro* (co)culture models with cell lines derived from tumors. Here, cell cultures are grown on permeable membranes to allow access to both apical and basolateral compartments, as schematically depicted in Figure 2.3. When the cells are cultured under specific conditions for a particular period, they will form a monolayer. The monolayer that is formed shows characteristics similar to the intestinal barrier [44].

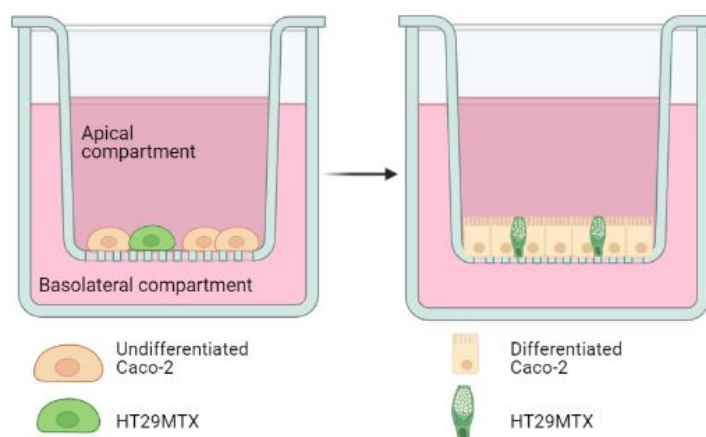


Figure 2.3: Schematic representation of Caco-2 differentiation and HT29 growth on a transwell membrane after approximately 21 days. Image was created using Biorender.

The most widely used cell line for human intestinal *in vitro* models is the Caco-2 line [45]. The model has become a standard tool to obtain an indication of intestinal permeability, absorption, metabolism and bioavailability of drugs for several substances. It has been extensively used as an *in vitro* barrier model [46, 47, 48]. After reaching confluence on a filter support, Caco-2 cells start to differentiate from colon cells into polarized cells. After differentiation, the cells show many properties of enterocytes, such as apical microvilli and intercellular TJ which serves as a physical and biochemical barrier for ions and small molecules [49].

A second cell type that is often added to the Caco-2 cell model is HT29MTX. The human adenocarcinoma colorectal cell line HT29 can be differentiated, in the presence of methotrexate (MTX), into mucus-producing goblet cells called HT29MTX [50]. Similar protein expression was found in HT29 cells and scrapings of the human epithelium *in vivo* [51]. Adding HT29MTX cells to the mono-culture of Caco-2 cells give rise to a mucus layer that functions as a physical and biochemical barrier for substances. The presence of mucus in the model is important for estimation of the intestinal permeability as the mucus acts as a physical and biochemical barrier [52]. The mucus layer is also present in *in vivo* situations [31], so a co-culture of Caco-2 and HT29MTX provides a more realistic model than a mono-culture of Caco-2 cells [53].

Even though the Caco-2 cell model and co-culture model of Caco-2 and HT29MTX cells are widely used, there are some drawbacks that must be taken into account. Tumoral cells, such as Caco-2 cells, are found to over- and underexpress certain proteins [51], leading to an altered phenotype that may impact the permeability [54]. For example, the overexpression of TJ proteins can lead to an incorrect estimation of *in vivo* permeability of compounds that can take the paracellular route [44]. HT29MTX cells express less tight junctions, and by the secretion of mucus, the co-culture is thought to be a better representation of the *in vivo* situation [52]. Still, other cell types, such as M-cells are missing, which could possibly exclude some routes for transportation. Permeability characteristics, have found to be alike for different substances, such as passive transport of different types of drugs [55]. Still, the difference between *in vitro* models and the *in vivo* situation can be different for other substances.

To summarize, Caco-2 and HT29MTX cells are widely used for *in vitro* models of intestinal epithelial cell layers. Overexpression in Caco-2 cells may lead to a decreased permeability compared to *in vivo*. Next to this, by the exclusion of M-cells, some transcellular routes may be excluded, which may also decrease the permeability of the *in vitro* cell model. By the addition of HT29MTX, the TJ-expression and presence of mucus are more similar to *in vivo*. It is assumed that the co-culture of Caco-2 and HT29MTX a better representation of the *in vivo* situation than the Caco-2 model. However, to know the exact permeability characteristics of amyloid fibrils, it is recommended to measure the permeability *in vivo*.

### 2.1.3 Evaluation of the *in vitro* cell models

To evaluate *in vitro* cell model of the intestinal epithelial cell barrier, different experiments can be performed. First, to determine the cell layer integrity, Transepithelial Electrical Resistance (TEER) can be measured. TEER is the measurement of electrical resistance across a cell layer, which reflects the ionic conductance of the paracellular pathway in the cellular monolayer [45]. TEER values are an indicator of an intact cellular layer which suggest low permeability for ions and molecules [56]. TEER is a non-invasive method and can be used to monitor the growth and expansion of the cell layer by division of cells [45]. In the same way, TEER values can suggest a compromised barrier which indicates increased permeability. For permeability studies, an intact cell layer is necessary to avoid unrestricted transport.

TEER values are an indication of cell layer integrity by transport of ions, but the TEER values do not represent the permeability for the compound of interest. The transport rate of a compound in *in vitro* models is typically expressed as the apparent permeability coefficient ( $P_{app}$ ).  $P_{app}$  (in cm/s) is calculated using equation 2.1 [44, 46].

$$P_{app} = \frac{dC \times V_a}{dt \times A \times C_i} \quad (2.1)$$

$dC/dt$  represents the change in the concentration of the particle of interest in the basolateral compartment ( $\mu\text{M/s}$ ).  $dC/dt$  can be determined from the slope of the cumulative concentration.  $V_a$  the volume in the apical compartment (mL),  $A$  the surface area of the entire membrane ( $\text{cm}^2$ ) and  $C_i$  the initial concentration of particles in the apical compartment ( $\mu\text{M}$ ) [46].  $P_{app}$  includes the transport of all transport mechanisms.

TEER values and apparent permeability can be determined for a monoculture (Caco-2) and co-culture (Caco-2 and HT29MTX). Cells that express more TJ-proteins show higher TEER values than cells that express fewer TJ-proteins [56]. Caco-2 cells express more TJ-proteins than HT29MTX cells, and it is indeed reported that the mono-culture shows higher TEER values than the co-culture [44, 53]. TEER values for Caco-2 layers are reported to be  $150\text{-}400 \Omega \times \text{cm}^2$  after 21 days of culturing [45]. For co-cultures with Caco-2 and HT29MTX, the TEER values depend on the seeding ratio, but are always lower than solely Caco-2 cells. The values vary from lab to lab because of the heterogeneity of the cell lines. The TEER values should be monitored during culturing. When the TEER values reach a plateau, the cell layer can be used for testing [45, 57]. This does not imply that the apparent permeability is lower for all molecules in Caco-2 models compared to the co-culture. Some studies report that the apparent permeability in Caco-2 is lower than in the co-culture, for example for the fluorescence molecule Lucifer Yellow [44, 53] or PS nanoparticles [26]. Others propose that the mucus layer secreted by the HT29MTX cells is an extra barrier for the substances, so the apparent permeability is lower for the co-culture than the mono-culture [58].

To summarize, *in vitro* cell models with Caco-2 and HT29MTX cells is a commonly used cell model for simulation of the intestinal epithelial cell barrier. Caco-2 cells differentiate into enterocytes and express TJ-proteins. HT29MTX cells are goblet cells that can secrete mucus. A cell model containing only Caco-2 cells show higher TEER values than a co-culture model with HT29MTX cells. TEER values are not directly related to the permeability, so the apparent permeability of the substance of interest should be measured to study the transport mechanism.

## 2.2 Amyloid fibrils

Amyloid fibrils are formed from (partly) denatured or misfolded proteins. Fibril formation is usually irreversible in physiological conditions, as the amyloid-forming form of proteins is often thermodynamically more stable than the native state. The formation of amyloid fibrils when there are no amyloid fibrils present in the first place is called primary nucleation. The term secondary nucleation is used to refer to nucleation that is induced by the presence of amyloid fibrils. The growth of nucleation can be represented in a sigmoidal growth curve with three phases: **nucleation**, **elongation** phase and **plateau** phase [1, 59]. Figure 2.4 shows the different phases and the corresponding protein structures.

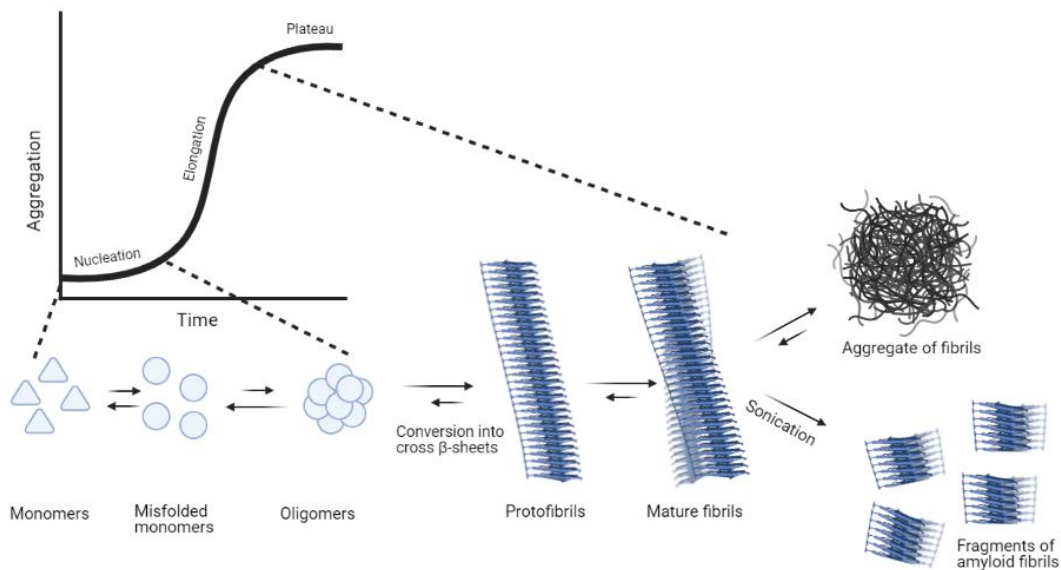


Figure 2.4: Schematic representation of amyloid fibril formation. The growth is represented in a sigmoidal curve with three phases: nucleation, elongation and plateau phase. Misfolded proteins aggregate to oligomers and after conversion into cross- $\beta$ -sheets, amyloid fibrils are formed. Amyloid fibrils can form larger aggregates and amyloid fibrils can be sonicated to fragment them into smaller amyloid fibrils. Image was created using Biorender.

In the **nucleation phase**, (partly) misfolded proteins aggregate into protofibrils, which act as nuclei that can elongate to form fibrils. These nuclei are believed to be held together by hydrogen interactions and salt bridges. Different conditions influence the lag-time, such as the monomer concentration, type of monomers, pH and temperature [59].

In the **elongation phase**, fibrils are formed by monomers binding to the ends of the nuclei. The monomers adopt cross- $\beta$ -sheet conformations parallel to the fibrillar axis. The rate of elongation depends on the monomer concentration and the amount of available fibril ends. Between the nucleation phase and the elongation phase, there is an intermediate state: oligomers. As the name implies, an oligomer is an aggregate of multiple monomers. Oligomers are believed to be more cytotoxic to cells compared to fibrils [60, 61], but the oligomeric state is thermodynamically meta-stable. There must be a minimum concentration of monomers in the elongation phase to have elongation [59].

In the **plateau phase**, the growing rate levels off because of the depletion of monomers. The rate of addition of monomers to fibril ends is in equilibrium with the rate of monomers detaching from the fibrils [59].

There are several proteins that are capable of forming amyloid fibrils. In this project, two types of food amyloid fibrils are used: hen egg-white lysozyme and  $\alpha$ -Synuclein. Properties of lysozyme and  $\alpha$ -Synuclein will be discussed in the next section.

### 2.2.1 Lysozyme

Human lysozyme is found in tears, saliva and human milk. It acts as a non-specific defense against gram-positive bacteria by hydrolysis of the peptidoglycan cell wall [62]. hen egg-white lysozyme is an ortholog of human lysozyme with around 60% sequence similarity with human lysozyme [8, 63]. It contains 129 residues and has a molecular weight of 14.3 kDa. The structure of hen egg-white lysozyme contains  $\alpha$ -helical and cross- $\beta$ -sheet regions, which is depicted in Figure 2.5a. Residues 57-107 of hen egg-white lysozyme are believed to be responsible for amyloid formation [60, 64]. At neutral pH, lysozyme is net positively charged [11, 65]. In physiological conditions, lysozyme is a stable enzyme that does not easily aggregate to form amyloid fibrils. Fibrillation of human and hen egg-white lysozyme occurs at a pH of 2 and temperature of approximately 70°C [63]. At these conditions, lysozyme is unfolded and can form amyloid fibril aggregates with key amyloid fibril characteristics, such as cross- $\beta$ -sheet-rich structure, fibrillar morphology and self-seeding abilities [8].

Some mutations of lysozyme are known to form amyloid fibrils in physiological conditions. The exact mechanisms of how these amyloid fibrils can affect various organs are not fully understood. It is believed that oligomeric and mature fibrils of lysozyme have cytotoxic effect *in vitro*. Probably there is an effect on organs as well, which can reduce organ function and eventually organ failure [61]. It is known that lysozyme fibrils can act as fibrils onto which monomers of disease-related amyloid-forming proteins can bind [11]. This property of lysozyme can also be exploited for the determination of the concentration of lysozyme fibrils and will be further discussed in Section 2.3.3 about Real-Time Quaking-induced Conversion.

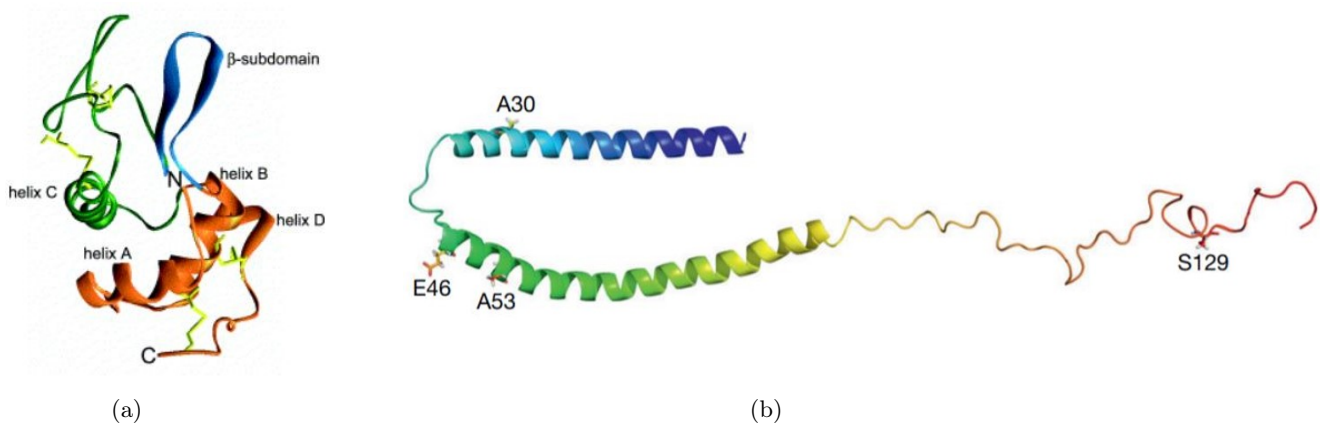


Figure 2.5: (a) Representation of the structure of a lysozyme monomer. The orange parts are segments 1-38 and 108-129. Green is segment 57-107, which is the region responsible for amyloid formation. Segments 39-56 are blue [64]. (b) Representation of the membrane-bound form of an  $\alpha$ -Syn monomer including the mutation sites (A30P, E46K and A53T) that are associated with Parkinson's disease. The red part is the unstructured C-terminal, blue the N-terminal and green the NAC-region [6].

### 2.2.2 $\alpha$ -Synuclein

$\alpha$ -Synuclein ( $\alpha$ -Syn) is a protein mainly expressed in neuronal tissue and is involved in the pathogenesis of several neurodegenerative diseases. Next to this, early onset of Parkinson's disease is induced by different mutations such as A30P, E46K and A53T [66]. The number in the mutation indicates the residue and the letters the type of amino acid. For instance, A53T indicates that the alanine at the amino acid 53 is replaced by threonine.  $\alpha$ -Syn and some mutations are schematically depicted in Figure 2.5b.  $\alpha$ -Syn contains 140 residues and has a molecular weight of 14 kDa. At physiological conditions,  $\alpha$ -Syn is net negatively charged [13]. The normal functions of  $\alpha$ -Syn remain unclear, but several reports show that it probably has a role in the regulation of neurotransmitter release, synaptic function and plasticity [13].

Monomeric  $\alpha$ -Syn is intrinsically disordered, meaning that it lacks a three-dimensional structure in the absence of cells or molecules such as proteins or RNA. The central region, residue 61-95, is called the NAC-region (non-amyloid component). It contains a high density of hydrophobic amino acids, which is critical for the amyloidogenic properties of  $\alpha$ -Syn. The NAC-region is believed to form the core of the cross- $\beta$ -sheet structure. This is known because, cross- $\beta$ -Syn lacks this region and this is not able to form amyloid fibrils [67]. The C-terminal of  $\alpha$ -Syn is acidic and net negatively charged and can shield the NAC-region to prevent spontaneous aggregation.  $\alpha$ -Syn is net negatively charged.

Most vertebrate species that humans consume, express  $\alpha$ -Syn, including cow, chicken and pig, and several fish species.  $\alpha$ -Syn is mostly abundant in brain tissue, but is also found in other tissues, including skeletal muscle and bone marrow. Small traces of  $\alpha$ -Syn are found in bovine milk proteome [10]. This indicates that  $\alpha$ -Syn is present in meat and milk that humans consume. Approximately 90% of the amino acid sequence of those animals corresponds to human  $\alpha$ -Syn, see Appendix Figure A1. For porcine  $\alpha$ -Syn, this is 98%. This means that there are three differences in amino acid sequence between porcine and human  $\alpha$ -Syn, which are A53T, G68E, and V95G [68]. The differences in properties of porcine  $\alpha$ -Syn and human  $\alpha$ -Syn have been investigated by Larsen et al. [68, 69]. A decreased fibrillation propensity of  $\alpha$ -Syn in the presence of the three mutations A53T, G68E, and V95G was found.  $\alpha$ -Syn with only one mutation is more prone to fibrillation [68]. For this research,  $\alpha$ -Syn A53T was used as a model for animal  $\alpha$ -Syn, but  $\alpha$ -Syn A53T might have different physico-chemical properties, for instance in fibrillation.

## 2.3 Principles of experimental methods

### 2.3.1 Fluorescence

The process of fluorescence involves the absorption of light by a molecule followed by the emission of some of this light energy a few nanoseconds later. In this process, some energy is lost, because of vibrational relaxation. This results in emission of a photon with less energy than the absorbed photon. Photons with higher energy have a shorter wavelength than light with lower energy. Therefore, the light emitted from the fluorescence molecule has a longer wavelength than that of the absorbed light. This change is called the Stokes shift [70].

### 2.3.2 Single Particle Tracking

In Single Particle Tracking (SPT), Brownian motion of nanoparticles is followed over time. Brownian motion is the movement of particles in a liquid or gas, caused by collisions between these particles or between the particles and molecules of the liquid or gas. These collisions are stochastic, so the path along which a particle follows is a random walk [71]. The trajectories of particles can be obtained from an acquired image sequence, wherein particles are bright spots on a dark background. The x- and y-coordinates of the particles can be determined on every image by setting a threshold intensity [72]. With algorithms based on the nearest-neighbour theory, the coordinates of the particles are used to calculate the corresponding trajectories. An example of one of those algorithms is the Crocker-Grier algorithm [73]. The algorithm can be used to determine the diameter of the particles and the concentration in the picomolar range [74].

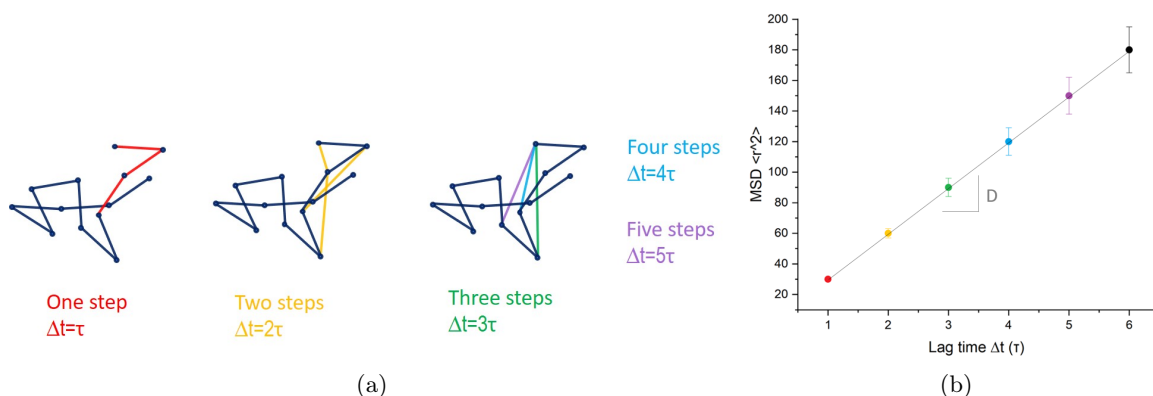


Figure 2.6: (a) An example of a schematic trajectory of a particle moving due to Brownian motion. The blue dots indicate the consecutive frames. Red is the distance the particles has moved in a time of  $1\tau$ . Yellow is  $2\tau$ , green  $3\tau$  and so on. (b) MSD graph of the trajectory. The slope of this graph is the diffusion coefficient (D).

From the trajectories, information about the surroundings and interactions of the particle can be obtained, which can be used to determine motional behavior and characteristics of the solution and the particles, such as particle diameter. This analysis starts with calculating the mean square displacement (MSD) [72]. The MSD, or  $\langle r^2 \rangle$ , describes the average of the squared distance between the position of the particles for all time-lags ( $\tau$ ) of certain lengths within one trajectory. Figure 2.6a shows an example of a random walk of a particle. The blue circles are the consecutive frames. The average for all steps for each lag-time is shown in Figure 2.6b.

With increasing lag-time, there are fewer data points so the uncertainty is increasing. The diffusion coefficient (D) can be described by equation 2.2.

$$\langle r^2 \rangle = q_i D \Delta t^\alpha \quad (2.2)$$

In which  $q_i$  is a numerical constant that depends on dimensionality.  $q_i=2, 4, \text{ or } 6$ , for 1, 2, or 3 dimensional diffusion. D represents the diffusion coefficient,  $\Delta t$  the lag-time and  $\alpha$  gives information about the type of diffusion. A linear MSD-graph with  $\alpha=1$ , indicates normal, or Brownian, diffusion.  $\alpha \neq 1$  describes anomalous diffusion,  $\alpha < 1$  subdiffusion, so diffusion is restricted and  $\alpha > 1$  superdiffusion, which can indicate active transport. For normal diffusion in 2D the equation can be written as:

$$\langle r^2 \rangle = 4D\Delta t \quad (2.3)$$

The diffusion coefficient, D, of spherical particles is the slope of the MSD-graph and can be described by the Einstein-Stokes equation:

$$D = \frac{K_B T}{6\pi\eta R_H} \quad (2.4)$$

In which  $K_B$  is the Boltzmann's constant, T the temperature and  $\eta$  the dynamic viscosity and  $R_H$  the hydrodynamic radius of the particles and. [72].

Inaccuracies of SPT can be due to assumptions made in the determination of the hydrodynamic diameter. First of all, the particles are assumed to be spherical, which is not the case with nanobead aggregates of particles with uneven shapes. Furthermore, to determine an accurate particle diameter with SPT, the viscosity of the solution has to be known, which can change with different temperatures. However, SPT is a relatively simple and fast method, for instance in sample preparation [6].

### 2.3.3 Real-Time Quaking-induced Conversion

Real-Time Quaking-induced Conversion (RT-QuIC) is a quantitative fibril amplification method for detecting protein aggregation [75, 76]. RT-QuIC is widely implemented for the diagnosis of prion diseases and can be applied to different biological samples, such as whole blood, plasma, cerebrospinal fluid and urine [75]. In RT-QuIC, the amount of amyloid fibrils is quantified using the reduction in lag-time of elongation. Elongation occurs in a defined temperature, pH and buffer and occurs in a cyclic manner, as depicted in Figure 2.7a. Template fibrils, called seeds, are fragmented after a quaking step to create more binding spots. Aggregation and shaking cycles are repeated to create exponential growth of the proteins. The experiments are performed over 5-13 days [75]. Aggregation can occur via seed-elongation or surface-mediated RT-QuIC. Seed-elongation is mostly homologous, meaning the seeds consists of the same protein as the monomers. In seed-elongation RT-QuIC, monomers bind to available extremities of the fibrils. The monomers that are added adopt the same morphology as the seeds.

In surface-mediated RT-QuIC, monomers do not bind to the extremities of the seeds, but interact with other binding sites of the fibril. This method is mostly heterologous, so the fibrils can induce aggregation of a different protein [78]. The protein structure of elongated fibril is not necessarily the same as the structure of the seeds. An example of such aggregation is lysozyme with  $\alpha$ -Syn wt monomers, where the net positive charge of lysozyme plays an important role. It is hypothesized that lysozyme fibrils bind to the negatively charged C-terminal of  $\alpha$ -Syn. The aggregation-prone NAC-region is now exposed and available to bind with the C-terminal of other  $\alpha$ -Syn monomers. The structure is left in a more aggregation-prone conformation on the lysozyme fibril surface, so monomers will assemble on the surface [11].

It has been observed by researchers of the NBP-group that lysozyme monomers can also cause aggregation of  $\alpha$ -Syn wt monomers. Therefore, it is important to add a control group with monomers. To reduce the aggregation caused by interactions of  $\alpha$ -Syn with lysozyme monomers, it is possible to increase the salt concentration of the buffer. By doing this, the charge of monomers is screened, so the binding of  $\alpha$ -Syn monomers to lysozyme monomers is reduced. Fibrils have a higher charge density than monomers, so the net charge of fibrils is not screened in a salt solution.

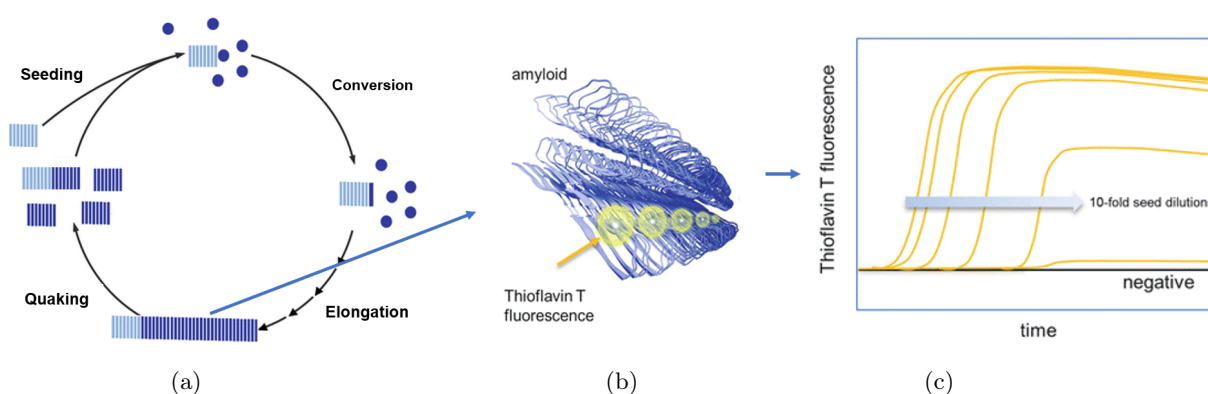


Figure 2.7: Schematic representation of the principle of RT-QuIC. (a) The cyclic process of seed-elongation of monomers to a template fibril, or seed. (b) ThT binding to amyloid fibrils and emits a fluorescence signal. (c) The increase of ThT emission is a sigmoidal curve with lag-time decreasing with increasing concentration of seeds. Images were adapted from [77].

Aggregation in RT-QuIC is quantified by the real-time recording of Thioflavin-T (ThT) dye fluorescence [79]. ThT contains a cationic benzothiazole group which is connected to aniline rings by a single C-C bond. In aqueous conditions, the two aromatic rings can rotate freely around their bond. Upon excitation, this rotation causes ThT to relax from a radiative excited state to a non-radiative state, causing quenched fluorescence. When binding onto the cross- $\beta$ -sheets of amyloid fibrils, the rotational freedom of the C-C bond is lost and the non-radiative decay impedes. Consequently, this relaxation leads to an increased and blue-shifted fluorescence of ThT [80, 81]. In this way, the fluorescence signal of ThT is proportional to the amount of cross- $\beta$ -sheets. ThT emits a fluorescence signal upon binding to fibrils at excitation of 450 nm and emission of 480 nm [79].

During RT-QuIC, the increase of ThT signal describes the amyloid formation in a lag-phase, an exponential phase and a plateau, see Figure 2.7c. The curve depends on the experimental conditions and the fibril concentration. By thresholding, the lag phase can be exploited, which correlates to the amount of fibrils in the samples. The logarithmic concentration of fibrils is inversely linear to the lag-time. Another, more quantitative method is to look at the time necessary to reach 50% of the maximum fluorescence. Different factors can influence the lag-time, such as the type of protein and buffer conditions. Acidic pH and high salt concentration have been shown to either enhance RT-QuIC reactions or result in spontaneous aggregation of the seed [82]. Abnormalities in the curves can be due to heterogeneity of the sample or entrapment of ThT. For these reasons, negative and positive controls are usually added in which respectively very slow aggregation occurs and in which an increase of fluorescence is observed [79].

Lysozyme and  $\alpha$ -Syn A53T fibrils can both reduce the lag-time of aggregation of  $\alpha$ -Syn wt monomers in a concentration dependent matter [11, 12]. This means that it is possible to exploit RT-QuIC to obtain the concentration of fibrils in a solution. For  $\alpha$ -Syn A53T, the mechanism is seed-elongation and for lysozyme surface-mediated. As mentioned, for lysozyme, the binding is driven by the difference in net charge between lysozyme and the C-terminal of  $\alpha$ -Syn [11]. It is expected that, at equal fibril concentration, aggregation in seed-elongation is faster, because, in this case, not all  $\alpha$ -Syn wt monomers that bind to lysozyme will form a new binding site for a second  $\alpha$ -Syn wt monomer. However, surface-mediated RT-QuIC is a good method to exploit when homologous seeding is not possible because of buffer conditions (temperature, pH etc.) [78].

### 2.3.4 Atomic Force Microscopy

Atomic Force Microscopy (AFM) is a technique with which the dimensions of nanometer sized particles can be determined. It is therefore an appropriate technique for studying the morphology of amyloid fibrils at a resolution of a few nanometer. A cantilever with a sharp tip scans over a sample surface and records the topography of the surface by variation in interactions between the tip and sample experience by the cantilever [6]. For imaging of amyloid fibrils, tapping-mode AFM is used. Amyloid fibrils can be imaged in dry samples. In tapping mode, the cantilever moves at or near the resonance frequency. The tip briefly touches the surface at each bottom of each swing. Interactions between the tip and the sample reduce the oscillation amplitude [83]. The lag-time between the oscillation amplitude and the driving amplitude determines the contrast in the AFM images. The amplitude should be large enough to overcome capillary forces, but must not damage the sample [6]. The movement of the tip is usually determined by the detection of a laser beam deflection on a diode.

### 3 Methodology

In this chapter, the methodology and experimental procedures will be explained in detail. First, methods and materials for the *in vitro* cell models will be explained. This will include cell culture, viability, staining and (confocal) microscopy. Next, quantification and permeability studies will be explained for nanobeads and for amyloid fibrils. For amyloid fibrils, the methods of aggregation, labelling, RT-QuIC, AFM and FCS will be presented.

#### 3.1 *In vitro* cell model of the intestinal epithelial barrier

##### 3.1.1 Cell culturing and seeding

Two different *in vitro* models were used to study the ability of amyloid fibrils to permeate the intestinal barrier. The first model was a mono-culture of Caco-2 cells and the second model was a co-culture of Caco-2 and HT29MTX cells. HT29MTX cells were added to test the influence of the presence of goblet cells and the influence of mucus on the permeation of amyloid fibrils.

Caco-2 and HT29MTX cells were cultured in Dulbecco's Modified Eagle Medium (DMEM) with 20% fetal bovine serum (FBS) to provide essential nutrients and growth factors. 10% FBS was used in the co-cultures. 1% Penicillin-Streptomycin (P/S) was added to prevent bacterial contamination. Finally, 1% non-essential amino acids (NEAA) was added to the culture medium as a supplement to increase the cell growth and viability. This culture medium was added to the cells during culturing in T25 flasks, and also during the differentiation process on the transwell membranes in the apical and basal chamber. During permeability studies, the same culture medium, but without Phenol red was used. Refreshing of culture medium was done every 2-3 days. The cells were maintained in an incubator at 37°C and 95% atmospheric O<sub>2</sub> and 5% CO<sub>2</sub>.

Before seeding, the cells were trypsinized with 0.25% Trypsin in EDTA for approximately 8 minutes at 37°C. The cell suspension was centrifuged at 1200 rpm for 3 minutes to obtain a cell pellet. Culture medium was added for resuspension of the pellet. The cells were counted in a Neubauer chamber and seeded on the transwell-membranes (pore size: 3.0  $\mu\text{m}$ ) at a cell concentration of  $1 \times 10^5$  cells/cm<sup>2</sup> (33,600 /transwell) for the mono-culture with only Caco-2 cells. In the co-culture, Caco-2 was seeded at a concentration of  $4.5 \times 10^4$  cells/cm<sup>2</sup> (15,000 /transwell) and HT29  $1.5 \times 10^4$  cells/cm<sup>2</sup> (5,000 /transwell). A ratio of 1:3 of HT29MTX cells to Caco-2 cells is reported to be the best compromise between the model response and the presence of mucus in the layer [52]. The cells were cultured on the transwell membranes until they were used for the permeability tests. The permeability tests were performed between day 21 and 25 after seeding the cells.

##### 3.1.2 Monolayer integrity: Transepithelial Electrical Resistance

Transepithelial Electrical Resistance (TEER) measurements were performed every 2-3 days during the differentiation process to monitor the cell layer integrity. For the TEER measurements, the commercially available system Epithelial Voltohmmeter (EVOM3) with STX2-PLUS electrodes were used. EVOM3 can generate a low AC current that avoids electrode metal deposits and negative effects on tissues which

can possibly be caused by higher DC currents. One electrode was placed in the apical compartment and the second electrode in the basolateral compartment. The electrodes contain silver/silver chloride pellet for measuring voltage and a silver electrode for passing current [56]. The measurements were performed in a 24-wells plate with 700  $\mu\text{L}$  cell culture medium in the basolateral compartment and 250  $\mu\text{L}$  in the apical compartment. The measured resistance of the cellular monolayer was corrected for the surface area and the resistance of an empty membrane.

### 3.1.3 Cell viability

A MTT assay was performed to measure cell viability. For the MTT assay, the seeding concentration was 5,000 cells/cm<sup>2</sup>. The MTT assay was performed in single day seeded cells. In a MTT assay, the metabolic activity of cells was measured. It is therefore an indicator for the cell viability, proliferation and cytotoxicity. A yellow tetrazolium salt (3-(4,5-dimethylthiazol-2-yl)-2,5-diphenyltetrazolium bromide, or MTT) was reduced into purple formazan crystals by viable cells containing NAD(P)H-dependent oxidoreductase enzymes [84, 85]. Formazan accumulates as an insoluble precipitate inside the cell as well as being deposited near the cell surface and in the cell medium [85]. Formazan was dissolved with a solubilization solution. The degree of light absorbed was measured by a spectrophotometer (Tecan) at 570 nm. Measurements at a reference wavelength (650 nm) were subtracted from the measurements to correct for the difference between locations of measurements [84]. The measurements were normalized between 0% and 100%, with 0% being a blank sample and 100% a control without nanobead exposure.

### 3.1.4 Fixation and Staining of the cells

Before imaging the cell layer, the Caco-2 and HT29MTX cells need to be fixed and stained. The fixation and staining protocols were equal for both cell types. Cells were fixed with 4% paraformaldehyde (PFA) in Phosphate-buffered saline (PBS) for 20 minutes after the experiments. After fixation, the cells were washed 3x with PBS. Before staining the cells, the cell membrane was permeabilized with 0.1 % Triton-X for 10 minutes and again washed 3x with PBS. Alexa Fluor 488 (AF488) phalloidin was used to stain F-actin. AF488-phalloidin was used at a concentration of 5 units/mL (165 nM) for 20 minutes. To visualize the cell nucleus, DAPI dilactate (4',6-diamidino-2-phenylindole) staining was used with a treatment of 5 minutes of 2  $\mu\text{g}/\text{mL}$ . After fixation, permeabilization and staining, the membrane of the transwell was cut out of the holder. The membrane was put on a microscope slide with the cells facing upwards. A droplet of mounting medium was added before covering the membrane with a coverslip (thickness No. 1.5H). During imaging, the cell-side of the membrane was faced towards the objective.

Qualitative analysis of mucus, secreted by HT29MTX cells, was performed with Alcian staining. For this, the cells were fixed with 4% PFA or with Methacarn. Methacarn (60% methanol, 30% chloroform, 10% acetic acid) was added to the apical and basolateral compartment. Incubation was done at 4°C for 15 minutes. The cells were gently washed with water and the membrane was cut out of the holder. The Alcian blue solution was filtered through a 0.02  $\mu\text{m}$  syringe filter and was added drop wise to the cell layer until the entire surface was covered. The Alcian staining was removed from the membrane after 15 minutes. Multiple washing steps were done to remove the excess of staining. A counter staining of 0.1% Eosin was used to stain the cytoplasm. After this, the membrane was washed until the water stayed colourless.

### 3.1.5 Confocal imaging

To image the nanobeads and amyloid fibrils within the cell layers, confocal laser scanning microscopy was used. With confocal microscopy, the optical resolution is improved compared to wide-field microscopy by blocking of out-of-focus-light by a pinhole. To create an image, the focused spot is scanned across the sample. With confocal microscopy, it is possible to obtain information for z-slices and generate 3D-images [86].

A Picoquant MicroTime200 Laser scanning confocal microscope was used for imaging the cell layer. The lasers were operated in a pulsed interleaved excitation (PIE) mode with repetitive three-color pulses. The excitation wavelength for the nanobeads and amyloid fibrils was 636 nm, for F-actin (AF488-phalloidin) 483 nm and for the cell nucleus (DAPI) 401 nm. The 483-nm laser pulse was followed by pulses at 483 nm and finally 636 nm. The time between two subsequent pulses was 25 ns. An optical filter of 690/70 was placed before the detector of the 636-laser, of 520/35 for detector the 483-laser and 438/24 and 447/60 before the 401-laser. The dichroic mirror transmitted 80% of the light and reflects 20% of the light. The diameter of the pinhole was 50  $\mu\text{m}$ . The distance between z-slices was 1  $\mu\text{m}$  and the number of pixels was chosen to obtain a pixel size of approximately 100 nm. The objective was Olympus UPlanSApo 60x WI, so before use a water droplet was placed on the objective. Orthogonal views of the confocal images were made in Fiji by a slice spacing of 1  $\mu\text{m}$  and interpolating the signal.

## 3.2 Polystyrene nanobeads

The nanobeads used within this research were 20 nm polystyrene FluoSpheres<sup>TM</sup> Carboxylate-Modified Microspheres [87] and 200 nm polystyrene Nanospheres<sup>TM</sup> [88]. The 20 nm beads are so-called 'dark red' (ex. 660 nm, em. 680 nm). The 200 nm beads were stained with Nile Red (NR) (ex. 552 nm, em 580 nm). 2 mg of NR powder was added to 1 mL methanol. 10  $\mu\text{L}$  of nanobeads was added to 10  $\mu\text{L}$  NR-methanol-solution and 990  $\mu\text{L}$  MiliQ water. Before diluting the nanobeads from the stock solution, the stock was sonicated in a sonication bath for 20 minutes. To determine the exact concentration of nanobeads, a calibration curve was made for the 20 nm and the 200 nm nanobeads. Three sets of solutions were prepared for the calibration.

### 3.2.1 Single Particle Tracking

Nanobead tracking and counting was performed with a custom made microscope. A 640 nm 2.1 Watt laser diode was coupled with an inverted microscope (NIKON TE-2000U). Excitation light was focused on the objective's back focal plane. The objective was Nikon CFI Plan Apo VC 60x WI, NA 1.20. An excitation filter removed light with a wavelength above 640 nm from the laser. The dichroic mirror separated excitation light from emission light. The emission light was filtered by a band-pass filter from 650 nm to 710 nm and a long-pass filter of 647 nm. The exposure time was for all measurements set to 5 ms and the frame rate to 35 frames per second for counting and 150 frames per second for tracking. The videos were analyzed using Trackpy, a Python implementation of the Crocker-Grier particle tracking algorithm. For measuring the concentration of nanobeads, nanobeads were required to be present for at least three consecutive frames, and for the determination of the size, five consecutive frames.

### 3.2.2 Permeability

As a first permeability experiment, the permeability of PS nanobeads through Whatman Nuclepore Track-Etched polycarbonate (PC) membranes, was measured. PC-membranes with two different pore sizes were tested: 400 nm and 1000 nm. Different pore sizes were tested to measure the effect of pore size on the removal of nanobeads in the feed. For this experiment, 200 nm beads were used. The PC-membrane was placed in a holder between two supports. Two syringes were placed on both sides of the filter holder, with one syringe containing nanobeads at a concentration of  $4.5 \times 10^9$ . This syringe was connected to a syringe pump and the flow was set to 20  $\mu\text{L}/\text{min}$ . After wetting the membrane with MiliQ, the measurement started. Every minute, 20  $\mu\text{L}$  of sample was collected from the initially empty syringe. The concentration of nanobeads in the permeate was measured in the SPT set-up. The retention was calculated using equation 3.1.

$$R = 1 - \frac{C_{permeate}}{C_{feed}} \quad (3.1)$$

$C_{permeate}$  is the concentration of nanobeads in the permeate after a plateau is reached and  $C_{feed}$  is the initial concentration of nanobeads.

Next, the permeability of a transwell membrane without cells was measured to test different experimental methods in the SPT set-up. For the permeability tests of the transwell membrane, a custom made holder and Ibidi black 24-wells plate were used to hold the transwell inserts. The custom made holder contained a glass coverslip No.1.5 which needed to be cleaned with UV light for approximately 20 minutes. 100  $\mu\text{L}$  of sample was pipetted into the apical compartment and 600  $\mu\text{L}$  in the basolateral compartment. Testing the set-up on the empty membrane measurements was done with transwell membranes with pores of 0.4  $\mu\text{m}$ . The ‘real-time’ measurements for measuring the concentration of nanobeads in the basolateral compartment were performed on the SPT set-up. After pipetting the nanobeads in the apical compartment, the images were made at a frame-rate of 0.2 fps. Every 5 seconds, an image was taken for a time of 2 hours (1440 frames). During that time, the holder (or 24-wells plate) and transwell inserts were not moved from the set-up. As a positive control, the cells were treated with EGTA (ethylene glycol-bis( $\beta$ -aminoethyl ether)-N,N,N',N'-tetraacetic acid) for 1, 2 or 4 hours.

To measure the permeability for longer time-points, the 24-wells plate was placed on a shake-plate in the incubator in between the measurements. The shake-plate agitated at a speed of 150 rpm. Before measuring the concentration of nanobeads in the basolateral, the transwell inserts were removed from the 24-wells plate and placed in another plate that remained in the incubator to avoid contamination. The transport in percentages was determined with the concentration of nanobeads in the apical and the basolateral compartment by equation 3.2. The factor 6 is from the dilution from the apical compartment to the basolateral compartment.

$$\text{Transport}(\%) = \frac{C_{basolateral}}{6 \times C_{apical}} \times 100\% \quad (3.2)$$

### 3.3 Amyloid fibrils

#### 3.3.1 Aggregation and labelling

The food-related amyloid fibrils studied in this research were hen egg-white lysozyme and  $\alpha$ -Synuclein ( $\alpha$ -Syn). In this research,  $\alpha$ -Syn A53T was used to mimic animal  $\alpha$ -Syn. Unstained lysozyme and  $\alpha$ -Syn A53T fibrils were produced in a *de novo* aggregation reaction by other researchers of the NBP-group. Lysozyme monomers were obtained from Sigma (cat. no. L6876). Amyloid fibrils were produced from fibrils by ultrasound-sonication in a bath-sonicator. The time of sonication for lysozyme was 4 minutes and for  $\alpha$ -Syn A53T the sonication time was experimentally tested to obtain equally long  $\alpha$ -Syn A53T and lysozyme fibrils.

The amyloid fibrils were labelled using fluorescence labels for quantification purposes. Lysozyme monomers were labelled with Alexa Fluor 647 (AF647) NHS ester. AF647 contains a N-Hydroxy succinimide-ester (NHS-ester), which can react to the primary amine (R-NH<sub>2</sub>) of a lysozyme monomer in slightly alkaline conditions. This will result in a stable amide bond [89, 90].  $\alpha$ -Syn  $\alpha$ -Syn A53T monomers were labelled with AF647 C5 maleimide. The alanine at residue 140 was substituted for cysteine (A140C). Maleimide reacts with the sulfhydryl, or thiol, bond of the cysteine in a neutral pH [91]. Before addition of the dye, the storage buffer of  $\alpha$ -Syn A53T was removed. This storage buffer contains dithiothreitol (DTT) to prevent the formation of disulfide bridges and inactivation of the cysteines. The storage buffer was removed by buffer exchange with Zeba Spin desalting column with a molecular weight cut-off of 7 kDa. The buffer was replaced with a labelling buffer, containing tris[2-carboxyethyl]phosphine (TCEP). TCEP is also a disulfide-reducing agent but does not have to be removed before the reaction with maleimide.

The Alexa Fluor dyes were added to monomers with the concentration of dye being twice the concentration of monomers. After incubation of 1 hour at room temperature, the excess of dye was removed by use of a Zeba Spin column with molecular weight cut off of 7 kD. The final protein concentration was calculated with equation 3.3 by measuring the absorbance at the wavelengths 280 nm and 650 nm.

$$C_{protein} = \frac{A_{280} - CF \times A_{650}}{\epsilon_{protein}} \quad (3.3)$$

Where A is the absorbance at 280 nm and 650 nm, CF a correction factor for the contribution of the protein absorbance of the absorbance of the dye, which is 0.05.  $\epsilon_{protein}$  was the molar extinction coefficient (in M<sup>-1</sup> cm<sup>-1</sup>).  $\epsilon$  for lysozyme was 36,000 M<sup>-1</sup> cm<sup>-1</sup> and for  $\alpha$ -Syn 5,600 M<sup>-1</sup> cm<sup>-1</sup>.

After labelling, the monomers were added to amyloid fibrils to induce fibrillation. Labelled fibrils were prepared from incubation of labelled monomers, unlabelled monomers and unlabelled fibrils at a ratio of 1:48:1. The concentrations of fibrils and monomers that should be added to obtain this ratio was determined by the help of the degree of labelling (DOL), as the solution of labelled monomers also contained unlabelled monomers. The degree of labelling was calculated with equation 3.4.

$$\text{DOL} = \frac{A_{650}}{\varepsilon_{\text{dye}} \times C_{\text{protein}} \times l} \quad (3.4)$$

Where  $\varepsilon_{\text{dye}}$  was the molar extinction coefficient for Alexa Fluor dye, which was  $239,000 \text{ M}^{-1} \text{ cm}^{-1}$ , and  $l$  the light path length.

For lysozyme fibrils, incubation was done at  $80^\circ\text{C}$ , with shaking at 750 RPM for 24 hours. The aggregation buffer was  $\text{NaH}_2\text{PO}_4$  50 mM with pH 2.  $\alpha$ -Syn A53T incubation was performed at  $37^\circ\text{C}$  with shaking of 750 RPM for 24 hours. The buffer was Tris 10 mM, NaCl 10 mM, EDTA 0.1 mM with pH 7.4. The labelled fibrils were separated from monomers and oligomers by centrifugation for 1 hour at 21,000 g at  $20^\circ\text{C}$ . The supernatant was removed and the absorbance at 280 nm and 650 nm was measured to determine the concentration again with equation 3.3. The final concentration of labelled fibrils was determined by subtracting the total concentration with the concentration of the supernatant. The concentration of fibrils described throughout this research is equivalent monomer concentration.

### 3.3.2 Bulk fluorescence spectroscopy

Bulk fluorescence measurements were performed on the basolateral samples of the models after treatment of lysozyme and  $\alpha$ -Syn A53T fibrils. With the increase of concentration of fibrils in the basolateral compartment, the apparent permeability can be determined.

Labelled lysozyme and  $\alpha$ -Syn A53T fibrils were pipetted on mono and co-culture models. The initial concentration of fibrils in the apical compartment was  $2.5 \mu\text{M}$ . The 24-wells plate containing the transwell inserts was placed in the incubator on a shake-plate, which agitated at 150 rpm. During measuring the fibril concentration in the basolateral compartment, the transwell inserts were removed from the 24-wells plate and placed in another plate that remained in the incubator to avoid contamination. The concentration of fibrils in the basolateral compartment was determined at different time points using the Fluoromax 4 (HORIBA).  $60 \mu\text{L}$  of sample was pipetted into a QS 3.00 mm cuvette. The excitation was 640 nm and emission 650-800 nm. The front entrance and exit slit were 5.00 nm bandpass for excitation and emission. A calibration curve was made on each day of measuring the permeability. This was done with lysozyme and  $\alpha$ -Syn A53T fibrils in culture medium without phenol red. A blank measurement containing only culture medium without Phenol red was always subtracted from the measurements. The maximum of the emission spectra was taken for the calibration curve and to determine the concentration of fibrils, which was at 669 nm. The transport in percentages was determined with the fibril concentration in the apical and the basolateral compartment by equation 3.5. The factor 6 is from the dilution from the apical compartment to the basolateral compartment.

$$\text{Transport}(\%) = \frac{C_{\text{basolateral}}}{6 \times C_{\text{apical}}} \times 100\% \quad (3.5)$$

The apparent permeability ( $P_{app}$ ) was calculated using equation 3.6.

$$P_{app} = \frac{dC \times V_a}{dt \times A \times C_i} [44, 46] \quad (3.6)$$

$dC/dt$  represents the change in amyloid fibril concentration in the basolateral compartment ( $\mu\text{M/s}$ ).  $V_a$  was the volume in the apical compartment (mL),  $A$  the surface area of the entire membrane ( $\text{cm}^2$ ) and  $C_i$  the initial fibril concentration in the apical compartment ( $\mu\text{M}$ ).  $P_{app}$  of the cell layer without the transwell was calculated with the following equation:

$$\frac{1}{P_{app(\text{cells})}} = \frac{1}{P_{app(\text{total})}} - \frac{1}{P_{app(\text{transwellmembrane})}} \quad (3.7)$$

### 3.3.3 Real-Time Quaking-induced Conversion

Real-Time Quaking-induced Conversion (RT-QuIC) experiments were performed on the samples of the basolateral compartments of the cell-models for lysozyme and  $\alpha$ -Syn A53T to determine whether there were amyloid fibrils or monomers, and in what concentration. Lysozyme and  $\alpha$ -Syn A53T fibrils in the sample, if present, will act as templates for aggregation of  $\alpha$ -Syn wild type (wt) monomers. For lysozyme, the reaction was based on the charge interactions between the positively charged lysozyme and the negatively charged  $\alpha$ -Syn monomers (surface-mediated mechanism). For  $\alpha$ -Syn A53T, the growing mechanism was seed-elongation, meaning the monomers only bind to the extremities of the  $\alpha$ -Syn A53T fibrils.

Recombinant  $\alpha$ -Syn wt monomers were thawed from  $-80^\circ\text{C}$  and filtered through a  $0.02 \mu\text{m}$  syringe filter. A buffer was made with 10 mM Tris pH 7.4, 10 mM NaCl, 0.1 mM EDTA,  $22.22 \mu\text{M}$   $\alpha$ -Syn wt monomers and  $22.22 \mu\text{M}$  ThT diluted in Miliq. NaCl concentration of 150 mM was also tested for RT-QuIC with lysozyme. Dilution series were made for amyloid fibrils and monomers for both types of proteins:

- Fibrils were obtained by sonication of fibrils in a ultrasound-sonication bath. For lysozyme fibrils, the sonication time was 4 minutes and for  $\alpha$ -Syn A53T 10 minutes.
- Lysozyme monomers were obtained by diluting lysozyme from hen egg-white in a  $\text{NaH}_2\text{PO}_4$  50 mM solution with a pH of 2.
- Recombinant  $\alpha$ -Syn A53T monomers were thawed from  $-80^\circ\text{C}$  and filtered through a  $0.02 \mu\text{m}$  filter.

For lysozyme fibrils and monomers, the concentration range was between 0.001 and  $10 \mu\text{M}$ . For  $\alpha$ -Syn A53T fibrils and monomers, between 0.5 nM and  $5 \mu\text{M}$ , with steps of power 10.  $100 \mu\text{L}$  of each of the dilutions, samples or negative control (unseeded) were added to  $900 \mu\text{L}$  of the buffer.  $200 \mu\text{L}$  of the mixture was added in quadruplicate in a black 96-wells polystyrene microplate, covered with a seal. The RT-QuIC experiments were performed at a pH of 7.4 and at a temperature of  $37^\circ\text{C}$ . The fluorescence intensity was measured at the beginning of each new cycle at an excitation wavelength of 458 nm and an emission wavelength of 485 nm. The gain was set to 40. Each cycle consists of 5 repetitions of 1 minute of orbital shaking at 335 rpm and 1 minute without shaking. After 1000 cycles, the measurements were finished.

RT-QuIC data was analyzed using Origin. For each sample, the threshold was the mean +  $5 \times$  standard deviation of the first hour, or first 6 data points. The lag-time was determined by finding the first intercept of the threshold in the intensity versus time plots. The lag-time was normalized to the lag-time of the unseeded sample, with the lag-time of the unseeded sample being 1. The normalized lag-times were plotted versus concentration in a semi-log plot. A linear fit was plotted, which was used to determine the concentration of fibrils in the samples.

### 3.3.4 Atomic Force Microscopy

Atomic Force Microscopy (AFM) was performed on 20 nm beads and amyloid fibrils to determine the exact size. Next to this, AFM was performed on lysozyme and  $\alpha$ -Syn A53T unsonicated and sonicated fibrils to determine the length and morphology of the fibrils.

AFM samples were prepared by adding 20  $\mu$ L to a freshly cleaved mica disk. For all AFM measurements, a concentration of 10  $\mu$ M of fibrils or fibrils was used. To remove unbound fibrils and the buffer, the mica disk was washed three times with MiliQ water and dried with a soft flow of nitrogen. For the measurements, soft tapping mode in air was used with Bioscope Catalyst (Bruker). The HQ:NSC36/Cr-Au BS probe was used with a force constant of 2 N/m. The images were made with a resolution of 512x512 px at a rate of 0.5 Hz. The images were processed with the Nanoscope Analysis software. The length of the fibrils of the AFM-images was measured using Fiji. The mean length was determined from 50 fibrils or nanobeads of at least 2 different AFM images. The concentration of fibrils was 10  $\mu$ M and the concentration of nanobeads was  $1.25 \times 10^5$  nanobeads/mL.

### 3.3.5 Förster Resonance Energy Transfer

The confocal images that were made with Picoquant MicroTime 200 were analysed on the presence of Förster Resonance Energy Transfer (FRET). The images were made with pulsed interleaved excitation, which could be used in the analysis of FRET. AF488 and AF647 could theoretically be a FRET pair. FRET images were made by looking at the second time gate (483 nm) and the detector with an optical filter of 690/70 nm.

### 3.3.6 Fluorescence Correlation Spectroscopy

Fluorescence Correlation Spectroscopy (FCS) experiments were performed on the permeate of the cell-models for lysozyme and  $\alpha$ -Syn A53T to determine whether there were monomers or free dye in the sample. Picoquant MicroTime 200 laser scanning confocal microscope was used for FCS measurements. The excitation wavelength was 636 nm and an optical filter of 690/70 was placed before the detector. The objective was an Olympus UPlanSApo 60x WI, so before use, a water droplet was placed on the objective. Calibration of the focal volume and  $\kappa$  was performed with a solution of 2.5 nM AF647 in MiliQ water before every measurement. The monomer solution was diluted until  $G(0)$  was between 0.1 and 1. OD filters were used to attenuate the laser intensity to approximately 6,000 A.U. Diffusion-time was between 0.001 and 100 ms. All samples were measured for at least 4 times for 60 seconds. The autocorrelation graphs were all fitted to a second order with a triplet state fit. This type of fit was used as electrons of the fluorophore can be excited to the triplet state and emit photons by a process called

phosphorescence. The duration of phosphorescence, is slower than diffusion time of molecules, but it is still long enough to be measured in FCS. By fitting the autocorrelation graph to a triplet state fit, this effect can be taken into account [92]. The hydrodynamic diameter,  $D_h$ , of the particles was determined with the Einstein-Stokes equation:

$$D_h = \frac{K_B T}{3\pi\eta D} [72] \quad (3.8)$$

In which  $D$  is the diffusion coefficient,  $k_B$  the Boltzmann's constant,  $T$  the temperature and  $\eta$  the dynamic viscosity [72].

## 4 Results and Discussion

In this chapter, the results of the research will be presented and discussed. The results are divided into two main sections: polystyrene (PS) nanobeads and amyloid fibrils. PS nanobeads are used as a first step towards developing a methodology to quantify the permeability of the *in vitro* cell models of the epithelial intestinal barrier. The first part of this section will contain the characterization of nanobeads including characterization of particle size and concentration. Nanobead characterization is followed by different experimental methods of measuring the permeability of nanobeads through different membranes. In the second part, the quantification of amyloid fibrils will be discussed. Finally, the permeability characteristics of the different amyloid fibrils in the cell models mimicking gut barrier will be discussed.

### 4.1 Polystyrene nanobeads

#### 4.1.1 Characterization and quantification

To study the permeability of PS nanobeads through the *in vitro* cell models, dark red carboxylated FluoSpheres with a diameter of 20 nm were used. These were the smallest nanobeads available. The exact diameter of these nanobeads was determined using Atomic Force Microscopy (AFM) and Single Particle Tracking (SPT). 200 nm PS nanospheres stained with Nile Red were used to determine the retention of membranes with different pore sizes. For both sizes of nanobeads, the detection range of SPT was determined by counting the number of nanobeads in the captures, which will be discussed in the second part of this section.

The hydrodynamic diameter of the nanobeads was determined with SPT based on the theory discussed in Section 2.3.2. Figure 4.1a shows a capture of the PS-nanobeads made with the SPT set-up. The red circles are nanobeads which are recognized by the tracking program Trackpy. The mean hydrodynamic diameter found with SPT was  $23.0 \pm 7.5$  nm. The diameter of the nanobeads was also examined by measuring the height of the nanobeads in the AFM images, see Figure 4.1b. In AFM, the mean height was  $16.9 \pm 3.8$  nm.

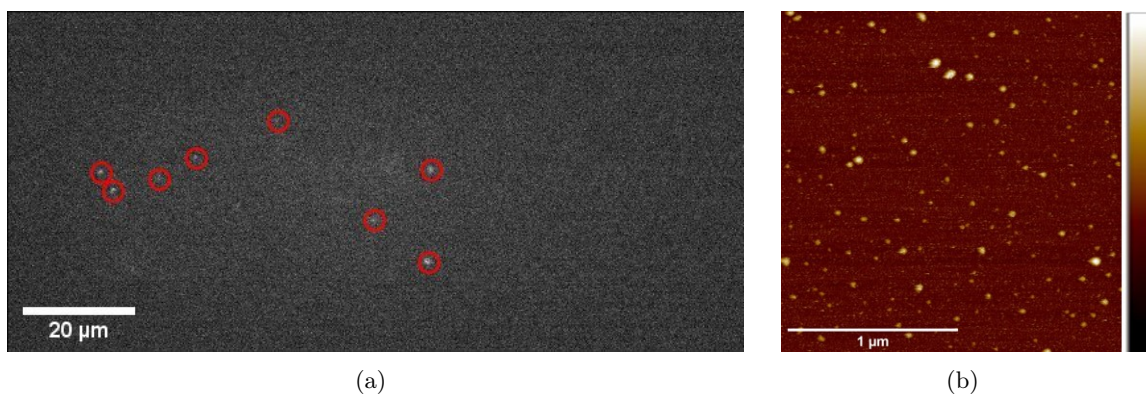


Figure 4.1: (a) Capture of nanobeads in the SPT set-up. Red circles are nanobeads recognized by Trackpy. (b) AFM image of ‘20 nm’ PS-beads. The color scale between black and white corresponds to a height of 25 nm.

The difference between the diameter of the two methods is probably related to the fact that with SPT, the hydrodynamic diameter was measured, while in AFM the particle height was determined. Because of this, AFM offers a more realistic result of the actual nanobead diameter, whereas in SPT the nanobead diameter is inflated. Larger nanobead diameter has been observed in literature for other hydrodynamic determination methods, such as Dynamic Light Scattering (DLS) [93]. The nanobeads appear to be in the expected range of particles that can take the paracellular leaky pathway [32, 39, 40]. This means that the PS nanobeads were suitable for the preliminary model for testing the quantification method.

To determine the concentration range of detection for the 20 nm and 200 nm beads, the number of nanobeads in the detection volume was counted with a tracking algorithm. Figure 4.2 shows the number of nanobeads in the detection volume plotted against the concentration. 20 nm beads were used for the permeability studies on the Caco-2 cell model and 200 nm beads for the permeability experiment with polycarbonate-membrane with different pore sizes.

From the measured number of nanobeads in the detection volume, the concentration could be calculated with the dimensions of the detection volume. The detection volume was 17 pL for the detection of 20 nm beads and 29 pL for the detection of 200 nm beads. The volumes were different, as different lasers were used for the detection. In Figure 4.2c the measured concentration is plotted versus the assumed concentration. The assumed concentration was based on information given by the manufacturer of the nanobeads. The slope should be 1, as the difference between the measured and assumed concentration should not be dependent of the concentration. For the 20 nm beads, the slope was 0.76 with  $R^2$  of 0.99. For the 200 nm beads, the slope was 1.02 with  $R^2$  of 0.98. The decrease of the slope of the 20 nm beads could be due to that for higher concentrations, the tracking program does not track the less bright nanobeads. The off-set between the 20 nm and 200 nm graph could be explained by the number of nanobeads in the stock being not exact as given by the manufacturer. For the lowest concentration, the number of nanobeads in the detection volume was on average less than 1. This means that there were captures measured without containing nanobeads. Within 30 minutes of measuring, the lowest concentration that could be measured was approximately  $10^7$  nanobeads/mL. Lower concentrations could be measured by increasing the measuring time or by using flow to refresh the detection volume. A disadvantage of inducing flow would be the volume, as for this research, the volume in the basolateral compartment would not be enough to perform flow-experiments.

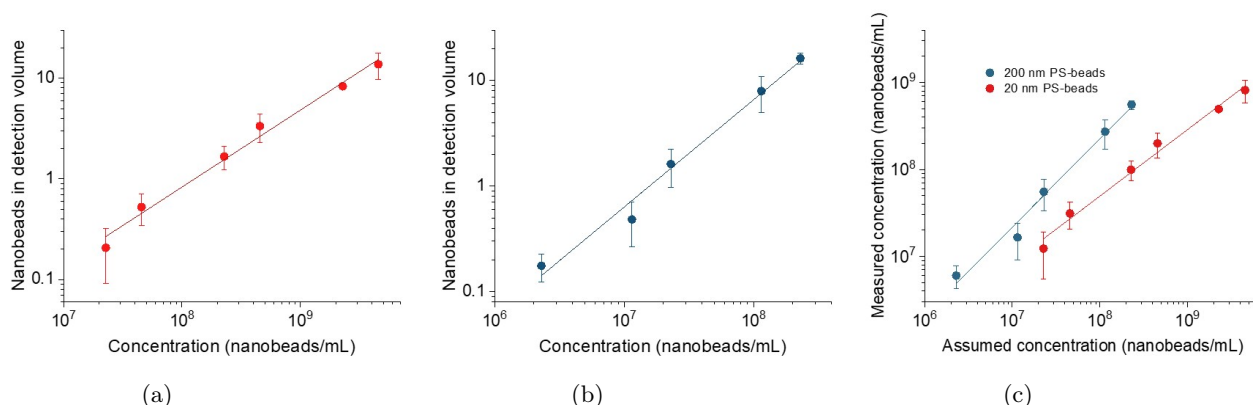


Figure 4.2: Number of (a) 20 nm and (b) 200 nm beads in the detection volume as a function of concentration. The red line shows the linear fit of the data with  $R^2$  0.99 in (a) and 0.98 in (b). The error bars show the standard deviation of 3 independent sets. (c) Measured concentration plotted against assumed concentration.

#### 4.1.2 Viability of Caco-2 cells during exposure to PS nanobeads

To verify if Caco-2 cells were still viable during exposure to PS nanobeads, a MTT viability assay was performed. The understanding of potential toxic effect of nanoparticles on the Caco-2 cell layer is crucial, because if the cells are not viable, the cell layer integrity might get compromised. This might result in change of overall permeability characteristic of Caco-2 cell layer. In this study, carboxylated PS nanobeads were used. The nanobeads have a high density of carboxylic acids (COOH) on their surface. Because of this modification, the PS nanobeads were negatively charged, which is reported to cause a decreased cytotoxic effect compared to positively charged nanobeads [27]. Moreover, charged nanoparticles aggregate less than neutral nanoparticles.

Figure 4.3 shows the viability of Caco-2 cells after exposure to different PS nanobead concentrations and exposure times normalized to the negative control, that did not have a nanobead treatment. Two control groups are shown, as the experiment of 2 hours treatment was not simultaneously performed with 72 hours treatment. There was no difference in the viability observed between treatment time of 2 hours and 72 hours. There was also no difference between the control and the nanobeads concentrations of  $5 \times 10^{10}$ ,  $5 \times 10^{11}$  and  $5 \times 10^{12}$  nanobeads/mL. For the highest concentration of  $5 \times 10^{13}$  nanobeads/mL, the viability of the Caco-2 cells was decreased to approximately 80%.

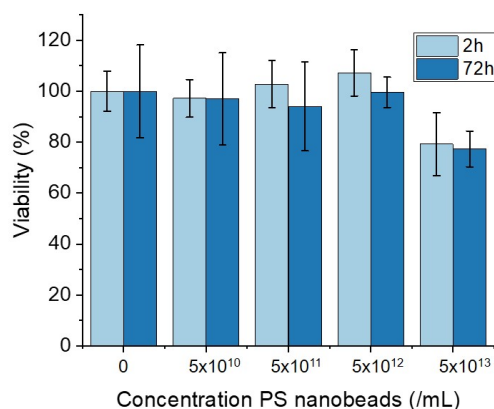


Figure 4.3: Viability of Caco-2 cells after exposure to PS nanobeads at different treatment times and concentration. The error bars show the standard deviation of 4 replicates.

In literature, (carboxylated) PS nanobeads were tested for cytotoxic effects on Caco-2 cells. The nanobead concentrations reported ranged from 0.1 to 200  $\mu\text{g/mL}$ , which corresponds to  $2 \times 10^{10}$  to  $5 \times 10^{13}$  nanobeads/mL. In these studies, carboxylated and non-carboxylated PS nanobeads of 50 nm, 100 nm and 500 nm within this concentration range do not have cytotoxic effect on Caco-2 cells after 24 hours of exposure [28, 29, 30]. The slight decrease in the viability at the highest concentration was not observed by these studies. It is possible that the decrease in the viability observed was not originating from the PS nanobeads, but from other molecules in the particle suspension. The nanobeads were supplied as suspension in water with 2 mM sodium azide ( $\text{NaN}_3$ ) as preservative. The concentration of  $\text{NaN}_3$  in the highest concentration of nanobeads was 0.02 mM. In literature it is reported that a  $\text{NaN}_3$  concentration of 0.015 mM may be toxic to epithelial cells [94]. This indicates that the slight decrease in the viability at  $5 \times 10^{13}$  nanobeads/mL may be due to the presence of  $\text{NaN}_3$ . This effect probably occurred in the first

2 hours after exposure, as there was no difference in the viability between 2 hours and 72 hours. Because of the possibility of cytotoxic effects of  $\text{NaN}_3$  in the nanobead concentration of  $5 \times 10^{13}$  it was chosen to exclude this concentration in the permeability experiments with cells.

From the viability experiment, it became clear that the concentrations of  $5 \times 10^{10}$ ,  $5 \times 10^{11}$  and  $5 \times 10^{12}$  nanobeads/mL did not reduce the cell viability of Caco-2 cells within 72 hours of exposure. Thus, these nanobead concentrations can be used in the permeability experiments with a maximum treatment time of 72 hours.

#### 4.1.3 Permeation of PS nanobeads through membranes with different pore sizes

As a first step in the determination of the permeability of the *in vitro* cell barrier, the retention of polycarbonate (PC) membranes with different pore sizes was determined. This was done to test the experimental set-up and to determine the effect of pore size on the removal of nanobeads. In this experiment, there was a flow exerted by a syringe pump. The flow rate of the syringe pump was  $20 \mu\text{L}/\text{min}$  and every minute the permeate was collected. Figure 4.4 shows the decrease in the nanobead concentration after filtration through the PC-membrane with pores of 400 nm and 1000 nm. The first data point (gray dot) shows the initial nanobead concentration before filtration. For the 400 nm beads, the concentration decreases until it reached a plateau. For the 1000 nm beads, the concentration immediately drops to approximately  $3 \times 10^8$  nanobeads/mL and remained at that concentration. The retention was calculated from the concentration at this plateau by equation 4.1.

$$R = 1 - \frac{C_{\text{permeate}}}{C_{\text{feed}}} \quad (4.1)$$

Retention of 1 indicates complete removal and retention of 0 indicates no removal by the membrane. For the 400 nm membrane, the retention was 0.97 and for the 1000 nm membrane 0.65. For both membranes there was some removal by the membrane, while the pores of both membranes were larger than the nanobeads. This could be due to some pores being smaller than the given pore size, because the pore sizes of track-edged membranes is a distribution. The nanobeads could attach to the membrane and possibly form a cake layer. To conclude, membranes with smaller pores have a higher removal of nanobeads than membranes with larger pores. This makes sense, as larger pores allow more transport compared to membranes with small pores. This is also expected to occur in paracellular transport by cells.

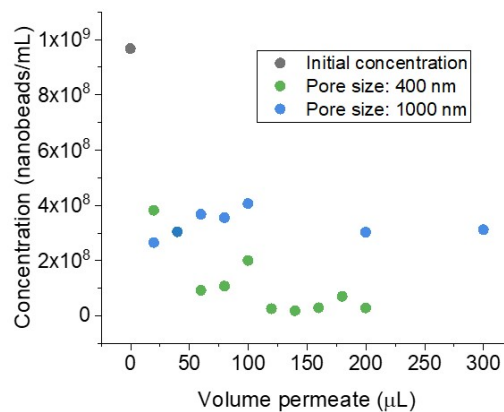


Figure 4.4: Concentration of nanobeads in permeate after filtration of 200 nm PS beads through a PC-membrane with two different pore sizes: 400 and 1000 nm. The gray dot shows the initial concentration in the feed.

#### 4.1.4 Permeation of PS nanobeads through empty transwell membranes

For the permeability experiment by PC-membranes described above, it was not possible to calculate the apparent permeability from equation 2.1 in Chapter 2. This was not possible, because the system was pressure-driven, as the nanobead solution was pushed through the membrane by a syringe-pump. Therefore, it was decided to continue with the permeability experiments where no pressure was applied. First, a transwell membrane without cells was used to test the experimental set-up of the quantification of nanobeads permeability.

It was found that for some permeability studies in literature, a small volume is removed from the basolateral compartment to measure the concentration of nanobeads in the sample. The basolateral sample is replaced with medium [27, 95]. The main issue for the quantification of the permeability in these systems is that the concentration gradient across the membrane was influenced. To overcome this problem, the concentration of the nanobeads in the basolateral compartment was measured in ‘real-time’. Another advantage of measuring the concentration in real-time is that it would provide many data points to extract the change in concentration ( $dC/dt$ ) for the calculations of the apparent permeability.

First, the real-time method was tested on an empty transwell membrane with pores of  $0.4 \mu\text{m}$ . A 24-wells plate containing a transwell was kept on the SPT set-up during the entire experiment. The position of detection in the basolateral compartment was kept constant during the measurements. After adding 20 nm beads in the apical compartment of the transwell membrane, every 5 seconds a capture was made from the detection volume in the basolateral compartment with the SPT set-up. Different initial nanobead concentrations in the apical compartment were tested and the reproducibility of the method was determined.

##### **Initial nanobead concentration**

The initial nanobead concentrations in the apical compartment were:  $5 \times 10^9$ ,  $5 \times 10^{10}$  and  $5 \times 10^{11}$  nanobeads/mL. It is known from the nanobead concentration range discussed in Section 4.1.1 that the number of nanobeads in the detection volume for  $5 \times 10^9$  nanobeads/mL was on average 14. The apical compartment contained a volume of  $100 \mu\text{L}$  and the basolateral compartment  $600 \mu\text{L}$ . If there would be an equilibrium in the concentration between the apical and basolateral compartment, the concentration of nanobeads would be diluted 6 times. For an initial concentration of  $5 \times 10^9$  nanobeads/mL, this would lead to an average of approximately 2 particles in the detection volume of the basolateral compartment. For  $5 \times 10^{10}$  nanobeads/mL this would be 20 and for  $5 \times 10^{11}$  nanobeads/mL 200.

Figure 4.5 shows the concentration of nanobeads in the detection volume over time for the three different initial concentrations. The moving average over 8 time points is depicted to smooth out the data, to remove noise and to better expose the trend of the data. The graphs in Figure 4.5 show an increase of concentration in the detection volume. For  $5 \times 10^9$  and  $5 \times 10^{10}$  nanobeads/mL, the increase was followed by a decrease in the concentration. The shape of these graphs could be explained by the diffusion front of the nanobeads. This is described in detail in the next section about the reproducibility of this method. The time at which the concentration starts increasing, depends on the position of the detection volume. This will also be explained in the next section.

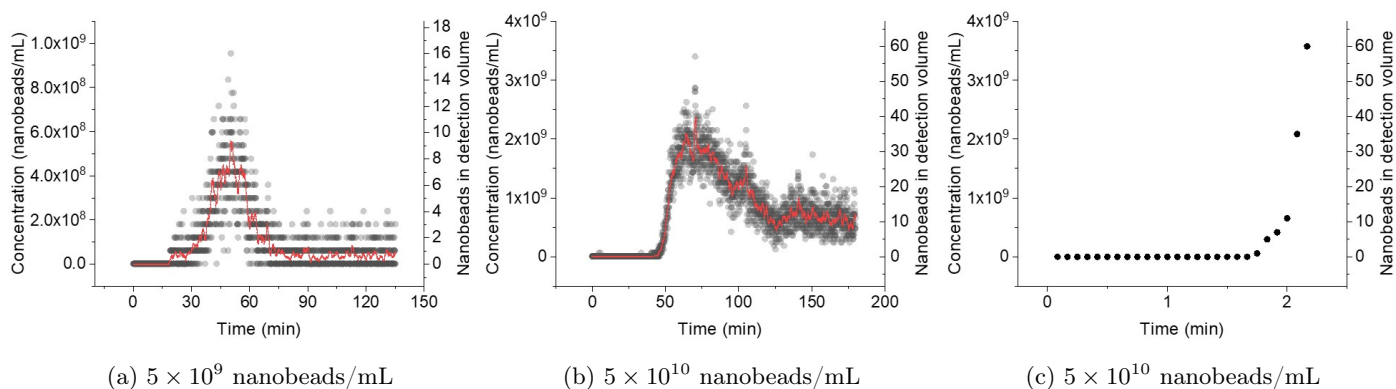


Figure 4.5: Concentration of nanobeads in the basolateral compartment for three different initial concentrations.

The left y-axis in the graphs shows the concentration of nanobeads in nanobeads/mL. The right y-axis shows the number of nanobeads calculated with the dimensions of the detection volume. The dots show data points, and the black lines are the moving average over 8 data points. In (a), the concentration was  $5 \times 10^9$  nanobeads/mL, in (b)  $5 \times 10^{10}$  nanobeads/mL and in (c)  $5 \times 10^{11}$  nanobeads/mL.

After the decrease of concentration of nanobeads, the concentration seems to reach a plateau. For  $5 \times 10^9$  nanobeads/mL in Figure 4.5a this plateau was approximately at 0.66 nanobeads in the detection volume. For  $5 \times 10^{10}$  in Figure 4.5b this plateau was at 11 nanobeads in the detection volume. Previously it was described that the final number of nanobeads in the detection volume for  $5 \times 10^9$  nanobeads/mL is expected to be 2 and for  $5 \times 10^{10}$  nanobeads/mL 20. This means that the measured number of particles in the detection volume at the plateau was within the order of magnitude of what was expected. However, the measured number of nanobeads were a bit lower than expected. This may be due to the nanobeads attaching to the membrane or sides and bottom of the wells plate and the holder of the transwell membrane.

Figure 4.5c shows that with an initial concentration of  $5 \times 10^{11}$  nanobeads/mL, there is a relatively fast and steep increase of concentration in the detection volume. After the number of nanobeads in the detection volume reaches approximately 60, the captures were overexposed, so the number of nanobeads in the detection volume could no longer be determined.

### Reproducibility of the real-time measurements

Figure 4.6a shows the concentration of nanobeads in the basolateral compartment over time of two measurements. The initial concentration for both measurements was  $5 \times 10^{10}$  nanobeads/mL. The data points and the moving average over 8 data points are shown. The experimental conditions of the two measurements were equal. It was attempted to keep the detection position constant in between measurements. However, obtaining the exact same position was difficult because of the small detection volume compared to the basolateral compartment.

The graphs in Figure 4.6a show that there is an increase in the concentration of nanobeads in the basolateral compartment. This was expected because of nanobeads permeating through the transwell membrane and diffusing towards the detection volume. There is also a decrease of concentration for measurement 1, which was also observed before in Figure 4.5a and 4.5b. The shape of these graphs can be explained by looking at the concentration profile, as depicted in Figure 4.6b. In this figure, the y-axis depicts the concentration of particles at position  $x$ .  $t$  indicates different time points. At  $t=0$ , a substance was added

to the origin at a certain  $x$ -position. In this experiment, the origin was the nanobeads in the transwell membrane. The concentration spreads out with time. When looking at one position, for example the blue line that depicts 1, there are at  $t=0$  no particles, while at  $t=2$  the concentration of particles increases. At  $t=10$ , the concentration decreases again.

Another observation in Figure 4.6a was that the change in the concentration of nanobeads over time was different for measurement 1 compared to measurement 2, while the experimental conditions were kept constant. The first difference is that the increase of concentration in measurement 1 is more steep compared to measurement 2. Next, the concentration in measurement 1 increases around 22 minutes. For measurement 2, this is around 30 minutes. These differences can also be explained by looking at the concentration profile depicted in Figure 4.6b. If the position of detection is closer to the origin, the increase of nanobeads occurs earlier and faster than when the position of detection is further away from the origin. This is indicated in Figure 4.6b, where at  $t=1$  the concentration of particles start to increase for measurement 1, at that time point, the concentration for measurement 2 is still 0. This indicates that the increase of concentration depends on the position of detection.

To calculate the apparent permeability, it was necessary to know the change in the concentration of nanobeads over time ( $dC/dt$ ) in the basolateral compartment. Figure 4.6a shows that it is not possible to obtain  $dC/dt$  from the real-time measurements, as the method depends on the exact location of the detection position. To determine the apparent permeability of the cell model, another method was used, which will be described in the next section.

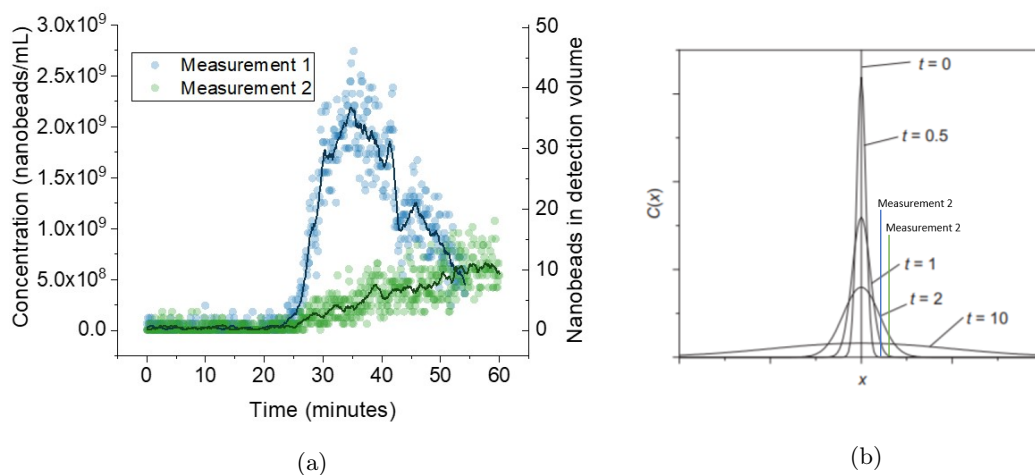


Figure 4.6: (a) Concentration of nanobeads in the basolateral compartment over time. The dots show data points, and the black lines are the moving average over 8 data points. Measurement 1 and 2 are measured in the same experimental conditions, only the location in the basolateral space was different. (b) Concentration profile versus location  $x$  due to diffusion after a substance initially only present at an origin.

The different curves show the concentration profile at different time points [96].

#### 4.1.5 Permeation of PS nanobeads through the Caco-2 cell model

The real-time measurements were not found to be reproducible due to difficulties in keeping a constant detection position. Another, more reproducible, experiment will be explained in the next section. However, the real-time method could be used to get a qualitative idea about the permeation of nanobeads through the cell barrier. For the quantification of the permeability, another measuring method was used, this will be explained at the end of this Section.

For the qualitative analysis, Caco-2 cells were cultured for at least 21 days on a transwell membrane. During measuring of the concentration of nanobeads in the basolateral compartment, the wells-plate with the transwell membrane was kept at the SPT set-up and every 5 seconds a capture was made from the basolateral compartment. The Caco-2 cells were treated with 20 nm PS-beads at a concentration of  $5 \times 10^{11}$  nanobeads/mL. This concentration was chosen, as it did not decrease the viability of the Caco-2 cells. Furthermore, it is expected that the concentration is high enough to observe nanobeads in the basolateral compartment, even if the permeability appears to be low. Caco-2 cells treated with EGTA were used as a positive control, as EGTA leads to an increased permeability of the cell layer. EGTA is a chelating agent for  $\text{Ca}^{2+}$ , which is involved in the assembly and sealing of TJ [97]. EGTA is more often used in literature as a positive control in permeability studies of epithelial barriers. In these studies, the treatment of EGTA was done at a concentration of 3-4 mM for 30 minutes [26, 98].

Figure 4.7a shows the concentration of nanobeads in the basolateral compartment over time for the Caco-2 model and for the Caco-2 model treated with EGTA. Without treatment of EGTA, nanobeads could not permeate the Caco-2 model within 90 minutes. After 4 hours of 8 mM EGTA treatment, nanobeads were detected in the detection volume. Shorter treatments did not lead to an increased permeability, which is contradictory to literature, where lower concentrations of EGTA were used. It is not known why the beads could not permeate the Caco-2 models treated with EGTA for 1 and 2 hours. With the treatment of 4 hours at a concentration of 8 mM the cell barrier was no longer intact, which can be seen in Figure 4.7b and 4.7c. Here, it is expected that the nanobeads can freely diffuse via unrestricted transport.

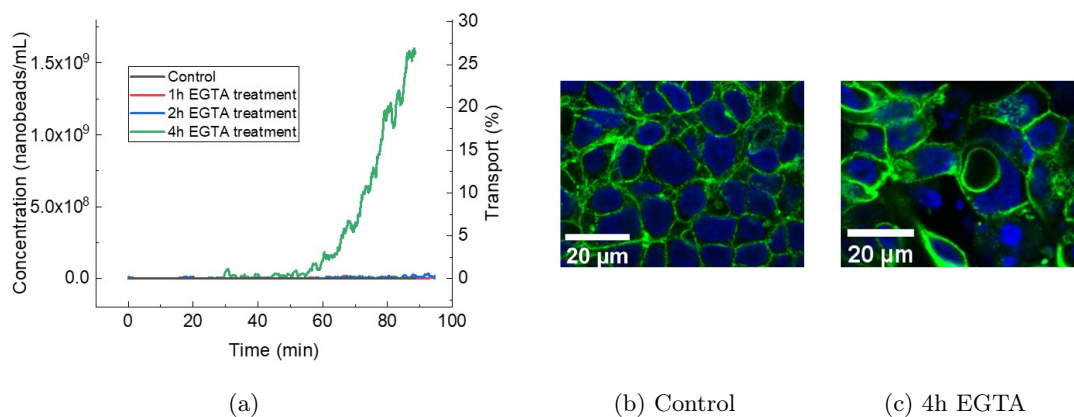


Figure 4.7: (a) Concentration and percentage transport of nanobeads in the basolateral compartment of the Caco-2 model and for the model treated with EGTA, measured with the real-time method. (b) and (c) Microscopic images of a control cell layer and a cell layer treated with EGTA for 4 hours. Green is F-actin and blue cell nucleus.

From the results of this permeability experiment, it seemed as if the pores between the Caco-2 cells are not large enough to allow transport of the PS nanobeads. This indicates that the nanobeads used in this research cannot transport via the paracellular pathway. In literature, the diameter of particles that can use the paracellular leaky pathway is not precisely defined but the maximum range of particles is thought to be in the range of 10-20 nm [32, 39, 40]. The diameter of the nanobeads used in this research is within this range, so the results correspond to literature. There are more factors that are important for transport via the paracellular pathway, such as charge. This could be further examined by using different surface modifications of 20 nm PS beads.

As mentioned earlier, the real-time permeability measurements were not reproducible. Next to this, the real-time measurements could not be performed for longer than approximately 2 hours, because it was possible that the Caco-2 cells behave differently at non-physiological temperature and CO<sub>2</sub>-levels. It was also possible that cells might detach from the transwell membrane. Because of these reasons, the experimental conditions were changed to determine the apparent permeability for the nanobeads through the Caco-2 model.

In the experimental condition that was tested next, the wells plate containing the transwell membrane was placed on a shake-plate during the treatment with nanobeads. When performing the experiment in this way,  $dC/dt$  was no longer dependent on the location of detection, as the nanobead concentration throughout the entire basolateral compartment was equal. Next to this, in literature it was found that without shaking of the transwell membrane, an unstirred water layer can be formed, which could decrease the permeability compared to the *in vivo* permeability [99]. Shaking was done at 150 rpm. By placing the transwell in the incubator, the experiment could be performed for longer than 2 hours, as the conditions in the incubator were 37°C and 95% atmospheric O<sub>2</sub> and 5% CO<sub>2</sub>. The same concentration of nanobeads as with the real-time measurements was used, because it was still expected that the permeability will be low and the concentration of  $5 \times 10^{11}$  nanobeads/mL nanobeads/mL appeared not to decrease the viability.

An experimental condition was added to examine the change of permeability during the differentiation process of the Caco-2 cells. This was done to examine if differentiated Caco-2 cells and undifferentiated Caco-2 cells show different permeability characteristics. The permeability of the cell model of Caco-2 cells that were cultured for 7 and 14 days were tested, next to the cell model of 21 days. The Caco-2 cells need approximately 21 days for the differentiation of carcinoma cells into enterocytes [46, 47]. Appendix Figure B1 shows that on day 7 after seeding, the cell confluence was 100%, so it was not possible for the nanobeads to diffuse freely to the basolateral compartment. It was assumed that the main difference between the conditions was that Caco-2 cells on day 7 were not differentiated, on day 14 some Caco-2 cells might be differentiated and on day 21 the Caco-2 cells were mostly differentiated.

Figure 4.8 shows the increase of concentration of nanobeads in the basolateral compartment over time for Caco-2 cells after 7, 14 and 21 days of seeding. The left y-axis shows the concentration in the basolateral compartment in nanobeads/mL. The right y-axis shows the percentage of nanobeads which was transported. 100% transport indicates an equilibrium in the concentration between the apical and basolateral compartment. The dilution from 100  $\mu\text{L}$  to 600  $\mu\text{L}$  from the apical to basolateral compartment was taken into account, as described in Chapter 3.2.2. The experiment could not be performed for longer than 72 hours, because after 72 hours, the culture medium should be refreshed. Next to this, effects on the cell viability due to exposure to nanobeads were not known for exposure longer than 72 hours.

For the Caco-2 cells that are cultured for 21 days, the concentration of nanobeads after 72 hours of treatment was  $4 \times 10^8$  nanobeads/mL, which corresponds to a transport of 0.5%. This shows that the transport of nanobeads was very low. The concentration in the basolateral compartment was lower at all time points for Caco-2 cells that were cultured for 7 and 14 days, compared to day 21 Caco-2 cells. The results indicate that PS nanobeads were more easily translocated by Caco-2 cells that were mostly differentiated compared to cells that were undifferentiated. The results of this experiment are contradictory with literature, because it has been reported that in undifferentiated Caco-2 cells, fewer TJ-proteins are expressed, leading to an increased permeability [49]. A possible explanation for this could be that the mechanisms responsible for translocation of nanobeads in differentiated enterocytes were not present or less efficient in undifferentiated Caco-2 cells. However, the degree of differentiation was not tested in these experiments, so it is not certain that this explanation is correct. Next to testing the differentiation, further research is needed to verify the exact pathway of transport. This can be done for example with inhibitors for certain mechanisms in the transcellular route. Next to this, Transepithelial Electrical Resistance (TEER) values were not measured in this part of this research. This should also be done in further research, as cell layer integrity can influence the permeation characteristics. By measuring the TEER values of the Caco-2 layer, it can be verified whether the model is suitable to use. In the next section, the hypothesis about permeation across differentiated and undifferentiated Caco-2 cells was further tested by imaging the cell layer after exposure to nanobeads.

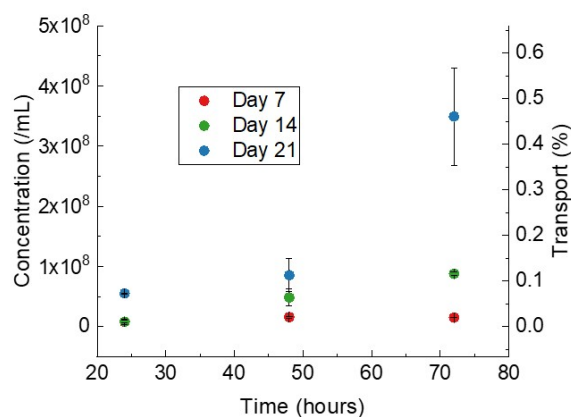


Figure 4.8: Concentration and transport (%) in the basolateral compartment of the Caco-2 model of 7, 14 and 21 days after seeding. The error bars represent the standard deviation of 3 replicates.

#### 4.1.6 Localization of the PS nanobeads in the Caco-2 cell layer

The Caco-2 cells that were treated with nanobeads for 72 hours were imaged with confocal laser scanning microscopy to find the location of the nanobeads within the Caco-2 cells. The cells of different seeding days and different Z-slices of these cell layers were compared. The Caco-2 cells were stained with DAPI (blue) for staining of the nuclei and AF488-phalloidin (green) for staining of F-actin filaments. The nanobeads were ‘dark red’ FluoSpheres, so they appear red in the images.

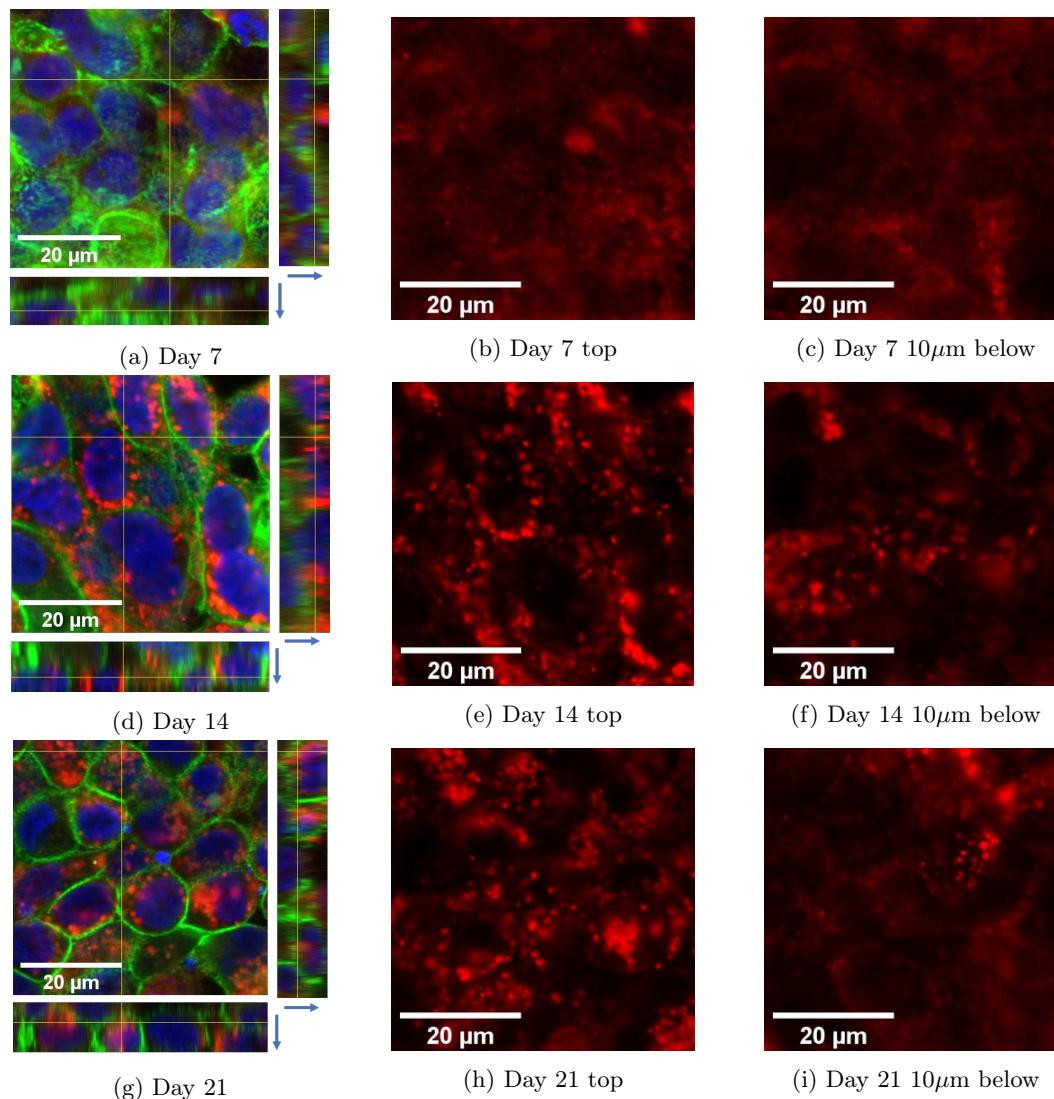


Figure 4.9: Images and orthogonal views of cell layers of the Caco-2 cell model after 7 (a-c), 14 (d-f) and 21 (g-i) days after seeding. Green is F-actin, blue is cell nucleus and red are the nanobeads. The captions show how many days the Caco-2 cells have been cultured before nanobead exposure. Top indicates images of a slice in the top of the cell layer and bottom from 10  $\mu\text{m}$  deeper into the cell layer. Arrows point towards the top of the cell layer.

Figure 4.9a, 4.9d and 4.9g show confocal images and orthogonal views of the Caco-2 cell models of 7, 14 and 21 days after seeding. The Caco-2 cell layers were exposed to nanobeads for 72 hours at a concentration of  $5 \times 10^{11}$  nanobeads/mL. The images represent the cell layer well. Figure 4.9b, 4.9e and 4.9h show the nanobeads at the ‘top’ side, or the apical side, of the cell layer. Figure 4.9c, 4.9f and 4.9i show nanobeads 10  $\mu\text{m}$  deeper into the cell layer. All of the images show the presence of nanobeads, which corresponds to the uptake of PS nanobeads reported in literature [29, 30].

Nanobeads in the Caco-2 cells that were cultured for 7 days were evenly distributed over the cells, whereas the images of day 14 and day 21 Caco-2 cells show some bright spots. These bright spots are most likely aggregates of nanobeads. The aggregates were also visible in deeper regions in the cell models of 14 and 21 days. The SPT measurements described in Section 4.1.1 show that in solution, the nanobeads were not aggregating, so the nanobeads accumulated within the Caco-2 cells. From these images, it seems as if differentiated Caco-2 cells (day 21) take up more nanobeads than undifferentiated Caco-2 cells (day 7). Transport mechanisms for nanobeads may be less efficient in undifferentiated Caco-2 cells, compared to differentiated Caco-2 cells, which corresponds to the hypothesis that was described in Section 4.1.5 about the apparent permeability of nanobeads. However, these images are not direct evidence of the absence or presence of transport mechanisms. Next to this, the difference in the uptake between differentiated and undifferentiated Caco-2 cells was not found in literature search, so it should be further examined.

As described before, there was no decrease in the Caco-2 cell viability observed at a concentration of  $5 \times 10^{11}$  nanobeads/mL after 72 hours. It is remarkable that there was no decrease in the viability observed because the confocal images from Figure 4.9 show that the Caco-2 internalized the PS nanobeads. The PS nanobeads are probably inert, but take up quite some space within the Caco-2. This could eventually have adverse long-term effects to cell and barrier function. Next to this, in *in vivo* situations, this could mean that the nanobeads can be distributed into other organs [29]. Examining the long-term effects of nanobeads on Caco-2 cells or other cell types is interesting to further examine, as nanoplastics are found in nature due to plastic pollutants [30]. This is, however, outside the scope of this research.

#### 4.1.7 Concluding remarks

As a first step towards developing a methodology to quantify the permeability of the *in vitro* cell models of the epithelial intestinal barriers, PS nanobeads were used. The hydrodynamic diameter of the nanobeads was 23.0 nm and the height of the nanobeads in AFM images was 16.9 nm. The lowest concentration of nanobeads that could be detected, within the chosen measuring time with SPT, was  $2 \times 10^7$  nanobeads/mL. The viability of Caco-2 cells was not decreased by exposure to PS nanobeads at the concentration used for the permeability experiments.

The permeability experiments were performed on the SPT set-up and different experimental conditions were tested. First, the concentration of nanobeads in the basolateral compartment was attempted to be determined in real-time. The main drawback of this method was that measuring the concentration in real-time turned out to be not reproducible, as the increase in the concentration in the basolateral compartment depended on the position in the sample. It was not possible to measure at exactly the same position between different measurements. Another drawback was that the real-time method allowed a maximum measuring time of 2 hours, as it could not be performed in physiological conditions. This time was not long enough for the nanobeads to translocate through the Caco-2 model. The observation that no nanobeads entered the detection volume in the basolateral compartment, indicates that the pores between the Caco-2 do not allow transport of the nanobeads, so the nanobeads were too large for the paracellular pathway.

The second method allowed measuring times up to 72 hours. Shaking conditions were used to obtain an equal nanobead concentration throughout the basolateral compartment. This method appeared to be a good method in measuring the transport of PS nanobeads in the cell model. Unlike reported in literature, PS nanobeads permeated to a low extent in Caco-2 that were completely differentiated. Nanobeads accumulated inside the cytoplasm by the Caco-2. Permeation and accumulation of nanobeads were higher for completely differentiated cell layers compared to the undifferentiated Caco-2 cell layer. However, more research is needed to verify whether the Caco-2 cells were differentiated after 21 days of culturing. The results indicate that PS nanobeads translocated via the transcellular pathway. However, more research is needed to research the exact mechanism.

With the SPT set-up, it was possible to quantify the concentration of nanobeads that transported across the cell barrier. The next step in this research was to use the established method for the determination of permeability characteristics of amyloid fibrils in the *in vitro* cell models.

## 4.2 Amyloid fibrils

In this section, the permeation characteristics of two types of amyloid fibrils will be presented and discussed. The first type of amyloid fibril used in this research was lysozyme, which originated from hen egg-white. The second type of amyloid fibril was  $\alpha$ -Syn A53T, which was used as a model to mimic animal  $\alpha$ -Syn. It is assumed that the main difference between the two amyloid fibrils is the charge: lysozyme is net positively charged and  $\alpha$ -Syn A53T net negatively. In this section, the characterization of amyloid fibril length and morphology will be discussed. Secondly, the cell layer integrity during lysozyme and  $\alpha$ -Syn A53T exposure will be discussed. Next, the quantification of amyloid fibrils using several techniques, such as the SPT set-up and bulk fluorescence spectroscopy is explained. The permeability of lysozyme and  $\alpha$ -Syn A53T through the Caco-2 model and the Caco-2+HT29MTX cell model will be presented. The Caco-2+HT29MTX cell model is added to test the effect of mucus on the permeation of amyloid fibrils. Furthermore, the Caco-2+HT29MTX cell model is a more close representation of the *in vivo* situation than the Caco-2 model. Finally, the identification of fibrils, monomers and free dye is discussed.

### 4.2.1 Length and morphology of amyloid fibrils

The ability of a substance to cross the epithelial barrier depends on many characteristics of the substance such as size, morphology, surface charge, hydrophobicity, and the potential to form interactions with proteins of the cell plasma membrane [38, 95]. Not all properties were examined in this project, as the main focus was the charge of amyloid fibrils. To understand the role of charge in permeability characteristics, it was important to keep the other amyloid fibril properties, such as size, constant as much as possible. With ultra-sound sonication, the fibrils can be fragmented into smaller fibrils and by varying the time of sonication, it was possible to obtain different lengths of fibrils. By doing this, the amyloid fibril length can be controlled and kept equal for both types of amyloid fibrils.

Figure 4.10 shows AFM images of lysozyme and  $\alpha$ -Syn A53T fibrils. The fibrils were diluted in fresh cell culture medium containing 20% Fetal Bovine Serum (FBS). The concentration of fibrils used for AFM was 10  $\mu$ M. Lysozyme fibrils that were sonicated for 4 minutes in an ultrasound-bath sonicator had an average length of  $116 \pm 63$  nm. The variation in length can be seen in Figure 4.10b. Next to small fibrils, there were also aggregates of fibrils, depicted in the white circles. In  $\alpha$ -Syn A53T fibrils in Figure 4.10d, this aggregation was not observed. There are some white spots, which is probably due to how crowded the fibrils on the image are. The length of  $\alpha$ -Syn A53T fibrils after 4 minutes of sonication was  $355 \pm 176$  nm. Longer sonication times were tested for  $\alpha$ -Syn A53T, as the length for both fibril types should be similar. Figure 4.10c shows the mean fibril length for  $\alpha$ -Syn A53T at different sonication times and for lysozyme for 4 minutes of sonication. The average length of  $\alpha$ -Syn A53T at 10 minutes sonication was  $118 \pm 52$  nm, so this was used for the permeability experiments.

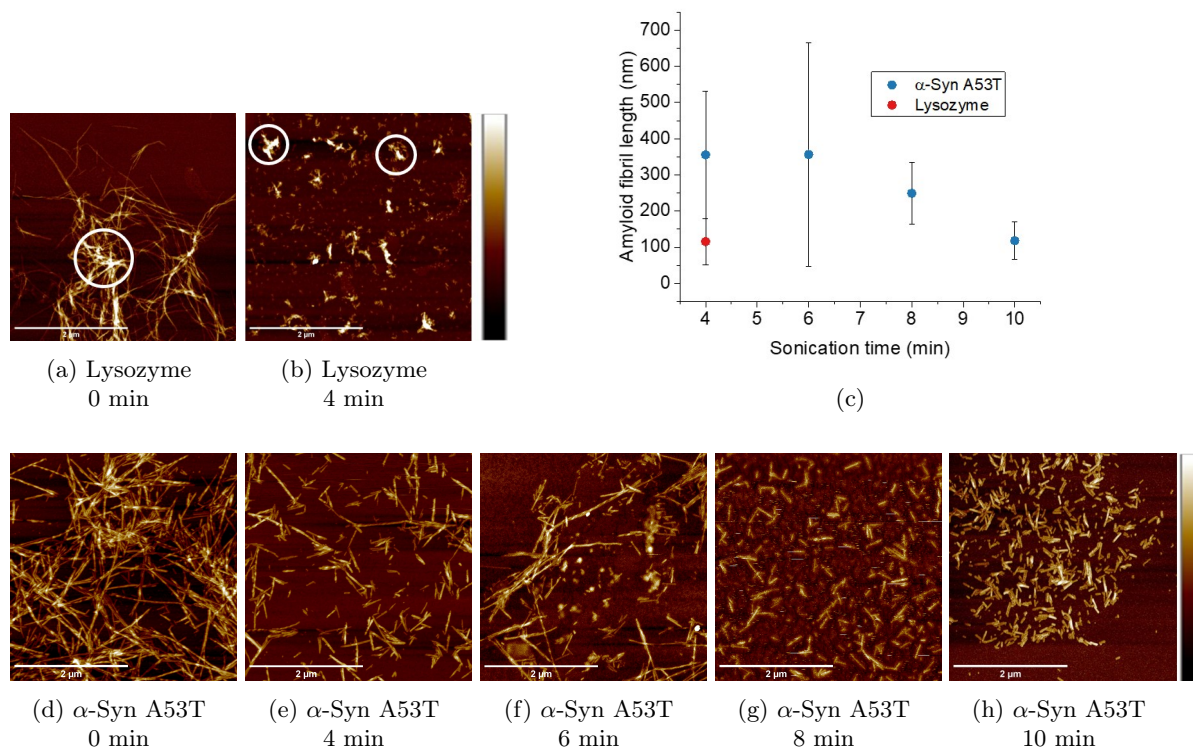


Figure 4.10: AFM images of amyloid fibrils at different sonication times. (a) unsonicated lysozyme fibrils, (b) lysozyme fibrils at 4 minutes. White circles show lysozyme fibrils aggregating. (c) The mean length of the amyloid fibrils at different sonication times. The error bars show the standard deviation of the measurements of 50 fibrils. (d)  $\alpha$ -Syn A53T unsonicated fibrils.  $\alpha$ -Syn A53T fibrils were sonicated for 4 minutes (e), 6 minutes (f), 8 minutes (g) and 10 minutes (h).

As mentioned, lysozyme fibrils seem to aggregate to larger fibril-aggregates. Figure 4.10h shows that  $\alpha$ -Syn A53T fibrils did not aggregate to larger non-fibrillar structures. Aggregation of fibrils can occur in the same way as proteins bind to other proteins. This can be a combination of hydrophobic interactions, Van der Waals forces, and salt bridges at binding domains on each protein [1]. From the AFM images, it seemed as if lysozyme can more easily form these interactions, compared to  $\alpha$ -Syn A53T. However, in the presence of enzymes and proteins secreted by the cells, lysozyme and  $\alpha$ -Syn A53T fibrils might have other size and morphology characteristics compared to freshly diluted in cell culture medium. The incubation temperature of 37°C during the experiment could also alter size and morphology. Unravelling the nature of the physicochemical interactions between proteins secreted by cells and lysozyme and  $\alpha$ -Syn A53T were not examined in this research. However, it is important to note that this may influence the permeability, as size and morphology are crucial characteristics for the permeation.

#### 4.2.2 Cell layer integrity: Transepithelial Electrical Resistance

Transepithelial Electrical Resistance (TEER) values were measured to validate that the cell layer was intact. An intact cell layer was important, as a disruption in the cell layer will lead to a wrong interpretation of the permeability. Next to this, TEER values were measured during exposure to amyloid fibrils to check if amyloid fibrils influence the cell layer integrity. Disruption in cell layer integrity might indicate that tight junction (TJ) complexes are disrupted. If amyloid fibrils can disrupt TJ-complexes, the permeability of the cell barrier may be increased.

In literature, it is reported that Caco-2 cells express more TJ-proteins than HT29MTX cells, so ionic conductance across a Caco-2 cell barrier is lower than across a cell barrier containing HT29MTX cells [56]. This leads to higher TEER values in Caco-2 cell layers than in co-cultures [44, 53]. TEER values can vary from lab to lab because of the heterogeneity of the cell lines [45, 57], but mostly TEER values for Caco-2 layers are reported in literature to be 150-400  $\Omega \times cm^2$  after 21 days of culturing [45]. For co-cultures with Caco-2 and HT29MTX, the TEER values depend on the seeding ratio, but are always lower than solely Caco-2 cells. The TEER values should be monitored during culturing. When the TEER values reach a plateau, the cell layer can be used for testing [45, 57].

Figure 4.11 shows TEER values for the Caco-2 model and Caco-2+HT29MTX model. Three different seeding days are shown: 1, 2 and 3. The cell layers of moment 1 were used for the permeability studies with  $\alpha$ -Syn A53T and the TEER experiment during exposure to  $\alpha$ -Syn A53T. The cell layers of moment 3 were used for the TEER experiments with treatment of lysozyme. Moment 2 was added to confirm the permeability results, as the TEER values were initially not measured for the cell layers used for the lysozyme permeability experiments. The TEER values of all cell layers increased over time, indicating that the layers became 100% confluent, that there was formation of TJ-complexes and that the cell layers remained intact.

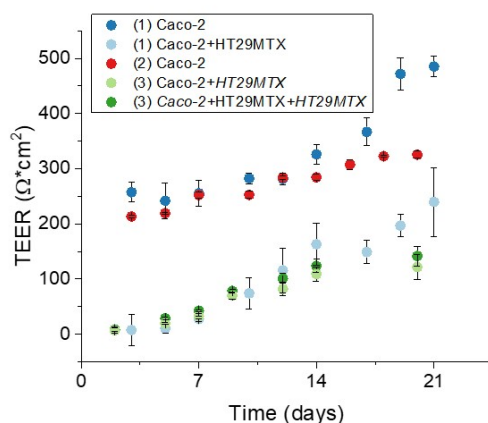


Figure 4.11: TEER values of Caco-2 cells and Caco-2+HT29MTX co-culture of different seeding moments 1, 2 and 3 over 21 days. TEER values are corrected for a blank measurement and the area of a transwell membrane. The ratio of HT29MTX cells to Caco-2 cells in the co-culture at moment 1 was 1:3. The cell layers of moment 1 probably contained an excess of HT29MTX cells by contamination of HT29MTX cells in the master's plate of Caco-2 cells. For moment 1 n=7, for 2 n=2 and for 3 n= 4.

The standard deviations show that there was not much variation between the replicates in one condition. However, there are differences visible between the seeding days, for instance the difference between moment 1 and moment 2. This shows that cell layers can have different properties when cultured on other seeding days. This could be due to different passage, somewhat different seeding densities or other differences in culturing and handling in the lab. For 1 and 2, there was a difference in TEER values between Caco-2 cells and the co-culture. For the third seeding moment 3, there was no difference in TEER values between the two models. Decreased TEER values in Caco-2 cell layer may indicate that the cells were not able to form TJ-complexes, for example a high cell passage or a mutation in the cells [45]. Another possibility is that HT29MTX cells were translocated to the Caco-2 membranes during handling in the lab. As the TEER values were low for all transwells in this condition, it is expected that the HT29MTX contaminated the Caco-2 master-plate. This was further examined with an Alcian blue staining described at the end of this section. If the Caco-2 master plate contained HT29MTX cells, it can be assumed that the co-culture transwell also contained relatively more HT29MTX cells. The exact ratio of Caco-2 and HT29MTX cells in both models was difficult to access. These cell layers were used for measuring the cell layer integrity during exposure to lysozyme. The effect of the excess of HT29MTX cells in this experiment will be discussed later in this section.

TEER values were measured during treatment of lysozyme and  $\alpha$ -Syn A53T fibrils, to examine if the amyloid fibrils would influence the cell integrity. Figure 4.12 shows the corrected TEER values of cell layers exposed to  $2.5 \mu\text{M}$  lysozyme and  $\alpha$ -Syn A53T fibrils. The graphs show the change in TEER values, which is depicted as the percentage change compared to the TEER value before exposure to amyloid fibrils on day 0. The treated cell layers were cultured for 21 days. For lysozyme, the Caco-2 cells which were contaminated with HT29MTX cells were used. This means that the Caco-2 cell layer and the co-culture contained an excess of HT29MTX cells. By using a control group, it was still possible to test the effect of amyloid fibrils on cell layer integrity for the Caco-2+HT29MTX model. Though, because of the excess of HT29MTX cells, the model was different from the model used in the permeability studies, which will be discussed in Section 4.2.4.

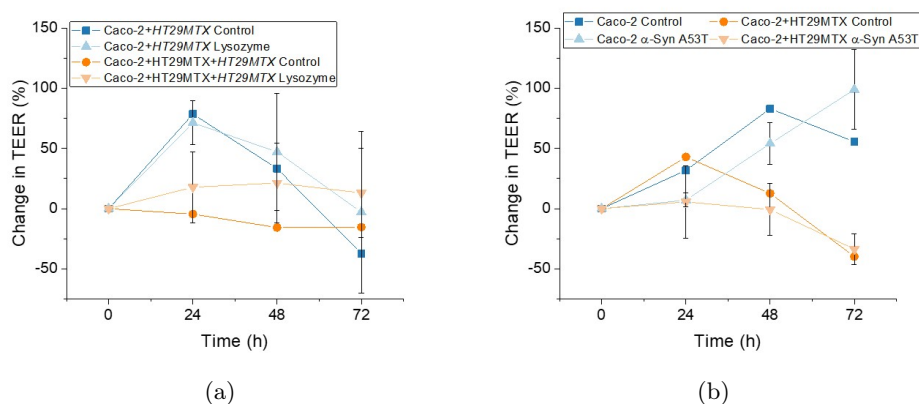


Figure 4.12: Change of TEER values across the Caco-2 and Caco-2+HT29MTX cells. The change in TEER was the percentage difference compared to the initial TEER value on day 0. The error bars show the standard deviation of 3 replicates.

One transwell containing cells was used for the control group, as it was assumed that there would not be a change in TEER values after 21 days. This appeared not to be true in all cases. The graphs in Figure 4.12 show that the TEER values of the control transwell membrane did not remain constant after 21 days of culturing. For instance, Figure 4.12b shows that the TEER values of the Caco-2 cells at 48 hours increase to almost 100% compared to the TEER values of day 0. This represents a difference of approximately  $300 \Omega \times cm^2$ . For the co-culture, the TEER values even decreased to -50% compared to day 0, which was a decrease of approximately  $100 \Omega \times cm^2$ . The fluctuations were not visible in Figure 4.11. It is not completely sure why these relatively large changes were visible in the control group. Despite the fluctuations of the control group, it is still possible to compare the control group to the treated cell layer to get a broad view of the influence of amyloid fibrils on cell layer integrity.

Overall, the treated cell layers follow the same trend as the control transwell, as the standard deviation of the treated group overlaps with the TEER values of the control group. This indicates that there was no change in TEER values after exposure to amyloid fibrils. However, due to the altered ratio of Caco-2 and HT29MTX cells in the lysozyme-experiments, the data might differ from for the ratio used in the permeability experiments.

In literature, it was reported that amyloid fibrils could weaken TJ-complexes by disruption of proteins such as ZO-1 and occludin [18, 19]. It is expected that this would influence the TEER values of the cell models. However, Kuan et al. found that after treatment of  $\alpha$ -Syn fibrils, there was no change in TEER values detected [18]. Moreover, Itallie et al. found that depletion of ZO-1 does not necessarily compromise the electrical barrier [100]. In this study, Itallie et al. hypothesized that the TJ-complex is arranged as a series of multiple cell-cell connections. These multiple connections still provide a barrier in case individual TJ might break. The results previously described show that there was no decrease in TEER values during exposure to amyloid fibrils, which indicates that lysozyme and  $\alpha$ -Syn A53T exposure does not influence the overall cell layer integrity. Individual TJ-proteins might be depleted, but this does not seem to influence the simultaneous loss of all TJ-complexes in the cell layer in the cell models used. More research is necessary to find the effect of lysozyme and  $\alpha$ -Syn A53T fibrils on TJ-proteins, as it was shown before that amyloid fibrils could facilitate their own movement over an epithelial barrier by decreasing TJ-proteins levels [16].

### Alcian Blue staining

An Alcian Blue staining was performed to qualitatively see the difference in mucus secretion between Caco-2 cells and HT29MTX cells. The Alcian staining was performed on the co-culture and on the mono-culture of Caco-2 cells that showed low TEER values. With the Alcian Blue staining, it was possible to check whether the Caco-2 layer was indeed contaminated with HT29MTX cells. Mucus is a gel-like structure composed of water, ions, proteins and macromolecules. The major macromolecular component of mucus is the glycoprotein mucin [34]. Mucus is secreted by goblet cells, such as HT29MTX cells [31, 50]. In a co-culture cell layer, the mucus is stained blue. In a Caco-2 cell layer, there is no mucus present, so the cell layer should remain colorless after a staining with Alcian Blue. A counter-staining of Eosin was performed to show the presence of cells [26, 44]. Eosin is a pink staining, so with this counter staining the Caco-2 layer should be pink and the Caco-2+HT29MTX cell layer purple.

Figure 4.13 shows the transwell membranes that were cut out of the holder and stained with Alcian Blue and Eosin. Without Eosin staining, all of the membranes appeared blue. Unfortunately, no image was made from the membranes without Eosin staining. The top row in Figure 4.13 are membranes containing Caco-2 cells and the bottom row contained Caco-2+HT29MTX cells. There was no color difference between the two models. This shows again that this Caco-2 cell model probably was contaminated with HT29MTX cells. Two different fixation protocols were tested, the left image in Figure

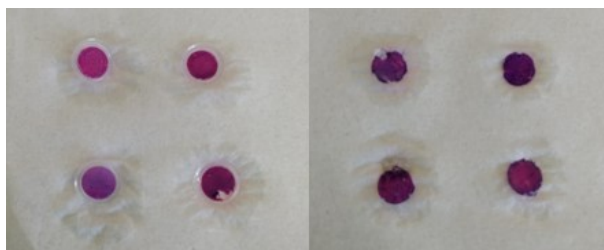


Figure 4.13: Transwell membranes with Caco-2 cells (top row) and Caco-2+HT29MTX (bottom row) stained with Alcian Blue and Eosin. The cells were fixed with PFA (left) and methacarn (right).

4.13 shows fixation with Paraformaldehyde (PFA) and the right image with methacarn. Methacarn (60% methanol, 30% chloroform, 10% acetic acid) is more often used to fix HT29MTX cells [101] and is believed to preserve mucus better than PFA. However, it was observed that the mucus layer may detach from the cells [102]. Figure 4.13 shows that detachment did not happen, as all membranes appear purple, indicating the membranes contain mucus. There was no large difference in the intensity of Alcian Blue and Eosin staining, so this indicates that there was no difference between the fixation methods.

To summarize, the Caco-2 and Caco-2+HT29MTX cell layers that were used for the permeability studies showed increased TEER values that corresponded to the values reported in literature. During exposure of lysozyme and  $\alpha$ -Syn A53T fibrils, the TEER values did not change compared to the control, so it is assumed that the cell layer integrity is not changed significantly by amyloid fibril exposure. However, the cell layer that was used for the lysozyme exposure experiment was performed on cell layers that contained an excess of HT29MTX cells, which was also confirmed with an Alcian Blue staining.

### 4.2.3 Quantification of the concentration of amyloid fibrils

To determine the apparent permeability, the concentration of amyloid fibrils in the basolateral compartment should be monitored. For the preliminary model using nanobeads, Single Particle Tracking (SPT) was used. For amyloid fibrils, this method may be more difficult to perform because of the non-spherical morphology and heterogeneity in size. However, it was attempted to measure the concentration of amyloid fibrils in the SPT set-up, because with nanobeads it appeared that with SPT, low concentrations could be measured. Measuring low concentration is probably needed, as the cell layer appeared to be a tight layer that did not allow much transport of nanobeads. For amyloid fibrils, this may also be the case.

Figure 4.14a shows a capture of lysozyme fibrils and Figure 4.14b of  $\alpha$ -Syn A53T fibrils imaged with the SPT set-up. Lysozyme fibrils were sonicated for 4 minutes and  $\alpha$ -Syn A53T fibrils for 10 minutes, as these were the suitable sonication times to obtain equal fibril length. The fibrils were diluted in cell culture medium. There were different sized structures visible in the captures. The large structures indicate that the fibrils aggregate to larger structures in cell culture medium. For lysozyme, this was also visible in the AFM images, see the white circles in Figure 4.10b. From the AFM images, aggregation of  $\alpha$ -Syn A53T fibrils did not seem to occur, but apparently in fresh cell culture medium, there was aggregation. In this solution, it seems as if the structure was more thermodynamically stable when aggregated or in a folded state instead of fibrillar structures.

Next to the large structures, it was clear that in the background of the videos the signal seems to be flickering. This could be out-of-focus fibrils or very small structures, such as labelled lysozyme or  $\alpha$ -Syn A53T monomers, oligomers or small fibrils. The flickering was not seen in blank measurements without fibrils. The flickering occurs with a speed that was faster than out-of-focus signal of the large structures, so it is assumed that there were smaller structures in the solution. These small structures were not individually detectable as spots because they were not bright enough and the dynamic range of the camera was not large enough to capture small and large structures at the same time.

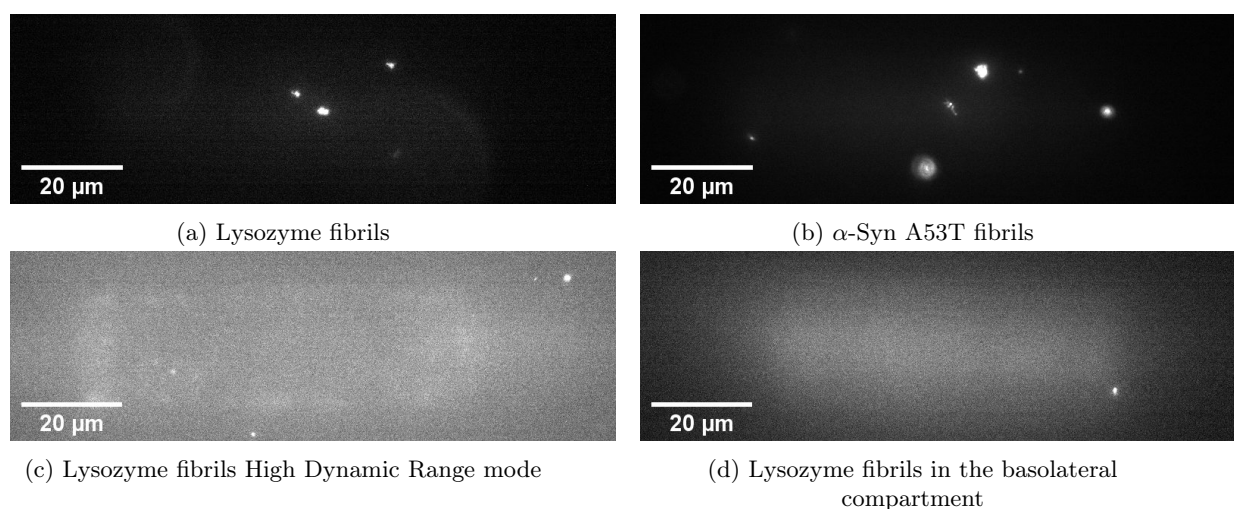


Figure 4.14: Captures of videos made with the SPT set-up. (a) Lysozyme fibrils sonicated for 4 minutes. (b)  $\alpha$ -Syn A53T fibrils sonicated for 10 minutes. (c) HDR image of amyloid fibrils. The exposure time was alternating between 5 ms and 50 ms. (d) A sample of the basolateral compartment of the Caco-2 model. The exposure time in (a), (b) and (c) was 5 ms.

In high dynamic range imaging (HDR), two exposure times are used to capture bright and less bright objects in the same video or image [103]. A short exposure time was used to visualize bright structures and a long exposure time to visualize dim structures. In HDR experiment, the exposure time was alternating between 5 ms and 50 ms. A region was imaged where no very large structures were present. Figure 4.14c shows a capture of a video of a solution of lysozyme fibrils. Some fibrils were distinguishable. However, the flickering was still present and the dimmer and smaller structures were not individually detectable by the tracking program Trackpy. The exposure time could not be further increased, as the distance travelled by the small particles would then be too large. This would result in the particles not being depicted in the captures as spots, but as lines.

Figure 4.14d shows a sample of the basolateral compartment of Caco-2 cells after exposure to lysozyme fibrils. There was one bright spot, which is thought to be a lysozyme fibril. In this video, the background was flickering. This indicates that smaller structures were present. This could be small fibrils, monomers or free dye. The same was observed in the basolateral compartment of  $\alpha$ -Syn A53T treated cells. An attempt was made to measure the mean gray value of these videos. It was possible to see a difference in gray values after different days of incubation with fibrils, but it was uncertain how the gray values correspond to the concentration. It was not possible to perform a calibration for this, because of the heterogeneity of the fibrils.

It was found that the SPT set-up was not suitable to quantify the concentration of amyloid fibrils in the samples because of the heterogeneity in size. It was decided to continue with bulk fluorescence spectroscopy. However, there are a few limitations in bulk spectroscopy.

The first drawback of bulk spectroscopy is that it is more difficult to measure low concentrations, especially with a low degree of labelling. For dim particles at a low concentration, the emission intensity in bulk fluorescence spectroscopy is low and becomes noisier. This makes it more difficult to accurately determine the exact concentration. Next to this, for bulk fluorescence spectroscopy, calibration is necessary with solutions with known concentrations. In SPT, calibration is not needed, but the exact dimensions of the detection volume should be known to determine the correct concentration. The final drawback of bulk fluorescence spectroscopy is that all dye molecules in the solution were taken into account. This was a disadvantage in this research, because it was important to know the aggregation state of the permeated lysozyme and  $\alpha$ -Syn A53T structures. The type of structure, such as fibrils or monomers, determine the ability to induce aggregation of disease-related proteins. Next to this, if the emission signal is originating from free dye present in the sample, the fibril concentration may be inflated. In the next paragraphs, it is explained how free dye, monomers and other structures could be present in the solution and why this may cause implication in this research.

Alexa Fluor 647 dye (AF647) was used for quantification of amyloid fibrils. Functionalized AF647 binds covalently to the primary amine of lysozyme and the cysteine of  $\alpha$ -Syn A53T. These bonds are known to be very stable [89, 91], so it is assumed that AF647 cannot detach from the amyloid fibrils. Ideally, the unattached dye was removed using Zeba Spin column during the labelling procedure. How-

ever, it could be possible that the removal during purification was incomplete and free dye was still present in the amyloid fibril solution. Free dye may permeate the cell barrier and cause an increase in emission signal in the basolateral samples, while no fibrils were present.

Lysozyme and  $\alpha$ -Syn A53T monomers and other small structures, such as oligomers, were removed during the labelling process by centrifugation. Some monomers could still be present in the solution after centrifugation because of incomplete removal. Next to this, monomers or oligomers could be present due to fibril disassembly upon exposure to cells. The goal of this research was to determine the permeability characteristics for amyloid fibrils, not for monomers, because it was expected that solely amyloid fibrils cause aggregation of disease-related amyloid forming proteins, such as  $\alpha$ -Syn wt monomers. However, for lysozyme this was not entirely the case, as the aggregation mechanism was based on the positive charge of lysozyme, so lysozyme monomers could also induce aggregation of  $\alpha$ -Syn wt. Aggregation induced by lysozyme monomers only occurs in suitable conditions, such as the concentration of salt. This will be explained in more detail in Section 4.2.5.

Even though bulk fluorescence spectroscopy likely does not give an accurate result for the reasons described above, it was still a useful technique to determine the apparent permeability of amyloid fibrils and monomers. This was done for both lysozyme and  $\alpha$ -Syn A53T across the mono- and co-culture. Furthermore, different techniques were exploited to distinguish between fibrils, monomers and free dye in the samples. First, Real-Time Quaking-induced Conversion was used to identify fibrils and monomers. Finally, Fluorescence Correlation Spectroscopy was exploited to test if free dye was present in the sample. Next to this, with FCS it was attempted to get an idea about the size of the particles to distinguish between larger structures, such as fibrils or oligomers and smaller monomers.

#### 4.2.4 Apparent permeability of amyloid fibrils in the Caco-2 and Caco-2+HT29MTX models

For the permeability experiments of amyloid fibrils, the established experimental condition for the nanobeads was used. The Caco-2 and Caco-2+HT29MTX cells were cultured on transwell membranes for at least 21 days. Hereafter, the cells were treated with 2.5  $\mu\text{M}$  lysozyme and  $\alpha\text{-Syn A53T}$  fibrils. This concentration was chosen, as it was within the range of detection of bulk fluorescence spectroscopy. Next to this, with a relatively high concentration in the apical compartment, it is still possible to measure the concentration of the diluted sample in the basolateral compartment. The treatment was done in 'shaking' conditions, meaning that the wells plate containing the transwell membranes was placed on a shake plate in an incubator. At certain time points, the concentration in the basolateral compartment was measured using bulk fluorescence spectroscopy. The basolateral samples were collected after 72 hours of treatment and used for analysis with AFM, RT-QuIC and FCS. 72 hours was chosen, as it is expected that the permeability of amyloid fibrils is not very high. By using a long treatment time, the concentration of fibrils in the basolateral compartment might be somewhat higher, so the presence of fibrils can be measured in AFM and RT-QuIC. Treatment time of more than 72 hours could not be done, because it is expected that this is the longest time that the cells were viable without refreshing the cell culture medium.

As discussed in Section 4.2.2, the TEER values of the Caco-2 cell layers used for the permeability experiments with lysozyme were not measured. Therefore, the bulk experiment was repeated with Caco-2 cells which had sufficient TEER values. The bulk experiment showed approximately the same results. The results of the first permeability experiment will be discussed, as more time points were measured, so a more reliable estimation of the apparent permeability could be made. For the permeability experiments of  $\alpha\text{-Syn A53T}$ , the cell layers of seeding moment 1 were used, which also had sufficient TEER values.

First, the basolateral samples were analyzed using AFM, to get an idea about the size and concentration of amyloid fibrils permeating through the model. It was attempted to visualize fibrils in the basolateral compartment of the cell models after 72 hours of exposure to 2.5  $\mu\text{M}$  lysozyme and  $\alpha\text{-Syn A53T}$  fibrils. With the dilution from the apical to the basolateral compartment, the expected concentration at equilibrium would be 0.42  $\mu\text{M}$ . This means that at equilibrium, the AFM images contained 20 times fewer fibrils than the AFM images in Figure 4.10. The AFM images in Figure 4.10 contained approximately 50-60 fibrils, so at a concentration of 0.42  $\mu\text{M}$ , each image still contains a few fibrils. No fibrils were found in the samples of the basolateral compartment, indicating that the concentration of fibrils was very low in the basolateral compartments. The basolateral samples were further analyzed using bulk fluorescence spectroscopy.

Next, the concentration of amyloid fibrils in the basolateral compartment was quantified by measuring the emission intensity of labelled amyloid fibrils. The emission intensity of known concentrations of amyloid fibrils was used to make a calibration curve. The calibration curve and some examples of emission spectra can be found in Appendix Figure C1. Figure 4.15a and 4.15b show the concentration in the basolateral compartment of lysozyme and  $\alpha\text{-Syn A53T}$  through an empty transwell membrane and through Caco-2 and Caco-2+HT29MTX models. First, the transport of an empty membrane is shown and discussed and thereafter the transport in the cell models.

### Transport of amyloid fibrils across the transwell membrane

It was expected that the transwell membrane does not contribute greatly to the apparent permeability of the cell layer, as the pore size of the membrane was  $3.0\ \mu\text{m}$  and the amyloid fibrils were around  $100\ \mu\text{m}$ . By measuring the transport over an empty transwell membrane, it can be verified if all fibrils were capable of crossing the membrane. The SPT images in Figure 4.14a and 4.14b showed that the amyloid fibrils could aggregate. It could be possible that these large structures cannot pass the transwell membrane. Next to this, binding of amyloid fibrils to the transwell membrane instead of transporting to the basolateral compartment was excluded with this experiment.

In Figure 4.15a, the transport of lysozyme and  $\alpha$ -Syn A53T across a transwell membrane is depicted in percentages. It is depicted in this way because the initial concentration of fibrils was slightly different for the two types of amyloid fibrils. This was not an issue for the calculations of the apparent permeability, as the concentration was corrected with the initial concentration in the calculations. In Figure 4.15a 100% transport indicates an equilibrium in the concentration between the apical and basolateral compartment. The dilution from  $100\ \mu\text{L}$  to  $600\ \mu\text{L}$  from the apical to basolateral compartment was taken into account, as described in Chapter 3. The apparent permeability was calculated from the fit of the data points of the first 60 minutes. The permeability of lysozyme fibrils to be somewhat lower than the permeability for  $\alpha$ -Syn A53T. A reason for this could be that lysozyme was more prone to aggregation, as discussed before. Because of aggregation, the transport over the membrane was slower. The transport of lysozyme and  $\alpha$ -Syn A53T approach 100% after 120 minutes. This indicates that most of the fibrils were able to cross the empty membrane. There may be some fibrils aggregating to large structures, or fibrils that attached to the membrane, as the transport was not reaching exactly 100%. However, this was only a small fraction, so it will not influence the apparent permeability much.

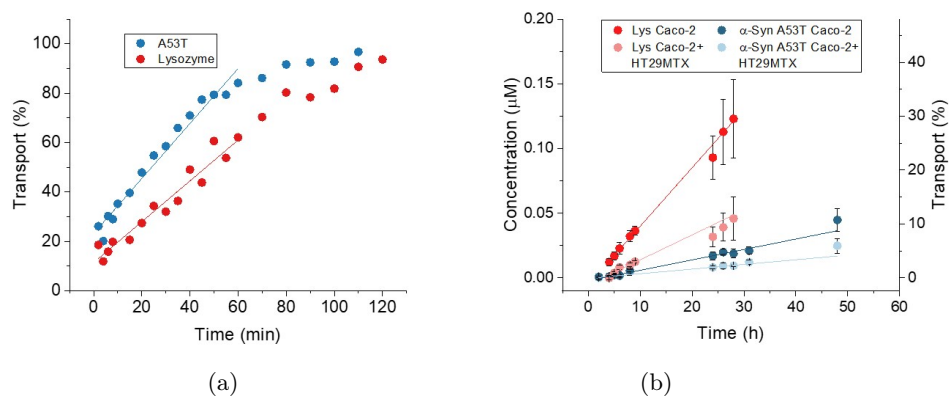


Figure 4.15: (a) Transport of lysozyme and  $\alpha$ -Syn A53T fibrils across an empty membrane transwells.  $R^2$  for the linear fit of lysozyme is 0.94 and for  $\alpha$ -Syn A53T 0.97. 100% indicates equilibrium between the apical and basolateral compartment. (b) Concentration of lysozyme and  $\alpha$ -Syn A53T in the basolateral compartment of the cell models.  $R^2$  of the linear fits was  $> 0.93$  for all fits. The error bars show the standard deviation of 3 replicates.

### Transport of amyloid fibrils across the cell models

Figure 4.15b shows the concentration of lysozyme and  $\alpha$ -Syn A53T in the basolateral compartment over time during exposure to 2.5  $\mu$ M amyloid fibrils. With a labelling ratio of 1:49 of labelled and unlabelled monomers in the fibrils, the lower detection limit of bulk fluorescence spectroscopy was approximately 1 nM. The concentration in the basolateral compartment for both types of amyloid fibrils exceeded 1 nM after 2 hours of treatment, so the detection range was suitable for these measurements.

The slope of the concentration of fibrils in the basolateral compartment versus time was used for the calculation of the apparent permeability. A high value for  $dC/dt$  indicates a high apparent permeability. A transport of 100% indicates an equilibrium in the concentration between the apical and basolateral compartment. For lysozyme, it was decided to finish the experiment after 28 hours, because if the transport would be too high, the concentration in the basolateral compartment reaches a plateau, because there would be no new supply of amyloid fibrils in the apical compartment. For  $\alpha$ -Syn A53T, the concentration was measured until 48 hours, to obtain a more reliable fit, as the concentration remained low. The apparent permeability of lysozyme and  $\alpha$ -Syn A53T fibrils in the cell models can be found in Table 1. It must be noted that this does not only include the permeability of amyloid fibrils, but possibly also of monomers, oligomers and free dye.

Table 1: Apparent permeability for lysozyme and  $\alpha$ -Syn A53T in the Caco-2 and Caco-2+HT29MTX cell layer

	<b>Caco-2</b>	<b>Caco-2+HT29MTX</b>
<b>Lysozyme</b>	$1.61 \times 10^{-7} \text{ cm/s}$	$6.86 \times 10^{-8} \text{ cm/s}$
<b><math>\alpha</math>-Syn A53T</b>	$2.81 \times 10^{-8} \text{ cm/s}$	$1.26 \times 10^{-8} \text{ cm/s}$

These results suggest that lysozyme fibrils can more easily translocate in the cell models than  $\alpha$ -Syn A53T fibrils. To evaluate this observation further, the uptake of lysozyme and  $\alpha$ -Syn A53T fibrils by the cells was examined using confocal microscopy. This will be discussed in Section 4.2.7. Next to this, the basolateral compartments were further examined using RT-QuIC and FCS.

The results also suggest that amyloid fibrils can translocate less efficiently in the co-culture model with Caco-2 and HT29MTX cells, compared to the Caco-2 model. In literature, contradictory results are reported about the difference in transport in Caco-2 models and co-culture with Caco-2 and HT29MTX cells, as described in Chapter 2. The TJ-proteins expressed by Caco-2 cells may lead to a decreased permeability in a mono-culture [26, 44, 53]. On the other hand, the mucus layer secreted by the HT29MTX cells may be an extra barrier for the substances [58]. This depends on several characteristics of the substance of interest. It is known that  $\alpha$ -Syn monomers can penetrate mucins despite their mucoadhesive properties [20]. However, it is possible that amyloid fibrils form interactions with mucins which decrease the transport. Next to this, the mucus layer leads to an increased thickness in the Caco-2+HT29MTX cell layer compared to the Caco-2 cell layer. The thickness of mucus in a cell layer containing was approximately 3-5  $\mu$ m [101]. An increased path length of the layer could lead to the observed decrease in permeability in the Caco-2+HT29MTX cell layer, compared to the Caco-2 layer.

Another possibility for the decreased permeability in the Caco-2+HT29MTX model compared to the Caco-2 model could be the difference in absorption of substances by enterocytes and goblet cells. Enterocytes and M-cells are mainly responsible for transcellular transport [33], while the main function of goblet cells is to produce mucus [31]. Due to a lower amount of enterocytes in the co-culture model compared to the Caco-2 model, the permeability might be reduced.

Figure 4.16 shows the relative amount of lysozyme and  $\alpha$ -Syn A53T fibrils that were taken up by the cells. This was calculated by subtracting the amount of fibrils permeated and remaining in the apical compartment from the initial concentration of amyloid fibrils. ‘Uptake’ includes all amyloid fibrils that are within the cell layer, but it does not necessarily mean that the fibrils are within the cells. It is possible that the fibrils bind to the cell membrane or present in the cell layer. There seems to be a higher uptake of  $\alpha$ -Syn A53T fibrils compared to lysozyme fibrils. The uptake in the Caco-2+HT29MTX model was lower than in the Caco-2 cell layer, which can be due to the extra barrier that mucus is forming, though further repeats are needed to confirm these results. Internalization was further analyzed in Section 4.2.7, where the cell layers are analyzed using confocal laser scanning microscopy.

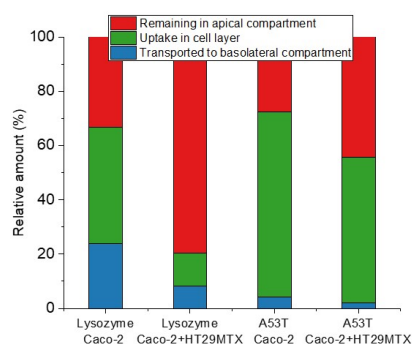


Figure 4.16: The bar graph shows the amount of lysozyme and  $\alpha$ -Syn A53T that permeated the cell model, taken up by the cells and which amount remained in the apical compartment.

#### 4.2.5 Identification of amyloid fibrils and monomers in the basolateral samples

From the bulk fluorescence spectroscopy measurements, it seemed that lysozyme and  $\alpha$ -Syn A53T fibrils and monomers cross the cell models. From these measurements, however, it remained unknown whether the emission signal originates from fibrils, monomers, free dye, or other structures such as oligomers. As discussed, monomers could be present in the sample because of incomplete removal during purification or due to fibril disassembly upon exposure to cells. The next step in this research was to differentiate between fibrils and monomers in the basolateral samples, because, mostly, monomers do not cause aggregation of disease-related amyloid forming proteins, such as  $\alpha$ -Syn wt monomers. This indicates that fibrils are potentially a higher risk for neurodegenerative disease than monomers. However, for lysozyme this is not the case, as the aggregation mechanism is based on the positive charge of lysozyme, so it is hypothesized that lysozyme monomers could also induce aggregation of disease-related proteins, such as  $\alpha$ -Syn wt monomers. Differentiation between fibrils and monomers was done by the use of Real-Time Quaking-induced Conversion (RT-QuIC). RT-QuIC can also give an indication about the ability to induce aggregation of  $\alpha$ -Syn wt monomers by lysozyme and  $\alpha$ -Syn A53T fibrils and monomers *in vivo*.

In the RT-QuIC experiments, lysozyme and  $\alpha$ -Syn A53T fibrils or monomers can act as template seeds to reduce the aggregation lag-time of  $\alpha$ -Syn wt-monomers. For lysozyme, a cross-seeding experiment was performed based on surface-mediated aggregation of  $\alpha$ -Syn wt monomers by lysozyme fibrils.  $\alpha$ -Syn wt monomers can bind to the surface of lysozyme fibrils. This mechanism is based on the charge difference between lysozyme and  $\alpha$ -Syn wt monomers. This mechanism was used as homogeneous seeding of lysozyme was not possible, as the temperature of the plate reader could not be set to the optimal lysozyme aggregation temperature, which is 70°C. Next to this, the pH should be 2, which is not the case for the basolateral samples. For  $\alpha$ -Syn A53T, the mechanism involves seed-elongation. Here,  $\alpha$ -Syn wt monomers can only bind to the ends of  $\alpha$ -Syn A53T fibrils. In RT-QuIC, the reduction of aggregation time of  $\alpha$ -Syn wt monomers was used as a measure for fibrils and monomer concentration.

Different concentrations of salt (NaCl) in the buffer were tested: a low salt concentration (LS) with 10 mM NaCl and high salt concentration buffer (HS) containing 150 mM NaCl. The concentration of salt in the buffer has different effects on the lag-time in the RT-QuIC experiments for the different mechanisms. For seed-elongation RT-QuIC, a HS buffer is expected to increase the difference in lag-time between fibrils and monomers. The reason for this is that in a HS buffer, the charge of monomers is screened, so binding of  $\alpha$ -Syn wt monomers to lysozyme is no longer possible. Fibrils have a higher charge density, so here, the net charge of fibrils is not much affected in a salt solution. The salt concentration in seed-elongation can enhance the RT-QuIC experiment [82].

The read-out of RT-QuIC-experiments was Thioflavin-T (ThT) emission. ThT binds to cross- $\beta$ -sheets in fibrillar structures, so ThT-intensity shows the degree of aggregation of  $\alpha$ -Syn wt-monomers. For all of the ThT graphs in the RT-QuIC experiments, the lag-time was defined as the time at which the graph reaches a threshold of the mean + 5  $\times$  standard deviation of the first hour. An unseeded sample, as well as the other samples, contained 22  $\mu$ M  $\alpha$ -Syn wt-monomers, so eventually,  $\alpha$ -Syn in the unseeded sample will also show an increase of ThT signal. The reduction of aggregation in the samples was normalized to the lag-time of the unseeded samples and all samples were tested in quadruplicate.

First, typical ThT curves and some anomalies will be discussed. The calibration curves will be shown to determine the exact relation between reduction in lag-time and fibril concentration. Furthermore, the lag-time of the basolateral compartments of the cell models will be compared to the calibration. Figure 4.17 shows some ThT-graphs of the RT-QuIC experiments. Figure 4.17a shows the aggregation of  $\alpha$ -Syn wt monomers by lysozyme fibrils in a LS buffer. The graphs are representative for the quadruplicates and show how most of the RT-QuIC data looks like. There are some exceptions, which will be discussed next.

Figure 4.17b shows the ThT graphs for  $\alpha$ -Syn A53T fibrils in a HS buffer. In the first 15 minutes, a very low intensity in some wells was observed in this experiment (around 20 A.U. instead of 300 A.U.). There was probably a problem with the placement of the wells plate in the measuring device, so the experiment was restarted. Because of this, the data points of the first 15 minutes of the experiment could not be used. The ThT intensity of the three highest concentrations was already increasing at  $t=0$ . The actual lag-time could not be determined, so the lag-time was set to 0.

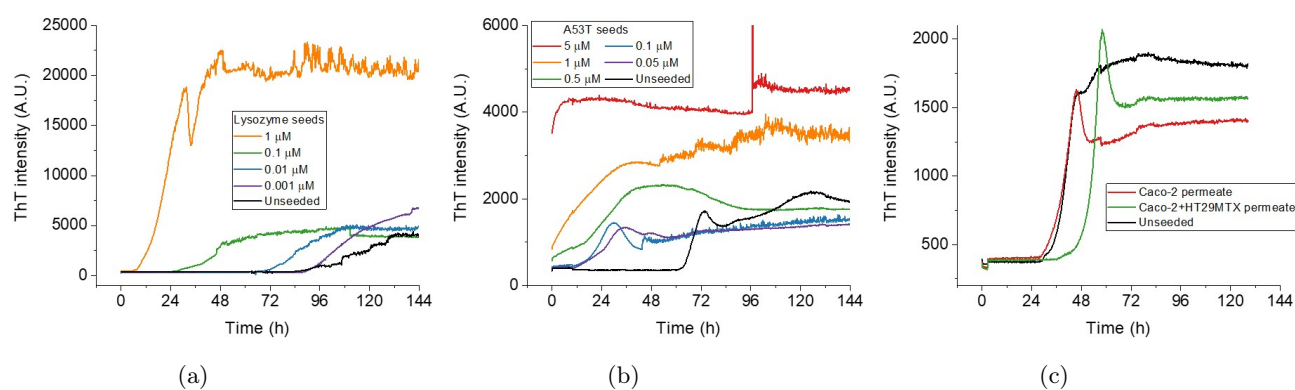


Figure 4.17: ThT intensity graphs in RT-QuIC experiments. (a) Lysozyme fibrils in a buffer with low salt concentration. (b)  $\alpha$ -Syn A53T fibrils in a buffer with high salt concentration. (c) Samples of the basolateral compartment of Caco-2 and Caco-2+HT29MTX after exposure to  $\alpha$ -Syn A53T.

Figure 4.17c shows ThT graphs of the samples of the basolateral compartment of the cell models after exposure to  $\alpha$ -Syn A53T fibrils after 72h. In the first hour, there was a jump in the intensity, which occurred more often. This was probably a defect of the device, as it happened in all wells in the wells plate. When this happened in the first hour, the threshold could not be calculated from the first 6 data points. Therefore, the threshold was determined from 6 other data points, where there was no ‘jump’. The lag-time of the basolateral sample of the Caco-2+HT29MTX model was longer than the lag-time of the unseeded sample. This was also observed in the replicates of the sample. An explanation for this will be given in the paragraph about RT-QuIC with  $\alpha$ -Syn A53T.

Next, the calibration and samples of lysozyme and  $\alpha$ -Syn A53T in RT-QuIC will be discussed. Figures 4.18 and 4.19 show the lag-times of all RT-QuIC experiments normalized to unseeded samples. Normalization was performed to reduce the batch-to-batch variance that is known to happen in RT-QuIC experiments [79, 104]. The lag-time in LS buffer in the unseeded sample varied from 26 hours to 89 hours, so this variation confirms the observations in literature.

## Lysozyme

In surface-mediated RT-QuIC with lysozyme, it is hypothesized that lysozyme fibrils bind to the negatively charged C-terminal of  $\alpha$ -Syn. The aggregation prone NAC-region is now exposed and available to bind with the C-terminal of other  $\alpha$ -Syn monomers. The structure is left in a more aggregation-prone conformation on the lysozyme fibril surface, so monomers will assemble on the surface and form  $\alpha$ -Syn fibrils [11]. As lysozyme monomers also have a net positive charge, it is hypothesized that lysozyme monomers may also cause aggregation of  $\alpha$ -Syn wt monomers, which is the reason that a control group with monomers was added. HS buffer was used to reduce the aggregation caused by lysozyme monomers. By doing this, the charge of monomers was screened, so the binding of  $\alpha$ -Syn wt monomers to lysozyme was no longer possible. Fibrils have a higher charge density, so here, the net charge of fibrils is not as much affected in a salt solution as the monomers.

Figure 4.18a shows the normalized lag-time of lysozyme fibrils and monomers in a LS buffer and Figure 4.18b in a HS buffer. In a LS buffer, the lag-time was decreased with increasing lysozyme concentration. However, there was no difference between the fibrils and monomers. This indicates that monomers can cause aggregation of  $\alpha$ -Syn wt monomers, which corresponds to the hypothesis previously described. This observation is important, as it shows that lysozyme monomers can also be a potential risk for neurodegenerative diseases by causing aggregation of disease-related amyloid fibrils. However, at physiological conditions, the salt concentration is approximately 150 mM, so it may be more relevant to look at the lag-time in a HS buffer in Figure 4.18a, where only a high concentration of lysozyme monomers causes aggregation of  $\alpha$ -Syn wt monomers. This needs to be further examined, as it was not tested in physiological conditions.

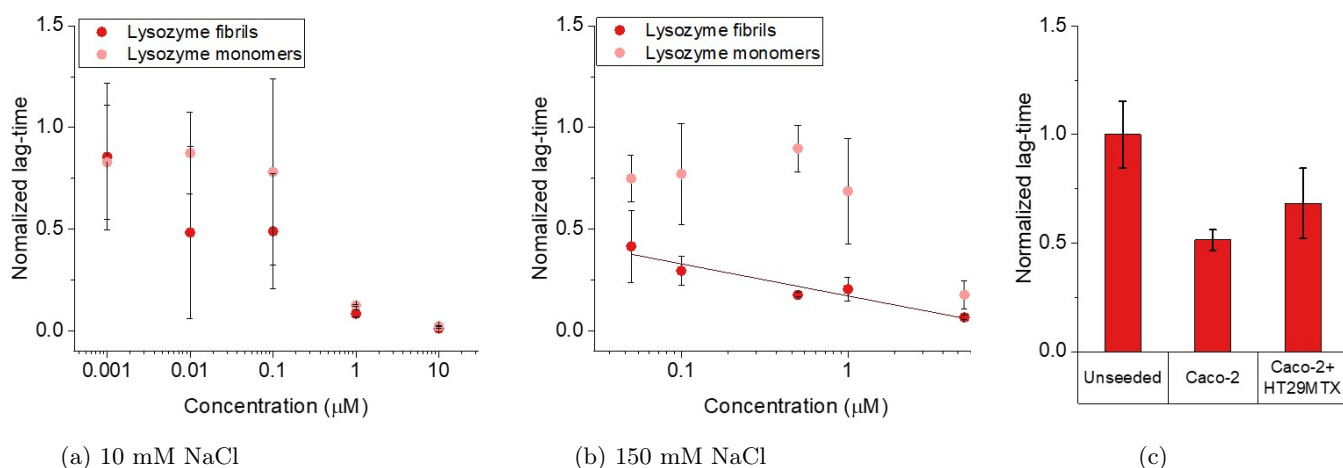


Figure 4.18: Normalized lag-time in RT-QuIC experiments for lysozyme and  $\alpha$ -Syn wt monomers, where lysozyme acts as a seed. (a) was performed in a buffer with low salt concentration and (b) in a buffer with high salt concentration.  $R^2$  for the linear fit in (a) is 0.92. (c) Normalized lag-time of the samples of the basolateral compartment lysozyme fibril treatment. All samples contained 22  $\mu$ M  $\alpha$ -Syn wt monomers. The error bars show the standard deviation of 4 replicates.

In a HS buffer, the concentration range of lysozyme was changed to 0.05 - 5  $\mu\text{M}$  instead of 0.001 - 10  $\mu\text{M}$ . The lower concentration of lysozyme fibrils and monomers was removed, as the method apparently was less precise for this concentration. 10  $\mu\text{M}$  was removed, as the initial concentration of lysozyme fibrils was 2.5  $\mu\text{M}$ . The concentration in the basolateral compartment will not exceed this. Figure 4.18b shows that in a HS buffer, the lag-time was also decreasing with increasing lysozyme concentration. Here, the lag-time with lysozyme fibrils was decreased more than with lysozyme monomers. This indicates that it is possible to differentiate between amyloid fibrils and monomers in a HS buffer, even though there was a small overlap in lag-time between the lowest concentrations. This means that it may be difficult to differentiate between fibrils and monomers for samples with a normalized lag-time higher than 0.5, as the sample could contain monomers or a very low concentration of fibrils. For the fibrils, a linear fit was made between the normalized lag-time and the log of the concentration.  $R^2$  of the linear fit is 0.92.

The normalized lag-time of aggregation of  $\alpha\text{-Syn wt}$  monomers added to the basolateral compartment of Caco-2 and Caco-2+HT29MTX were measured and depicted in Figure 4.18c. These samples were measured in HS buffer, so it can be compared to Figure 4.18b. The normalized lag-time for the Caco-2 sample was  $0.51 \pm 0.05$  and for the co-culture  $0.69 \pm 0.16$ . Figure 4.18b shows that normalized lag-times of 0.51 and 0.69 are within the low concentration-fibrils range, but also in the monomeric range, as there was an overlap between the fibrils and the monomers. If the sample would only contain fibrils, the concentration of fibrils can be extracted from the linear fit. If this would be the case, the concentration of fibrils would be in the low nanomolar range. From the bulk fluorescence spectroscopy, it was known that the concentration in the basolateral compartment was approximately a few hundreds micromolar after 72 hours of treatment. As discussed, the bulk fluorescence spectroscopy measurements could give an incorrect concentration of amyloid fibrils and monomers, as the concentration could be inflated by the presence of free dye. However, it is assumed that the difference between hundreds micromolar and a few nanomolar cannot be explained by solely the presence of free dye. This indicates that this sample does not solely contain fibrils. However, from this data it is not possible to conclude that the sample does not contain fibrils at all, so it is assumed that the samples might contain a mixture of fibrils and monomers. The sample may also contain oligomers, but this was probably a small fraction, as oligomers are thermodynamically meta-stable. The exact ratio of the different conformations cannot be extracted from the RT-QuIC data.

### **$\alpha\text{-Syn A53T}$**

The mechanism for the RT-QuIC experiment for  $\alpha\text{-Syn A53T}$  was seed-elongation by addition of  $\alpha\text{-Syn wt}$  monomers. This means that  $\alpha\text{-Syn wt}$  monomers can only bind to the extremities of  $\alpha\text{-Syn A53T}$  fibrils and not to  $\alpha\text{-Syn A53T}$  monomers. However, the salt concentration was tested, as it can enhance the RT-QuIC reaction [82], meaning NaCl could speed up the process. First, the RT-QuIC experiment was performed in a HS buffer. It was already discussed that for the highest concentrations of  $\alpha\text{-Syn A53T}$  fibrils in a HS buffer, the lag-time was set to 0. This is depicted in Figure 4.19b. Because the lag-time was too short, the next experiment was performed in a LS buffer. Next to this, the concentration range was changed to lower concentrations.

Figure 4.19a shows that in a LS buffer, there was a linear relationship between the normalized lag-time and log of the A53T fibril and monomer concentrations.  $R^2$  of the linear fit is 0.94. Besides, there was a clear difference between lag-time of amyloid fibrils and monomers. There was, however, an overlap in lag-time between the two lowest concentrations of fibrils and the highest concentration of monomers. When comparing the two different mechanisms used, it is clear that with seed-elongation, lower concentrations of fibrils can be measured than with surface-mediated RT-QuIC. This may be due to that in surface-mediated RT-QuIC not all  $\alpha$ -Syn wt monomers that bind to lysozyme fibrils form a nucleus for  $\alpha$ -Syn wt fibrils. More lysozyme fibrils may be necessary to induce the aggregation of  $\alpha$ -Syn wt fibrils.

Figure 4.19c shows the lag-time of the samples of the basolateral compartment of Caco-2 and Caco-2+HT29MTX. This experiment was performed in a LS buffer, so the values can be compared to Figure 4.19a. The basolateral sample of Caco-2 has a lag-time equal to that of the unseeded sample, indicating that there are no  $\alpha$ -Syn A53T fibrils present in the sample. The lag-time of the Caco-2+HT29MTX was decreased compared to the unseeded sample. It is likely that the basolateral sample of the co-culture also did not contain amyloid fibrils. A possible explanation for the decrease in lag-time in the basolateral sample of Caco-2+HT29MTX is explained in the next paragraph.

The permeability studies were performed in culture medium containing 20% Fetal Bovine Serum (FBS). FBS contains several proteins, which can influence the aggregation process in the RT-QuIC experiments. The calibration of amyloid fibrils and monomers was therefore done in cell culture medium. However, the basolateral samples could contain other proteins, secreted by the cells, that can enhance or slow down the aggregation. In surface-mediated RT-QuIC, a change in lag-time in the presence of these proteins could be caused by local charge differences by binding of proteins secreted by the cells to lysozyme fibrils. Local charge differences could alter the process and increase or decrease the lag-time. Another possibility is that the proteins secreted by the cells of themselves induce aggregation of  $\alpha$ -Syn wt monomers. For the seed-elongation mechanism, it could be that proteins secreted by cells bind to the ends of  $\alpha$ -Syn A53T

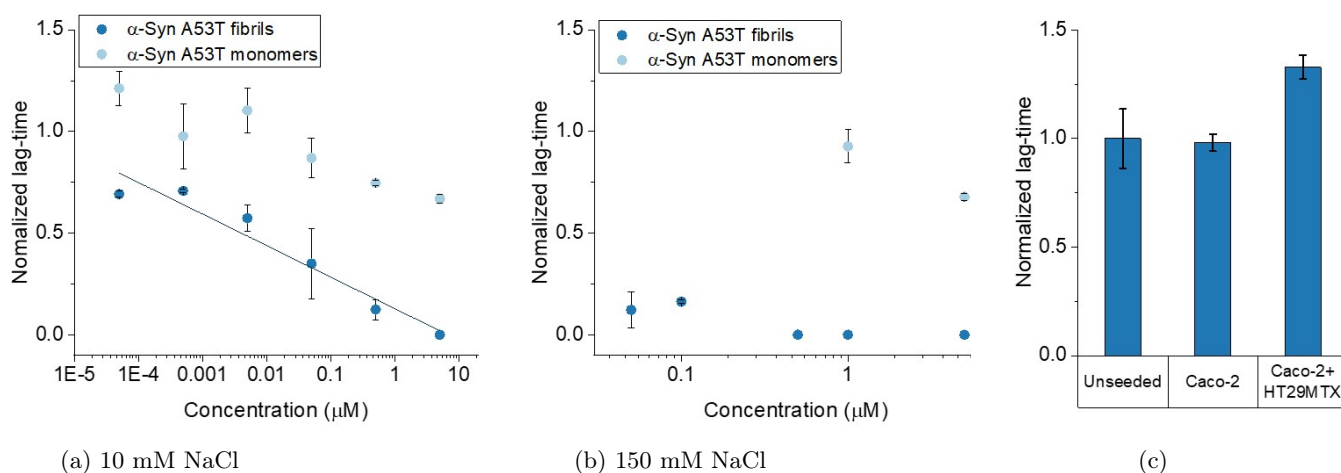


Figure 4.19: Normalized lag-time in RT-QuIC experiments for  $\alpha$ -Syn A53T and  $\alpha$ -Syn wt monomers, where  $\alpha$ -Syn A53T acts as a seed. (a) was performed in a buffer with low salt concentration and (b) in a buffer with high salt concentration.  $R^2$  for the linear fit in (a) is 0.94. (c) Normalized lag-time of the samples of the basolateral compartment  $\alpha$ -Syn A53T fibril treatment. All samples contained 22  $\mu$ M  $\alpha$ -Syn wt monomers. The error bars show the standard deviation of 4 replicates.

fibrils. By doing this,  $\alpha$ -Syn wt monomers cannot bind to these ends, so the aggregation is inhibited. The changes in lag-time by proteins secreted by cells may give an incorrect estimation of the amyloid fibril and monomer concentration in the basolateral compartment. Further research should be done to understand the change in lag-time by proteins secreted by the cells. This can be tested by performing the experiments in cell culture medium taken from cells after a few days of incubation.

To summarize, from the bulk fluorescence spectroscopy experiment it was observed that all basolateral samples contained amyloid fibrils, monomers or free dye. With RT-QuIC, it was attempted to differentiate between fibrils and monomers was made. The basolateral samples of the Caco-2 model and the Caco-2+HT29MTX for both types of amyloid fibrils did not contain a high concentration of amyloid fibrils, as the lag-time of  $\alpha$ -Syn wt monomers was not much reduced. The exact ratio of the different conformations cannot be extracted from the RT-QuIC data. Lysozyme monomers appeared to cause aggregation of  $\alpha$ -Syn wt monomers, so this could also be a potential risk for aggregation of disease relation amyloids. Further testing should be done in the presence of proteins secreted by the cells. After this, aggregation experiments should be performed in even more physiological conditions, such as cell lysate or blood serum.

#### 4.2.6 Identification of free dye and lysozyme and $\alpha$ -Syn A53T species in the basolateral samples

From the bulk fluorescence spectroscopy measurements and the RT-QuIC data, it seemed that lysozyme and  $\alpha$ -Syn A53T fibrils and monomers cross the cell models. However, the apparent permeability, includes all labelled structures in the basolateral compartment, so it could include a mixture of fibrils, monomers, oligomers or free dye. As mentioned, free dye could be present in the samples due to incomplete removal during purification, which could increase the emission intensity, while there were no fibrils or monomers present. For this reason, the next step in this research was to exploit Fluorescence Correlation Spectroscopy (FCS) to test if free dye was present in the sample. Next to this, with FCS it was attempted to get an idea about the size of the particles to distinguish between larger structures, such as fibrils or oligomers and smaller monomers.

FCS offers insights into the diffusion behaviour of fluorescently labelled molecules or particles. Fluorescently labelled molecules diffuse through a detection volume due to Brownian motion. Fluctuations in emission intensity reflect the number of molecules within the detection volume. The changes in the intensity were quantified by auto-correlating the signal. By fitting the auto-correlated signal, the average number of particles and the average diffusion time were extracted. Eventually, the concentration and diffusion coefficient can be determined [105]. The hydrodynamic diameter,  $D_h$ , of the particles can be determined with the Einstein-Stokes equation:

$$D_h = \frac{K_B T}{3\pi\eta D} [72] \quad (4.2)$$

In which  $D$  is the diffusion coefficient,  $K_B$  the Boltzmann's constant,  $T$  the temperature and  $\eta$  the dynamic viscosity [72].

In FCS, the y-axis of the auto-correlation curves,  $G(0)$ , equals the inverse of the number of particles in the focal volume. The samples were diluted to obtain a  $G(0)$  value between 0.1 and 1. Measuring a particle with a known diffusion coefficient was done to calibrate the focal volume and  $\kappa$ . In FCS,  $\kappa$  is the ratio of the axial length of the focal volume to the lateral length of the focal volume [106]. In this research, AF647 in MiliQ water was used for the calibration measurements. The diffusion coefficient of AF647 is  $330 \mu\text{m}^2/\text{s}$  [107]. The measured focal volume was around 1.7 fl and  $\kappa$  was around 6, which are both in the expected range, compared to literature [39]. This was found using a triplet-state fit. This type of fit was used as electrons of the fluorophore can be excited to the triplet state and emit photons at a somewhat same time-scale as the diffusion time. By fitting the autocorrelation graph to a triplet state fit, this effect can be taken into account. The fits which will be discussed next are all triplet fits. Fits were considered good when  $\chi^2$  was approximately 1 and the residual plot was randomly dispersed.

The samples of the basolateral compartment were diluted cell culture medium containing FBS, which has a higher viscosity than MiliQ water. Therefore, free dye was also measured in cell culture medium. The diffusion coefficient of AF647 in cell culture medium was found to be  $342 \pm 36 \mu\text{m}^2/\text{s}$ . To find this diffusion coefficient of AF647 in culture medium, a second order fit was necessary. A second population of approximately  $70 \mu\text{m}^2/\text{s}$  was found. This population could be proteins originating from serum in the

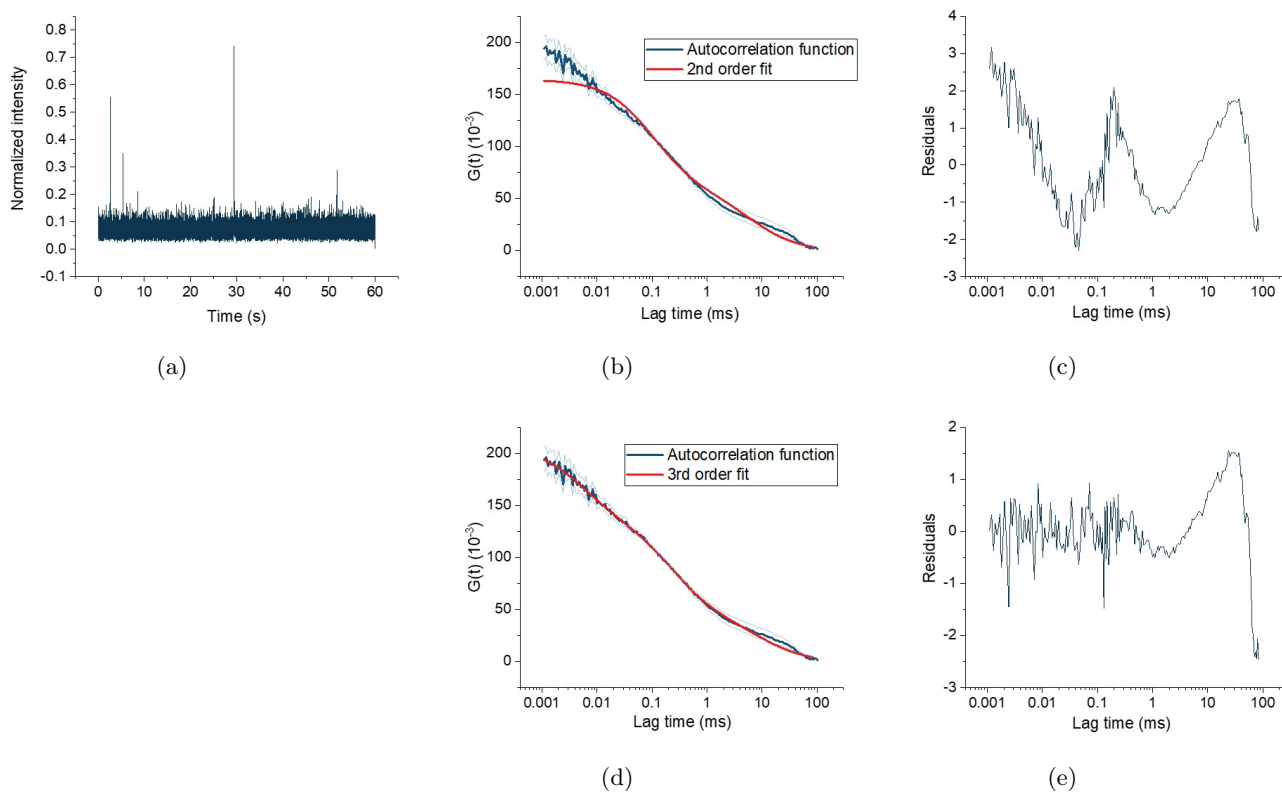


Figure 4.20: FCS data of the sample of the basolateral compartment of Caco-2 cells after exposure to  $\alpha$ -Syn A53T. (a) Intensity trace. (b) Triplet 2nd order fit and (c) residual plot of (b). (d) Triplet 3rd order fit and (e) residual plot of (d).

culture medium, stained by the free dye in the solution. This population was 28.0% of the total number of particles in the solution. As the diffusion coefficient of free dye in MiliQ is within the standard deviation of free dye in culture medium, it was assumed that there was no difference between the diffusion coefficient of free dye in MiliQ and free dye in culture medium, so it was assumed that the viscosity was equal.

The diffusion coefficient of lysozyme monomers in MiliQ was found to be  $122 \pm 15 \mu\text{m}^2/\text{s}$ . This was found with a first order fit. The diffusion coefficient corresponds to the radius of lysozyme monomers, which is approximately 1.6 nm. No population with a diffusion coefficient of approximately  $330 \mu\text{m}^2/\text{s}$  was found, which indicates that there was no free dye in this solution, or at least in a very low concentration. With fitting of the autocorrelation graph of lysozyme monomers in culture medium, there was no population found with a diffusion coefficient of approximately  $120 \mu\text{m}^2/\text{s}$  with a first order fit. An attempt was made to plot the fit with a fixed diffusion-time,  $\tau$ . This was fixed at 0.27 ms, which corresponds to a diffusion coefficient of  $120 \mu\text{m}^2/\text{s}$ . When doing this with a first order fit, no good fit could be made. A second order fit was tried and a good fit could be made. There was a second population with a diffusion coefficient of approximately  $40 \mu\text{m}^2/\text{s}$ . This was 28% of the total numbers of particles in the solution. This second population could be lysozyme di- or oligomers. Another possibility was that there were other proteins present in the solution, but these were originally unstained. That there was a second population visible in this sample may indicate that there was free dye in the monomer solution which stains the proteins originating from the serum in the culture medium. However, this option was also not very likely as no population of free dye was found in the FCS measurement of lysozyme

monomers in MiliQ. The final option could be that proteins from the culture medium bind to lysozyme monomers, causing a decrease in diffusion coefficient, as the monomers become larger. This may lead to the conclusion that FCS was not suitable to use for measurements in cell culture medium. It was not found in literature that FCS measurements were performed in cell culture medium. Still, the samples of the basolateral compartments were measured with FCS to try to get an idea about the size of the particles to distinguish between larger structures, such as fibrils or oligomers and smaller monomers.

An example of a sample of the basolateral compartment of Caco-2 cells with exposure to  $\alpha$ -Syn A53T cells will be discussed. The concentration of fluorescence molecules was suitable for FCS, because  $G(0)$  was between 0.1 and 1. An intensity trace of the sample is shown in Figure 4.20a. The distinct peaks that can be seen could be small structures of  $\alpha$ -Syn A53T, such as fibrils or oligomers, diffusing in and out of the detection volume. Figure 4.20b shows a triplet second order fit with  $\chi^2$  of 0.53. Figure 4.20d shows the triplet third order fit with  $\chi^2$  of 0.36. Figure 4.20c and 4.20e also show that the residual plots were not randomly dispersed. This indicates that it was not possible to obtain a good fit for these intensity traces.

Figure 4.21a shows the intensity trace of the same measurement, but here only the time point from 10 to 30 seconds from Figure 4.20a were used. These time points were chosen to exclude the distinct peaks from Figure 4.20a. For this example, it was possible to make a good second order fit, see Figure 4.21b.  $\chi^2$  of 1.088 and the residual plot looks randomly dispersed, see Figure 4.21c. The populations that were found had a diffusion coefficient of  $246 \pm 35 \mu\text{m}^2/\text{s}$  and  $32 \pm 12 \mu\text{m}^2/\text{s}$ , which corresponds to particle radius of respectively 0.9 nm and 6.7 nm. The smaller-sized population does not correspond to monomers or free dye. This population could be monomers, which were (partly) degraded by the cells or enzymes secreted by the cells. The larger population could be fibrils or oligomers in the sample. Furthermore, it could be that proteins from the culture medium and proteins secreted by the cells attached to the stained  $\alpha$ -Syn A53T monomers. Binding would be unspecific, but the same types of proteins were present throughout the sample, so eventually, there would be one specific range of particle sizes.

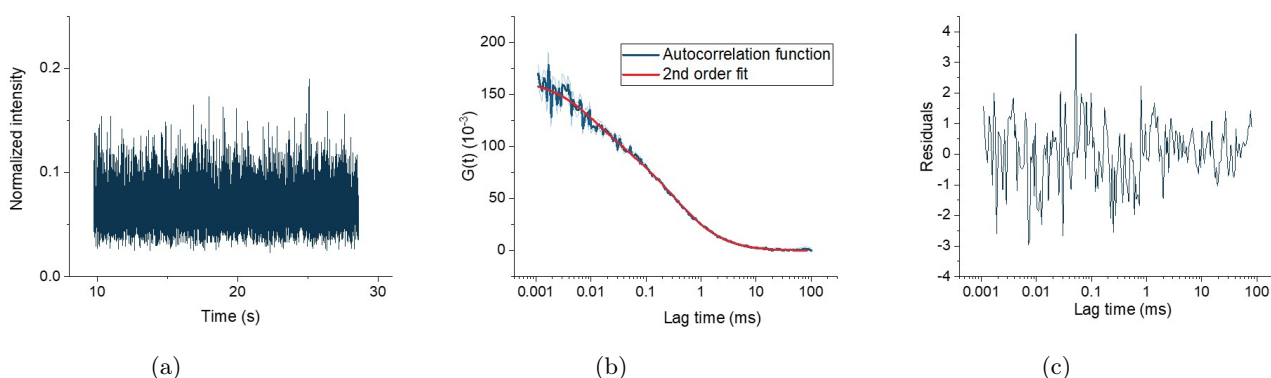


Figure 4.21: FCS data from a part of the data from sample of the basolateral compartment of Caco-2 cells after exposure to  $\alpha$ -Syn A53T. (a) Intensity trace. (b) Triplet 2nd order fit and (c) residual plot of (b).

To summarize, FCS was performed to examine different sized lysozyme and  $\alpha$ -Syn structures, such as monomers or oligomers, and free dye in the basolateral samples. This was done, as it was not clear from the bulk fluorescence spectroscopy measurements if the emission signal originated from lysozyme and  $\alpha$ -Syn A53T fibrils, monomers or free dye. From the FCS data, it was assumed a very low concentration of free dye was present in the samples, as there was no population with the diffusion coefficient of free dye found in the sample of  $\alpha$ -Syn A53T monomers diluted in MilliQ. It remained unclear whether the large structures were fibrils, oligomers or proteins from the cell culture medium or secreted by the cells attached to labelled monomers.

#### 4.2.7 Internalization of amyloid fibrils by Caco-2 and HT29MTX cells

The Caco-2 and Caco-2+HT29 cell models treated with 2.5  $\mu$ M lysozyme and  $\alpha$ -Syn A53T fibrils for 72 hours were imaged with confocal microscopy to examine the location of the amyloid fibrils within the cell layer. This may give an explanation for the difference in the ability of permeation of lysozyme and  $\alpha$ -Syn A53T, as the apparent permeability for lysozyme appeared to be higher than  $\alpha$ -Syn A53T. First, the stainings are explained. Next, the position of amyloid fibrils was determined in the Z-plane of the cell layers. Finally, different internalization mechanisms of amyloid fibrils found in literature are discussed and compared to the observations of this research.

AF488-phalloidin was used to stain F-actin. Actin can be present in the cell as monomers called G-actin (globular) or as part of a polymeric microfilament, called F-actin (filamentous) [108]. F-actin plays a crucial role in many functions in the cell, such as cell motility, division and signalling. Actin is the most abundant intracellular protein in a cell. It is concentrated into bundles within the cell. The richest area of F-actin filaments lies in the cortex, a small zone just beneath the plasma membrane. F-actin filaments are a part of a network continuing into the cell interior. By staining F-actin, the structure of a cell can be visualized. Phalloidin conjugated to a dye is often used for staining F-actin. Labelled phalloidin a good stain for visualizing the cytoskeleton of the cell and structural changes in the cytoskeleton in response to exposure to amyloid fibrils [109].

To visualize the cell nucleus, DAPI, dilactate (4',6-diamidino-2-phenylindole) staining was used. DAPI binds to adenine–thymine-rich regions in DNA. Staining the nucleus, can give a qualitative indication about the state of DNA and apoptosis of the cell [110].

Figure 4.22 shows confocal images of the Caco-2 and Caco-2+HT29MTX cell models with lysozyme and  $\alpha$ -Syn A53T. The images represent the entire cell layers well. Green in the images is F-actin, blue is the cell nucleus and red either lysozyme or  $\alpha$ -Syn A53T fibrils. 10 slices, or 10  $\mu$ m, were used for the orthogonal views. The images in Figure 4.22 show the X-Y plane of the fifth Z-slice. Figure 4.22c and 4.22e contain more amyloid fibrils than the images of Figure 4.22g and 4.22i. The white arrows in the orthogonal views in Figure 4.22g and 4.22i show that  $\alpha$ -Syn A53T remained on top of the cells and not inside the cells. The  $\alpha$ -Syn A53T fibrils that can be detected in the images probably interact with the cell membrane, otherwise the fibrils would have been washed away before fixation. This indicates that the cells have better uptake capabilities for lysozyme fibrils compared to  $\alpha$ -Syn A53T fibrils.

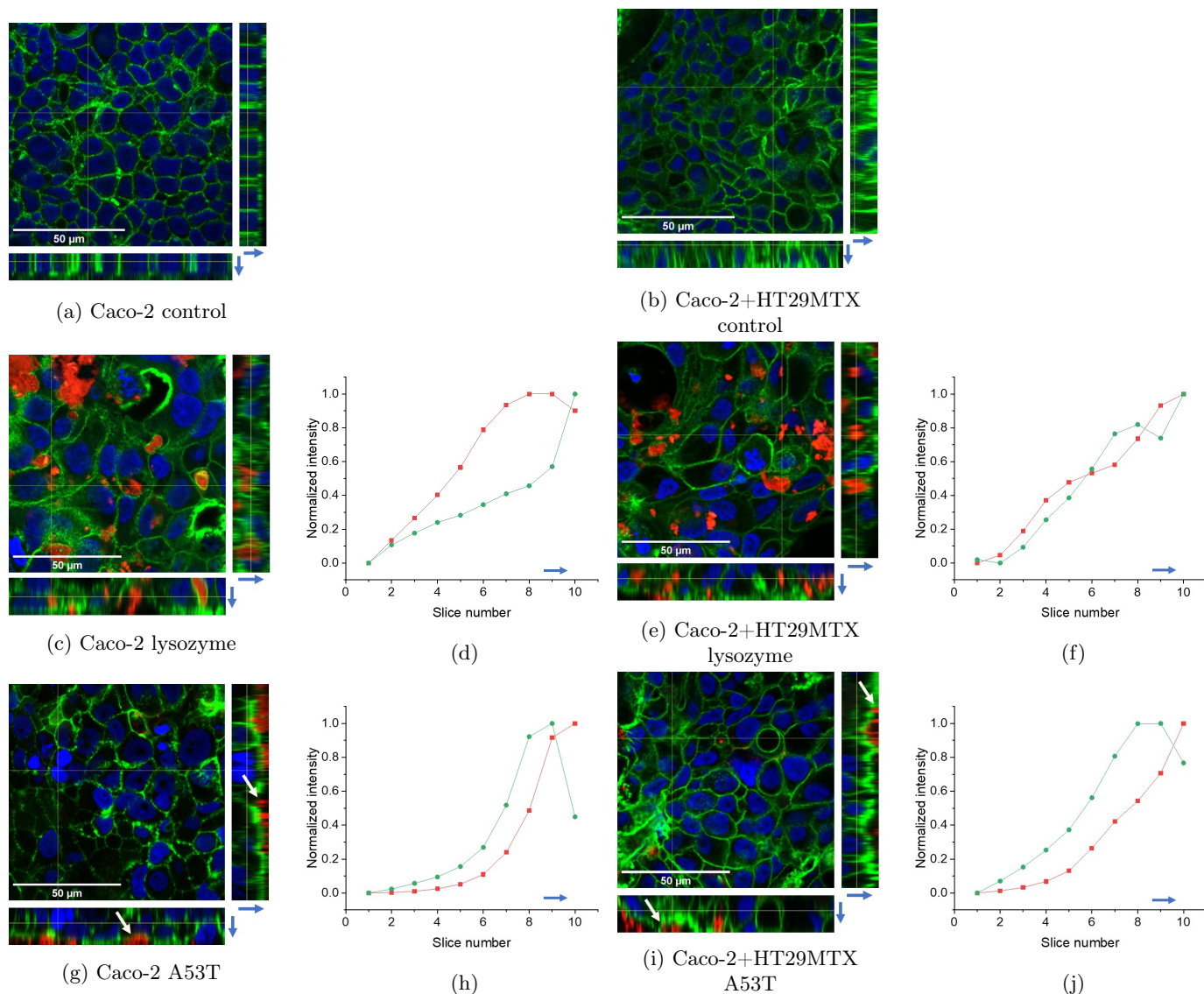


Figure 4.22: Images with orthogonal views and intensity profiles of cell models treated with lysozyme and  $\alpha$ -Syn A53T. (a) Caco-2 control, (b) Caco-2+HT29MTX control. Cell layers treated with lysozyme in (c) and (g) and  $\alpha$ -Syn A53T in (e) and (i) with corresponding intensity profile in (d), (f), (h) and (j) for AF488-phalloidin (green) and amyloid fibrils (red). Blue arrows point towards the top of the cell layer.

Intensity profiles were made to show where the fibrils were positioned in the Z-axis of the cell layer. The graphs in Figure 4.22 show the mean intensity per slice of the amyloid fibrils and F-actin. Slice 10 was on top of the cells, and slice 0 was 10  $\mu$ m into the cell layer. For all of the conditions, F-actin and amyloid fibril intensity increases towards the top of the cell layer. For F-actin, this was because the AF488-phalloidin staining was pipetted on top of the cells. AF488-phalloidin needs to penetrate the cell layer, so there was more AF488-phalloidin available at the top of the cells than towards the bottom. Next to this, the cortex, which contains a large amount of F-actin, lies just beneath the plasma membrane, so the top shows a high intensity of AF488-phalloidin signal [109].

The amyloid fibril intensity increases towards to top because most of the larger amyloid fibril structures remain on top of the cells. There is a difference in the intensity profiles between lysozyme and  $\alpha$ -Syn A53T. The intensity of AF488-phalloidin reaches a maximum at the top membrane of the cells. It can be seen in Figure 4.22h and 4.22j that the top of the cells was around slice 9. The intensity of

$\alpha$ -Syn A53T was still increasing beyond the outer layer of the cells, meaning the amyloid fibrils were positioned on top of the cells. In Figure 4.22h and 4.22f the peak of the intensity of lysozyme was still within the cells.

These results indicate that  $\alpha$ -Syn A53T fibrils remain on the top of the cells, whereas lysozyme fibrils seem to be internalized by the cells. A possible difference in the uptake by the cells could be an explanation for the difference in apparent permeability observed in the bulk fluorescence spectroscopy and RT-QuIC experiments. In those experiments, it seemed as if lysozyme could translocate more easily than  $\alpha$ -Syn A53T, which could be an explanation for the higher apparent permeability for lysozyme, compared to  $\alpha$ -Syn A53T. In literature, multiple mechanisms are reported by which amyloid fibrils can be internalized. In the next paragraphs, a few examples of the internalization of amyloid fibrils by cells are discussed and compared to the observations in this research.

Intestinal epithelial cells have a negatively charged cell surface, similar to other types of cells [111]. The negatively charged surface, as well as proteins on the surface, provide sites of interactions for positively charged compounds. One example of a protein present on the plasma membrane of cells that can form interactions based on the charge of amyloid fibrils is heparan sulfate proteoglycan (HSPG). HSPG can act as a receptor for cell-surface endocytosis [112, 113]. Endocytosis can occur via different mechanisms, such as clathrin-mediated endocytosis [112]. In literature, it is thought to be that the uptake of  $\alpha$ -Syn in neuronal cells might be dependent on cell surface HSPG [114].

The interaction between amyloid fibrils and HSPG likely occurs by interactions between the negatively charged HSPG and positively charged amino acids of amyloid fibrils. For  $\alpha$ -Syn, the central region is slightly positively charged. These studies have shown that it is possible for different amyloid fibrils to be internalized by neuronal cells by HSPG-receptor endocytosis. HSPG is also abundant on intestinal cells [111], which indicates that this could be a possible receptor for endocytosis of amyloid fibrils by intestinal cells. Next to this, both lysozyme and  $\alpha$ -Syn A53T fibrils contain positively charged regions. From this, it is expected that it could be possible for lysozyme and  $\alpha$ -Syn A53T fibrils to be internalized in Caco-2 and HT29MTX cells. However, the exact charge of lysozyme and  $\alpha$ -Syn A53T fibrils in cell culture medium with the presence of ions is not known.

Another possible internalization pathway observed for amyloid fibrils is macropinocytosis [115, 116]. Macropinocytosis involves rearrangement of the F-actin cortex by the formation of membrane ruffles. The ruffles can fold back to the membrane to form a large vesicle that traps the substance [117], see Figure 2.2 in Chapter 2. These vesicles have a size of approximately 0.2 - 5  $\mu$ m, so this mechanism allows internalization of relatively large structures [116]. All substances in the fluid inside the vesicle are internalized, which makes the process non-specific [42]. Macropinocytosis is generally triggered by growth factors, but can also be triggered by apoptotic bodies or necrotic cells [116]. Another trigger for macropinocytosis is receptor-mediated, for instance by the use of HSPG [112, 115]. It has been found that internalization of  $\alpha$ -Synuclein is possible via macropinocytosis, and occurs in the time range of a few hours [115, 116].

To summarize, there are different mechanisms for the internalization of amyloid fibrils possible. Characteristics like size and charge are crucial properties for the uptake. Internalization occurs for a wide range of amyloid fibril sizes. Next to this, in the mechanisms discussed, a positively charged region seems to be important for the uptake. Uptake of amyloid fibrils can also be non-specific. From this, it seems as if it would be possible for lysozyme and  $\alpha$ -Syn A53T to be internalized by the cells. However, the results of the confocal microscopy images seem to contradict this. In the confocal images of this research, it was observed that  $\alpha$ -Syn A53T remained on the top of the cell layer and lysozyme was internalized. An explanation for this could be that even though both types of amyloid fibrils have positively charged sites, the net charge was different. This could in turn change the binding properties of the amyloid fibrils to membrane proteins, such as HSPG. Further research is needed to support these findings, for example to the exact charge of the amyloid fibrils in cell culture medium.

While the difference in charge may explain the difference in the internalization of  $\alpha$ -Syn A53T and lysozyme, the confocal images do not provide enough information to prove this theory. First, the confocal images of the cell layers were made after 72 hours of exposure to amyloid fibrils. It has been reported that the time span for macropinocytosis is within a few hours [115]. Because of this, it might be possible that the cell internalize and remove  $\alpha$ -Syn A53T, but that this is not visible on these confocal images. Next to this, cells that internalized  $\alpha$ -Syn A53T fibrils may have died and removed during the washing steps. Because of this, the internalization of  $\alpha$ -Syn A53T cannot be seen in the cells after 72 hours. Only the larger  $\alpha$ -Syn A53T fibrils remain on the top of the cells. These possibilities should be further analyzed, for example with time-dependence imaging and cytotoxicity testing.

#### 4.2.8 Reorganization of cytoskeleton upon uptake of lysozyme fibrils

In Chapter 2, different mechanisms by which substances can be taken up by the cells were briefly discussed. The mechanisms by which lysozyme fibrils were taken up are not extensively tested. However, it is possible to get an idea of the mechanism by looking at the F-actin network in confocal images. As mentioned, the internalization of  $\alpha$ -Syn A53T fibrils was not observed in the confocal images, so in this section only internalization of lysozyme fibrils is discussed.

Figure 4.23 shows the F-actin structure containing lysozyme fibrils. In Figures 4.23a and 4.23b there is a reorganization of the F-actin cortex visible. There is a clear increase in the intensity of AF488-phalloidin stained F-actin that was present around the fibrils, forming a cage-like structure. Two positions where this occurred are indicated with a white arrow in Figure 4.23b. Figure 4.23c shows the intensity of AF488-phalloidin and amyloid fibrils over the dashed white line in Figure 4.23a, with green being F-actin and red lysozyme fibrils. F-actin forms around the fibrils, which can also be seen in this graph. F-actin itself is not responsible for encapsulating the fibrils, but during the uptake there was a remodelling of the F-actin cortex. The cortex lays directly beneath the cell membrane and can be remodelled to form a cage-like structure around the fibrils [43]. This remodelling of the F-actin cortex upon the internalization of substances has been described before, for instance in macropinocytosis [42, 117] and clathrin-mediated endocytosis [43]. The exact mechanism of uptake was not known from the experiments in this research.

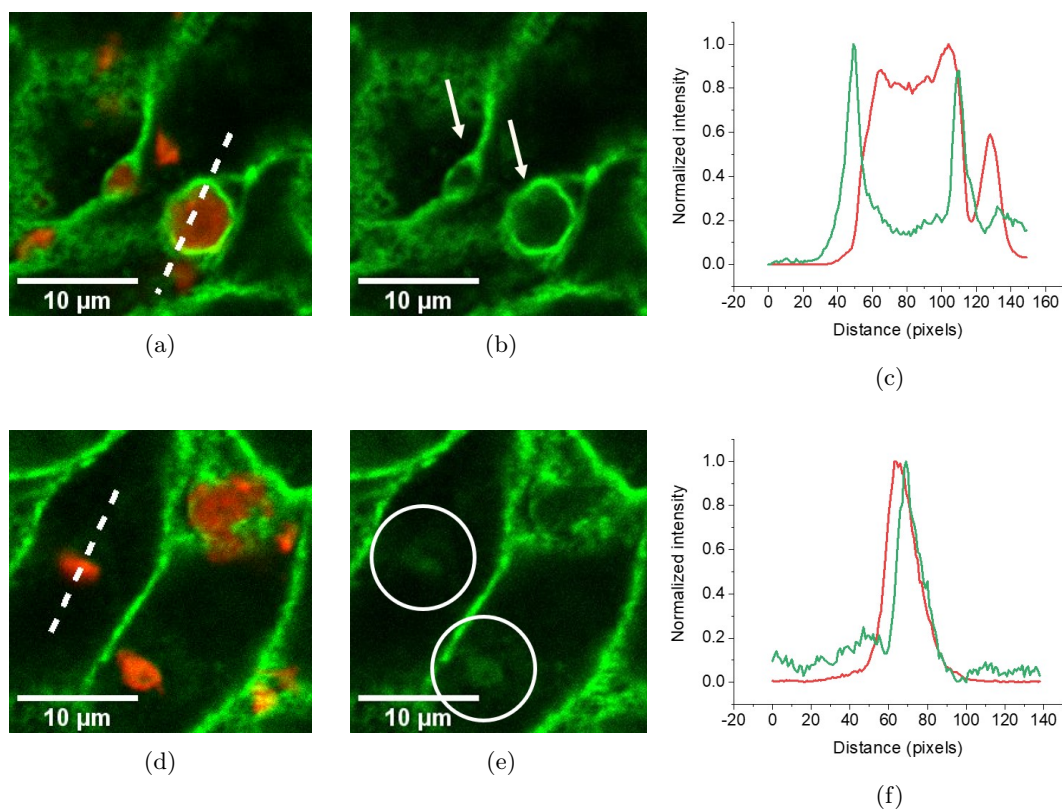


Figure 4.23: Images of Caco-2+HT29MTX cells containing lysozyme fibrils. The intensity of AF488-phalloidin and lysozyme fibrils on the dashed line in (a) and (d) is plotted in (c) and (f). The arrow in (b) shows that F-actin was reorganizing around the fibrils. The circles in (e) show the sequestration of F-actin by lysozyme fibrils.

Furthermore, in Figure 4.23d and 4.23e fibrils that were internalized by the cells are shown. The positions of these fibrils are indicated by white circles in Figure 4.23e. Figure 4.23f shows that at the position of the fibril on the dashed line there is an increase of AF488-phalloidin signal. This indicates that fibrils sequester F-actin inside the cell. A possibility is that lysozyme fibrils bind non-specifically to F-actin. It has been previously observed in literature that monomeric hen egg-white lysozyme monomers and F-actin can self-assemble because of their opposite charges [65]. This may also occur with lysozyme fibrils.

Figure 4.24 shows again the effect of F-actin reorganisation in Caco-2 cells. Here, the orthogonal views are also shown to show the cage-like structure in all direction. In Figure 4.24a it is clear that F-actin remodels in a cage-like structure around the fibril. In Figure 4.24c the cage is indicated with the black arrows. The intensity profile shows that the AF488-phalloidin intensity within the cage at 60-100 pixels was somewhat higher than the background at 0-30 pixels and 130-160 pixels, so the sequestration, described in the previous paragraph and Figure 4.23f is also present in this region.

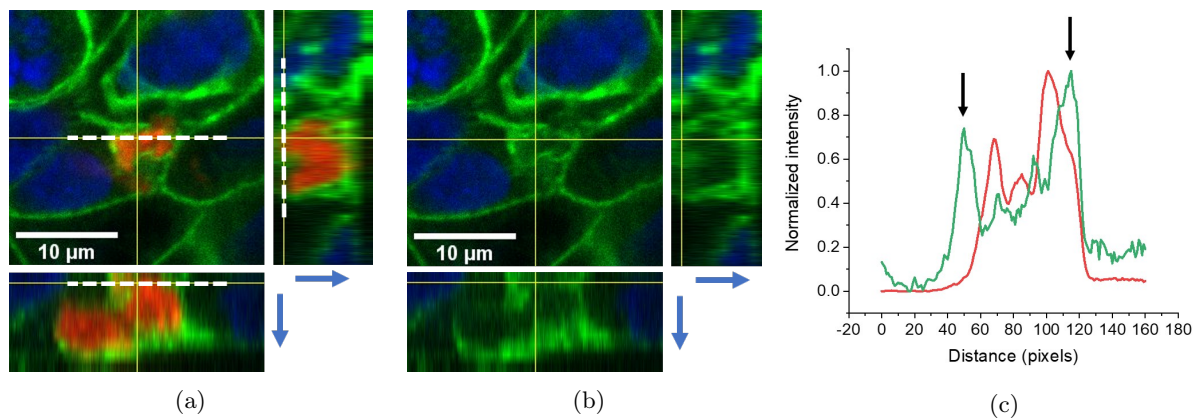


Figure 4.24: Images of Caco-2 cells containing lysozyme fibrils. (a) and (b) confocal images with orthogonal views. The intensity of AF488-phalloidin and lysozyme fibrils on the dashed line in (a) is plotted in (c).

The AF488-phalloidin intensity of the cage-like structure itself was higher than within the cage, which can also be observed in Figure 4.23c. To verify if the decrease in the intensity of AF488-phalloidin at the position of the fibrils inside the cage was not due to energy transfer, FRET experiments (Förster Resonance Energy Transfer) were performed. If there would be FRET, AF488 intensity is quenched by the presence of AF647. AF488 and AF647 could be FRET pairs, with AF488 as the donor and AF647 as the acceptor. FRET occurs when the fluorophores are in nanometer proximity, which is 5.6 nm for AF488 and AF647 [118]. Appendix Figure D1 shows the excitation and emission spectra of AF488 and AF647, where it can be seen that there is spectral overlap between emission of AF488 and excitation of AF647. This means that theoretically, it is possible for FRET to occur.

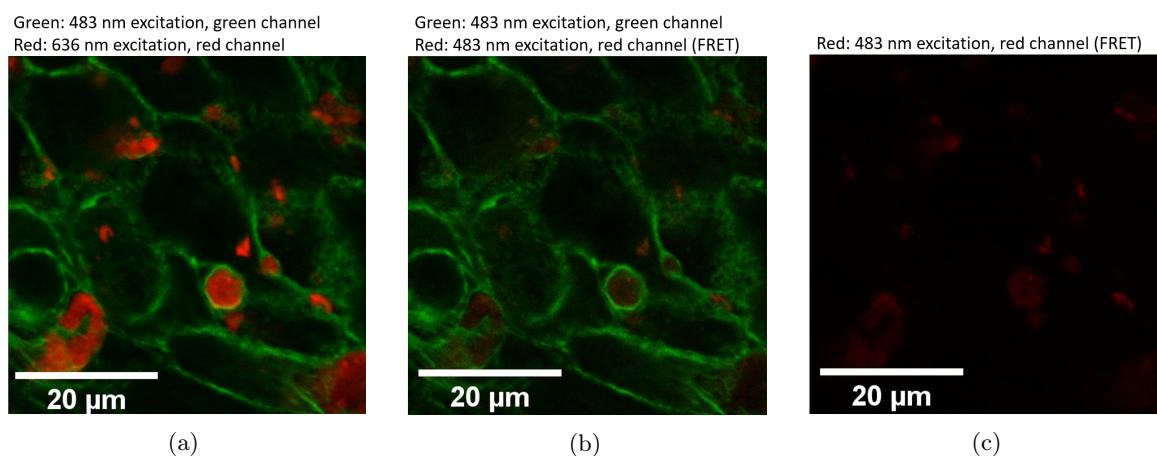


Figure 4.25: Images of Caco-2+HT29MTX cells treated with lysozyme. In (a) and (b), green signal is emission signal from the 483 nm laser. In (a) red is emission signal from the 636 nm excitation laser and in (b) and (c) from the 483 nm laser (FRET signal).

The images that were previously discussed were made with PIE-excitation, which made it possible to analyze the images for FRET. In Figure 4.25a the green signal is AF488 and red signal is AF647. The red signal in Figure 4.25b and 4.25c show FRET signal, which could occur at excitation wavelength of 483 nm and detection in the red channel. The red intensity in these figures is very low, indicating the decrease of intensity at the position of the fibrils was not due to FRET.

To conclude, it seems as if  $\alpha$ -Syn A53T fibrils were not endocytosed by the cells, while lysozyme fibrils were taken up by the cells. This is contradictory to literature, where several mechanisms are described for amyloid fibril uptake. This also includes uptake of  $\alpha$ -Synuclein fibrils by (heparan sulfate-mediated) macropinocytosis [115, 116]. However, the confocal images were taken after 72 hours of treatment. A time-dependent study could be useful to gain further insight. Upon the internalization of lysozyme fibrils, there was remodelling of the F-actin cortex. The mechanism of uptake could be macropinocytosis, as this allows non-specific uptake of different sizes amyloid fibrils [115, 116, 42]. However, from the existing data it is difficult to conclude the mechanism of internalisation.

## 5 Conclusion

The goal of this project was to examine whether food-related amyloid fibrils could translocate across *in vitro* cell models of the epithelial intestinal barrier to evaluate the risk of amyloid fibril exposure. Two amyloid forming proteins found in food are hen egg-white lysozyme and  $\alpha$ -Synuclein, which can be found in for example porcine meat. Hen egg-white lysozyme fibrils and  $\alpha$ -Synuclein fibrils can induce fibrillation of  $\alpha$ -Synuclein, present in for example neurons. This makes exposure to fibrils of these food-related proteins a potential risk for neurodegenerative diseases if these fibrils find their way to the brain. Therefore, knowledge about the ability of these amyloid fibrils to permeate and cross the epithelial barrier in the intestines is of great significance.

Permeability and internalization characteristics of lysozyme and  $\alpha$ -Synuclein amyloid fibrils were evaluated for *in vitro* cell models of the intestinal barrier using Caco-2 cells and HT29MTX cells. Caco-2 cells were differentiated into enterocytes during culturing on transwell membranes. Enterocytes are the most abundant cell type in the intestinal epithelial barrier. The second most abundant cell type are goblet cells, which can be modelled with HT29MTX cells. HT29MTX cells secrete mucus, so by addition of HT29MTX cells, the effect of mucus on permeability characteristics can be determined.

In order to test the quantification method, the permeability of polystyrene (PS) nanobeads through the *in vitro* model was determined as a preliminary model. The results of the preliminary model with PS nanobeads indicated that 20 nm beads cannot permeate across the Caco-2 cell model via the paracellular route, but were probably translocated via the transcellular route. Furthermore, the nanobeads accumulated inside the cytoplasm by the Caco-2 cells. With the Single Particle Tracking (SPT) set-up, the concentration and diameter of nanobeads was accurately determined. However, it was found that the quantification of amyloid fibrils in the SPT-set up was not possible because of the heterogeneity of the fibrils. Because of this, it was decided to continue with bulk fluorescence spectroscopy and Real-Time Quaking-induced Conversion (RT-QuIC) for quantification of the concentration of lysozyme and  $\alpha$ -Syn A53T fibrils, which was used to model animal  $\alpha$ -Synuclein.

The results of the bulk fluorescence spectroscopy indicate that the apparent permeability for amyloid fibrils of both proteins was higher in the Caco-2 model compared to the co-culture. This may indicate that mucus played a role in reducing the ability of lysozyme fibrils to permeate the intestinal barrier. In literature it was found that it is possible for  $\alpha$ -Synuclein monomers to diffuse in mucus [20, 21]. However, the permeation properties might be different for fibrils and for other proteins. Furthermore, the increased thickness of the cell layer of the co-culture because of mucus could lead to a decreased permeability. Next to this, it is known that enterocytes are responsible for transcellular transport. Due to a lower amount of enterocytes in the co-culture model compared to the Caco-2 model, the permeability might be reduced.

The bulk fluorescence spectroscopy results also indicate that the apparent permeability for lysozyme was higher than for  $\alpha$ -Syn A53T in both cell models. However, using bulk fluorescence spectroscopy, it could not be determined if the emission signal originated from fibrils, monomers, free dye or other

structures such as oligomers. A low concentration of monomers and free dye could be present in the samples because of incomplete removal during purification. Next to this, monomers or oligomers could originate from fibril disassembly during exposure to cells. With RT-QuIC, it was attempted to distinguish between fibrils and monomers in the sample by comparing the lag-time of aggregation of  $\alpha$ -Synuclein wt monomers. The basolateral compartment contained mostly monomers, as there was no clear decrease of lag-time of the aggregation of  $\alpha$ -Synuclein wt monomers. However, with the RT-QuIC data, it could not be excluded that the samples also contain a small amount of fibrils. Next to this, these experiments were performed in the absence of proteins and enzymes that may be excreted by the cells and which could alter the lag-time, so further research is needed.

Fluorescence correlation spectroscopy (FCS) was exploited to verify if the samples contained free dye, which could lead to misrepresentation of the bulk fluorescence spectroscopy measurement. It was found that there was no free dye present in the monomer solution diluted in MiliQ. This may indicate that there was no free dye in the samples, so the emission intensity was probably not inflated by the presence of free dye. It was also found in the FCS experiments that there was a population with a small size in the basolateral compartment, which could be monomers that were (partly) degenerated by the cells. A population with a relatively large size was found, which could indicate that proteins from the culture medium or secreted by the cells interact with lysozyme and  $\alpha$ -Syn A53T monomers, forming larger aggregates.

From literature, it was clear that there are several internalization mechanisms for amyloid fibrils by cells [115, 116]. It was hypothesized that lysozyme and  $\alpha$ -Syn A53T fibrils could both be internalized by Caco-2 and HT29MTX cells. Internalization of lysozyme and  $\alpha$ -Syn A53T fibrils was evaluated using confocal scanning laser microscopy. From these experiments, it seemed as if lysozyme fibrils were internalized by the cells, while  $\alpha$ -Syn A53T remained mostly on top of the cells. This could explain the observed difference in apparent permeability. However, the confocal images were taken after 72 hours of treatment. More time points are needed to be sure if  $\alpha$ -Syn A53T was not internalized by the cells. Upon the internalization of lysozyme fibrils, there was remodelling of the F-actin cortex. The mechanism of uptake could be macropinocytosis, as this allows non-specific uptake of different sizes amyloid fibrils. The exact mechanism cannot be known from the available data.

Altogether, the results of this research indicate that hen egg-white lysozyme fibrils, can cross the *in vitro* intestinal epithelial cell models used in this study more easily than  $\alpha$ -Syn A53T fibrils, which was used as a model for animal  $\alpha$ -Syn. However, from the data available, it was not possible to get a clear indication about the aggregation state of the translocated food proteins. The samples that permeated the *in vitro* cell models could contain fibrils, oligomers or monomers. Lysozyme was internalized by the cells, while  $\alpha$ -Syn A53T seems to be attached to the top side of the cell layer. This might be a possible explanation for the difference in permeability observed. However, more research is needed to support these findings.

## 6 Recommendations

The results of this research indicated that lysozyme could more easily cross the *in vitro* barriers used in this study, compared to  $\alpha$ -Syn A53T. The exact aggregation state (monomers, oligomers or fibrils) of the permeated lysozyme, however, was not clear from the results. More research is needed to support these findings and to further investigate the effect of food-related amyloid fibrils on neurodegenerative diseases. In this chapter, recommendations will be presented for further research.

The research was performed with *in vitro* cell models of the epithelial intestinal layer. The model in the preliminary model with PS nanobeads only contained Caco-2 cells. Differentiated Caco-2 cells show many characteristics of enterocytes. However, it is reported that Caco-2 layers fail to provide a reliable estimation of *in vivo* permeability because of the overexpression of TJ-proteins [51, 54] and the absence of other cell types [44]. For the permeability experiments for amyloid fibrils, a co-culture model with Caco-2 cells and HT29MTX was used, which was a more close representation of the *in vivo* situation [53]. This model is ideal for *in vitro* measurements. However, this model lacks different neighbouring cells, such as M-cells. M-cells are responsible for the uptake and transport of substances [33], so by excluding M-cells, it could be possible that some routes for transportation were also excluded. Next to this, blood flow and other environmental conditions were lacking in the model [51]. Therefore, these experiments should be repeated *in vivo*.

An increase of the measured TEER-values indicated that TJ-complexes were formed during 21 days of culturing of the Caco-2 and HT29MTX cells on transwell membrane. This was the only verification of differentiation of Caco-2 cells into enterocytes. There are several ways to verify this, which can be performed in further research. A staining of wheat germ agglutinin (WGA) conjugated to a fluorescence dye can be done to stain N-acetylneuraminic sialic acid, which is only present on the cell surface of differentiated Caco-2 cells [119]. The presence of microvilli can be examined in electron microscopy [32, 119]. Finally, the expression of TJ-proteins can be investigated with PCR or Western blotting.

The bulk fluorescence measurements showed that there was an increase of the fluorescence signal in the basolateral compartment over time. This signal could originate from fibrils, monomers or free dye. Distinguishing between these three was done with RT-QuIC. The control groups to make a calibration curve in the RT-QuIC experiments were not performed in conditioned cell culture medium, but were performed in fresh culture medium. This means that the experiments were performed in the absence of proteins and enzymes secreted by the cells. The presence of such proteins could influence the aggregation, as discussed in the Results and Discussion section. The RT-QuIC calibration experiments should be performed in cell culture medium retrieved from cells in culture.

Finally,  $\alpha$ -Syn A53T used in this research contained the sequence of human  $\alpha$ -Syn, except for the threonine at residue 53. This variant was used, as it was observed in animals consumed by humans. There are more differences in sequence between human  $\alpha$ -Syn and animal  $\alpha$ -Syn, which may change physico-chemical properties of  $\alpha$ -Syn. For example, Larsen et al. [68] showed that porcine  $\alpha$ -Syn has a decreased propensity for fibrillation compared to human  $\alpha$ -Syn. It is not known if the ability to induce aggrega-

tion of human  $\alpha$ -Syn wt monomers is different for porcine or other animal  $\alpha$ -Syn. Next to this, another change in amino acid sequence was done at residue 140 for labelling purposes. The effect of this change and the effect of the A647 label on aggregation or permeability characteristics is not known. For further research,  $\alpha$ -Syn directly taken from meat or milk should be used, as the differences in amino acid sequence may influence the permeability or fibrillation characteristics of  $\alpha$ -Syn. RT-QuIC experiments could be performed with unlabelled lysozyme and animal  $\alpha$ -Syn.

Next to improving the experimental design of this research, extensive research is necessary to evaluate the risks associated with amyloid fibril exposure. The cross-aggregation ability of lysozyme and animal  $\alpha$ -Syn with  $\alpha$ -Syn wt and other disease-related proteins should be tested in actual physiological conditions. Finally, the ability of amyloid fibrils to translocate to the brain via the vagus nerve or blood to cross the blood-brain barrier should be evaluated. Researches of the NBP-group in the DOMINOS project are already working on this. Together with the research described in this thesis, this research will give insights into the risks associated with food-related amyloid fibrils.

## Acknowledgements

I could not have done this project without the help of so many people, so I would like to thank all of them.

First of all, I would like to thank Ayeman Amanullah for being my daily supervisor and for being there literally every day to help me with my problems and answering my questions. Thanks for being patient when you had to tell me things twice (or more). I really learned a lot from you.

Mireille Claessens and Christian Blum, thank you for giving me the opportunity for working in the NanoBioPhysics group. Thanks for all the ideas and suggestions you gave me during the meetings and for always having the doors of your offices open, so I could always walk in and ask questions.

Kerensa Broersen and Ine Segers-Nolten for giving suggestions for new experiments during the meetings. And Kerensa, for being the external member of my graduation committee.

Thanks to all the people of the NBP-group, who I've got to know during my project and who made me feel welcome in the group. Jonathan, thanks for helping me with all the work in the lab with the amyloid fibrils and to think with me about the results. Amin and Robert, who have helped me with all the set-ups and techniques I have used. Without you, I would have been lost in the optical lab. Swarupa, thanks for helping me with the nanobeads and the 'Swarupa-set up'. Kirsten, I would like to thank you for preparing all the  $\alpha$ -Synuclein samples. I would like to thank all the students at NBP, who have contributed in the meetings. Especially, I would like to thank Sybren, for being my graduation-, ub- and lab-buddy during our time at NBP.

A very big thanks to Maxim and Ceri-Anne, who gave me suggestions and new insights on my thesis. Finally, I would like to thank all of my friends and family for their love and support throughout the years.

## References

- [1] F. Chiti and C. M. Dobson, "Protein misfolding, amyloid formation, and human disease: A summary of progress over the last decade," *Annual Review of Biochemistry*, vol. 86, pp. 27–68, 6 2017.
- [2] J. L. M. R. K. R. Bruce Alberts, Alexander Johnson and P. Walter, *Molecular Biology of the Cell, 4th edition*. 2002.
- [3] C. M. Dobson, "Protein folding and misfolding," *Nature*, vol. 426, pp. 884–890, 12 2003.
- [4] S. Mankar, A. Anoop, S. Sen, and S. K. Maji, "Nanomaterials: amyloids reflect their brighter side," *Nano Reviews*, vol. 2, p. 6032, 1 2011.
- [5] R. N. Rambaran and L. C. Serpell, "Amyloid fibrils: abnormal protein assembly.," *Prion*, vol. 2, no. 3, pp. 112–117, 2008.
- [6] I. Segers-Nolten, M. Van Raaij, and V. Subramaniam, "2.19 Biophysical analysis of amyloid formation," in *Comprehensive Biomaterials II*, pp. 438–451, Elsevier, 1 2017.
- [7] T. Scheibel, R. Parthasarathy, G. Sawicki, X. M. Lin, H. Jaeger, and S. L. Lindquist, "Conducting nanowires built by controlled self-assembly of amyloid fibers and selective metal deposition," *Proceedings of the National Academy of Sciences of the United States of America*, vol. 100, pp. 4527–4532, 4 2003.
- [8] V. Sivalingam, N. L. Prasanna, N. Sharma, A. Prasad, and B. K. Patel, "Wild-type hen egg white lysozyme aggregation in vitro can form self-seeding amyloid conformational variants," *Biophysical Chemistry*, vol. 219, pp. 28–37, 12 2016.
- [9] B. A. Killinger and V. Labrie, "Vertebrate food products as a potential source of prion-like  $\alpha$ -synuclein," *npj Parkinson's Disease*, vol. 3, pp. 1–11, 12 2017.
- [10] R. Tacoma, J. Fields, D. B. Ebenstein, Y. W. Lam, and S. L. Greenwood, "Characterization of the bovine milk proteome in early-lactation Holstein and Jersey breeds of dairy cows," *Journal of Proteomics*, vol. 130, pp. 200–210, 1 2016.
- [11] J. Vaneyck, I. Segers-Nolten, K. Broersen, and M. M. Claessens, "Cross-seeding of alpha-synuclein aggregation by amyloid fibrils of food proteins," *Journal of Biological Chemistry*, vol. 296, p. 100358, 2 2021.
- [12] A. Sidhu, I. Segers-Nolten, and V. Subramaniam, "Conformational Compatibility Is Essential for Heterologous Aggregation of  $\alpha$ -Synuclein," *ACS Chemical Neuroscience*, vol. 7, pp. 719–727, 6 2016.
- [13] H. A. Lashuel, C. R. Overk, A. Oueslati, and E. Masliah, "The many faces of  $\alpha$ -synuclein: From structure and toxicity to therapeutic target," *Nature Reviews Neuroscience*, vol. 14, pp. 38–48, 1 2013.
- [14] S. Holmqvist, O. Chutna, L. Bousset, P. Aldrin-Kirk, W. Li, T. Björklund, Z. Y. Wang, L. Roybon, R. Melki, and J. Y. Li, "Direct evidence of Parkinson pathology spread from the gastrointestinal tract to the brain in rats," *Acta Neuropathologica*, vol. 128, pp. 805–820, 11 2014.
- [15] C. A. Bates, S. Fu, D. Ysselstein, J. C. Rochet, and W. Zheng, "Expression and transport of  $\alpha$ -synuclein at the blood-cerebrospinal fluid barrier and effects of manganese exposure," *ADMET and DMPK*, vol. 3, pp. 15–33, 3 2015.
- [16] J. Keaney, D. M. Walsh, T. O'Malley, N. Hudson, D. E. Crosbie, T. Loftus, F. Sheehan, J. McDaid, M. M. Humphries, J. J. Callanan, F. M. Brett, M. A. Farrell, P. Humphries, and M. Campbell, "Autoregulated paracellular clearance of amyloid- $\beta$  across the blood-brain barrier," *Science Advances*, vol. 1, p. e1500472, 9 2015.

- [17] A. Hartsock and W. J. Nelson, "Adherens and tight junctions: Structure, function and connections to the actin cytoskeleton," *Biochimica et Biophysica Acta - Biomembranes*, vol. 1778, pp. 660–669, 3 2008.
- [18] W. L. Kuan, N. Bennett, X. He, J. N. Skepper, N. Martynyuk, R. Wijeyekoon, P. V. Moghe, C. H. Williams-Gray, and R. A. Barker, " $\alpha$ -Synuclein pre-formed fibrils impair tight junction protein expression without affecting cerebral endothelial cell function," *Experimental Neurology*, vol. 285, pp. 72–81, 11 2016.
- [19] K. L. Puig, G. D. Manocha, and C. K. Combs, "Amyloid Precursor Protein Mediated Changes in Intestinal Epithelial Phenotype In Vitro," *PLOS ONE*, vol. 10, p. e0119534, 3 2015.
- [20] M. Marczynski, C. A. Rickert, S. A. Semerdzhiev, W. R. Van Dijk, I. M. J. Segers-Nolten, M. M. A. E. Claessens, and O. Lieleg, " $\alpha$ -Synuclein Penetrates Mucin Hydrogels Despite Its Mucoadhesive Properties," 2019.
- [21] M. Marczynski, B. T. Käsdorf, B. Altaner, A. Wenzler, U. Gerland, and O. Lieleg, "Transient binding promotes molecule penetration into mucin hydrogels by enhancing molecular partitioning," *Biomaterials Science*, vol. 6, pp. 3373–3387, 12 2018.
- [22] M. Lassé, D. Ulluwishewa, J. Healy, D. Thompson, A. Miller, N. Roy, K. Chitcholtan, and J. A. Gerrard, "Evaluation of protease resistance and toxicity of amyloid-like food fibrils from whey, soy, kidney bean, and egg white," *Food Chemistry*, vol. 192, pp. 491–498, 7 2016.
- [23] J. Geys, L. Coenegrachts, J. Vercaemmen, Y. Engelborghs, A. Nemmar, B. Nemery, and P. H. Hoet, "In vitro study of the pulmonary translocation of nanoparticles: A preliminary study," *Toxicology Letters*, vol. 160, pp. 218–226, 1 2006.
- [24] E. Rytting, Cartwright, Poulsen, Nielsen, Pojana, Knudsen, and Saunders, "In vitro placental model optimization for nanoparticle transport studies," *International Journal of Nanomedicine*, vol. 7, p. 497, 1 2012.
- [25] M. Ayer, M. Schuster, I. Gruber, C. Blatti, E. Kaba, G. Enzmann, O. Burri, R. Guiet, A. Seitz, B. Engelhardt, and H. Klok, "T Cell [U+2010] Mediated Transport of Polymer Nanoparticles across the Blood–Brain Barrier," *Advanced Healthcare Materials*, vol. 10, p. 2001375, 1 2021.
- [26] A. P. Walczak, E. Kramer, P. J. M. Hendriksen, P. Tromp, J. P. F. G. Helsper, M. van der Zande, I. M. C. M. Rietjens, and H. Bouwmeester, "Translocation of differently sized and charged polystyrene nanoparticles in *in vitro* intestinal cell models of increasing complexity," *Nanotoxicology*, vol. 9, pp. 453–461, 5 2015.
- [27] A. M. Bannunah, D. Vllasaliu, J. Lord, and S. Stolnik, "Mechanisms of nanoparticle internalization and transport across an intestinal epithelial cell model: Effect of size and surface charge," *Molecular Pharmaceutics*, vol. 11, pp. 4363–4373, 12 2014.
- [28] J. Domenech, A. Hernández, L. Rubio, R. Marcos, and C. Cortés, "Interactions of polystyrene nanoplastics with *in vitro* models of the human intestinal barrier," *Archives of Toxicology*, vol. 94, pp. 2997–3012, 9 2020.
- [29] M. Hesler, L. Aengenheister, B. Ellinger, R. Drexel, S. Straskraba, C. Jost, S. Wagner, F. Meier, H. von Briesen, C. Büchel, P. Wick, T. Buerki-Thurnherr, and Y. Kohl, "Multi-endpoint toxicological assessment of polystyrene nano- and microparticles in different biological models *in vitro*," *Toxicology in Vitro*, vol. 61, p. 104610, 12 2019.
- [30] C. Cortés, J. Domenech, M. Salazar, S. Pastor, R. Marcos, and A. Hernández, "Nanoplastics as a potential environmental health factor: Effects of polystyrene nanoparticles on human intestinal epithelial Caco-2

- cells,” *Environmental Science: Nano*, vol. 7, pp. 272–285, 1 2020.
- [31] S. Kong, Y. H. Zhang, and W. Zhang, “Regulation of intestinal epithelial cells properties and functions by amino acids,” *BioMed Research International*, vol. 2018, 2018.
- [32] J. R. Turner, “Intestinal mucosal barrier function in health and disease,” *Nature Reviews Immunology*, vol. 9, pp. 799–809, 11 2009.
- [33] J. M. Allaire, S. M. Crowley, H. T. Law, S.-Y. Chang, H.-J. Ko, and B. A. Vallance, “The Intestinal Epithelium: Central Coordinator of Mucosal Immunity,” *Trends in Immunology*, vol. 39, pp. 677–696, 2018.
- [34] J. A. Grondin, Y. H. Kwon, P. M. Far, S. Haq, and W. I. Khan, “Mucins in Intestinal Mucosal Defense and Inflammation: Learning From Clinical and Experimental Studies,” *Frontiers in Immunology*, vol. 11, p. 2054, 9 2020.
- [35] J. T. Collins and S. S. Bhimji, *Anatomy, Abdomen and Pelvis, Small Intestine*. StatPearls Publishing, 8 2018.
- [36] M. Yu, Y. Yang, C. Zhu, S. Guo, and Y. Gan, “Advances in the transepithelial transport of nanoparticles,” *Drug Discovery Today*, vol. 21, pp. 1155–1161, 7 2016.
- [37] M. M. France and J. R. Turner, “The mucosal barrier at a glance,” *Journal of Cell Science*, vol. 130, no. 2, pp. 307–314, 2017.
- [38] Y. Yun, Y. W. Cho, and K. Park, “Nanoparticles for oral delivery: Targeted nanoparticles with peptidic ligands for oral protein delivery,” *Advanced Drug Delivery Reviews*, vol. 65, pp. 822–832, 6 2013.
- [39] M. M. Buschmann, L. Shen, H. Rajapakse, D. R. Raleigh, Y. Wang, Y. Wang, A. Lingaraju, J. Zha, E. Abbott, E. M. McAuley, L. A. Breskin, L. Wu, K. Anderson, J. R. Turner, and C. R. Weber, “Occludin OCEL-domain interactions are required for maintenance and regulation of the tight junction barrier to macromolecular flux,” *Molecular Biology of the Cell*, vol. 24, pp. 3056–3068, 10 2013.
- [40] M. C. Chen, F. L. Mi, Z. X. Liao, C. W. Hsiao, K. Sonaje, M. F. Chung, L. W. Hsu, and H. W. Sung, “Recent advances in chitosan-based nanoparticles for oral delivery of macromolecules,” *Advanced Drug Delivery Reviews*, vol. 65, pp. 865–879, 6 2013.
- [41] G. H. Liang and C. R. Weber, “Molecular aspects of tight junction barrier function,” *Current Opinion in Pharmacology*, vol. 19, pp. 84–89, 12 2014.
- [42] S. Behzadi, V. Serpooshan, W. Tao, M. A. Hamaly, M. Y. Alkawareek, E. C. Dreaden, D. Brown, A. M. Alkilany, O. C. Farokhzad, and M. Mahmoudi, “Cellular uptake of nanoparticles: Journey inside the cell,” *Chemical Society Reviews*, vol. 46, pp. 4218–4244, 7 2017.
- [43] K. Takei and V. Haucke, “Clathrin-mediated endocytosis: Membrane factors pull the trigger,” *Trends in Cell Biology*, vol. 11, pp. 385–391, 9 2001.
- [44] A. F. Strugari, M. S. Stan, S. Gharbia, A. Hermenean, and A. Dinischiotu, “Characterization of nanoparticle intestinal transport using an in vitro co-culture model,” *Nanomaterials*, vol. 9, 1 2019.
- [45] B. Srinivasan, A. R. Kolli, M. B. Esch, H. E. Abaci, M. L. Shuler, and J. J. Hickman, “TEER Measurement Techniques for In Vitro Barrier Model Systems,” *Journal of Laboratory Automation*, vol. 20, pp. 107–126, 4 2015.
- [46] R. B. Van Breemen and Y. Li, “Caco-2 cell permeability assays to measure drug absorption,” *Expert Opinion on Drug Metabolism and Toxicology*, vol. 1, pp. 175–185, 8 2005.
- [47] M. Natoli, B. D. Leoni, I. D’Agnano, F. Zucco, and A. Felsani, “Good Caco-2 Cell Culture Practices,” *Toxicology in Vitro*, vol. 26, pp. 1243–1246, 12 2012.

- [48] R. T. Borchardt, “Hidalgo, I. J., Raub, T. J., and Borchardt, R. T.: Characterization of the human colon carcinoma cell line (Caco-2) as a model system for intestinal epithelial permeability, gastroenterology, 96, 736-749, 1989-The Backstory,” *AAPS Journal*, vol. 13, pp. 323–327, 9 2011.
- [49] K. Verhoeckx, P. Cotter, I. López-Expósito, C. Kleiveland, T. Lea, A. Mackie, T. Requena, D. Swiatecka, and H. Wichers, *The impact of food bioactives on health: In vitro and Ex Vivo models*. Springer International Publishing, 1 2015.
- [50] D. Martínez-Maqueda, B. Miralles, and I. Recio, “HT29 cell line,” in *The Impact of Food Bioactives on Health: In Vitro and Ex Vivo Models*, pp. 113–124, Springer International Publishing, 1 2015.
- [51] K. Lenaerts, F. K. Bouwman, W. H. Lamers, J. Renes, and E. C. Mariman, “Comparative proteomic analysis of cell lines and scrapings of the human intestinal epithelium,” *BMC Genomics*, vol. 8, p. 91, 4 2007.
- [52] C. R. Kleiveland, “Co-cultivation of caco-2 and HT-29MTX,” in *The Impact of Food Bioactives on Health: In Vitro and Ex Vivo Models*, pp. 135–140, Springer International Publishing, 1 2015.
- [53] A. Béduneau, C. Tempesta, S. Fimbel, Y. Pellequer, V. Jannin, F. Demarne, and A. Lamprecht, “A tunable Caco-2/HT29-MTX co-culture model mimicking variable permeabilities of the human intestine obtained by an original seeding procedure,” *European Journal of Pharmaceutics and Biopharmaceutics*, vol. 87, pp. 290–298, 7 2014.
- [54] A. S. Fanning, C. M. Van Itallie, and J. M. Anderson, “Zonula occludens-1 and -2 regulate apical cell structure and the zonula adherens cytoskeleton in polarized epithelia,” *Molecular Biology of the Cell*, vol. 23, pp. 577–590, 2 2012.
- [55] E. Walter, S. Janich, B. J. Roessler, J. M. Hilfinger, and G. L. Amidon, “HT29-MTX/Caco-2 cocultures as an in vitro model for the intestinal epithelium: In vitro-in vivo correlation with permeability data from rats and humans,” *Journal of Pharmaceutical Sciences*, vol. 85, pp. 1070–1076, 10 1996.
- [56] “Epithelial Volt/Ohm Meter | Surgical Instruments, Research Instruments, Laboratory Equipment | WPI.”
- [57] C. Hilgendorf, H. Spahn-Langguth, C. G. Regårdh, E. Lipka, G. L. Amidon, and P. Langguth, “Caco-2 versus Caco-2/HT29-MTX co-cultured cell lines: Permeabilities via diffusion, inside- and outside-directed carrier-mediated transport,” *Journal of Pharmaceutical Sciences*, vol. 89, pp. 63–75, 1 2000.
- [58] M. Vázquez, M. Calatayud, D. Vélez, and V. Devesa, “Intestinal transport of methylmercury and inorganic mercury in various models of Caco-2 and HT29-MTX cells,” *Toxicology*, vol. 311, pp. 147–153, 9 2013.
- [59] S. I. Cohen, M. Vendruscolo, C. M. Dobson, and T. P. Knowles, “From macroscopic measurements to microscopic mechanisms of protein aggregation,” *Journal of Molecular Biology*, vol. 421, pp. 160–171, 8 2012.
- [60] S. Y. Ow and D. E. Dunstan, “A brief overview of amyloids and Alzheimer’s disease,” *Protein Science*, vol. 23, pp. 1315–1331, 10 2014.
- [61] A. L. Gharibyan, V. Zamotin, K. Yanamandra, O. S. Moskaleva, B. A. Margulis, I. A. Kostanyan, and L. A. Morozova-Roche, “Lysozyme Amyloid Oligomers and Fibrils Induce Cellular Death via Different Apoptotic/Necrotic Pathways,” *Journal of Molecular Biology*, vol. 365, pp. 1337–1349, 2 2007.
- [62] “Hen Egg-White (HEW) Lysozyme - Proteopedia, life in 3D.”
- [63] Y. Cao and R. Mezzenga, “Food protein amyloid fibrils: Origin, structure, formation, characterization, applications and health implications,” *Advances in Colloid and Interface Science*, vol. 269, pp. 334–356, 7 2019.

- [64] E. Frare, P. Polverino De Laureto, J. Zurdo, C. M. Dobson, and A. Fontana, “A highly amyloidogenic region of hen lysozyme,” *Journal of Molecular Biology*, vol. 340, pp. 1153–1165, 7 2004.
- [65] L. K. Sanders, C. Guáqueta, T. E. Angelini, J.-W. Lee, S. C. Slimmer, E. Lujten, and G. C. L. Wong, “Structure and Stability of Self-Assembled Actin-Lysozyme Complexes in Salty Water,” 2005.
- [66] M. H. Polymeropoulos, C. Lavedan, E. Leroy, S. E. Ide, A. Dehejia, A. Dutra, B. Pike, H. Root, J. Rubenstein, R. Boyer, E. S. Stenroos, S. Chandrasekharappa, A. Athanassiadou, T. Papapetropoulos, W. G. Johnson, A. M. Lazzarini, R. C. Duvoisin, G. Di Iorio, L. I. Golbe, and R. L. Nussbaum, “Mutation in the  $\alpha$ -synuclein gene identified in families with Parkinson’s disease,” *Science*, vol. 276, pp. 2045–2047, 6 1997.
- [67] G. Yamin, L. A. Munishkina, M. A. Karymov, Y. L. Lyubchenko, V. N. Uversky, and A. L. Fink, “Forcing nonamyloidogenic  $\beta$ -synuclein to fibrillate,” *Biochemistry*, vol. 44, pp. 9096–9107, 6 2005.
- [68] K. Larsen, R. Bæk, C. Sahin, L. Kjær, G. Christiansen, J. Nielsen, L. Farajzadeh, and D. E. Otzen, “Molecular characteristics of porcine alpha-synuclein splicing variants,” *Biochimie*, vol. 180, pp. 121–133, 1 2021.
- [69] C. Sahin, L. Kjær, M. S. Christensen, J. N Pedersen, G. Christiansen, A. M. W. Pérez, I. M. Møller, J. J. Enghild, J. S. Pedersen, K. Larsen, and D. E. Otzen, “ $\alpha$ -Synucleins from Animal Species Show Low Fibrillation Propensities and Weak Oligomer Membrane Disruption,” *Biochemistry*, vol. 57, pp. 5145–5158, 8 2018.
- [70] M. J. Sanderson, I. Smith, I. Parker, and M. D. Bootman, “Fluorescence microscopy,” *Cold Spring Harbor Protocols*, vol. 2014, pp. 1042–1065, 10 2014.
- [71] D. D. Vvedensky and D. D. Vvedensky, “Brownian motion, random walks, and the diffusion equation,” in *Transformations of Materials*, IOP Publishing, 2019.
- [72] N. Ruthardt, D. C. Lamb, and C. Bräuchle, “Single-particle tracking as a quantitative microscopy-based approach to unravel cell entry mechanisms of viruses and pharmaceutical nanoparticles,” *Molecular Therapy*, vol. 19, no. 7, pp. 1199–1211, 2011.
- [73] J. C. Crocker and D. G. Grier, “Methods of digital video microscopy for colloidal studies,” *Journal of Colloid and Interface Science*, vol. 179, pp. 298–310, 4 1996.
- [74] R. Molenaar, S. Chatterjee, B. Kamphuis, I. M. J. Segers-Nolten, M. M. A. E. Claessens, and C. Blum, “Nanoplastic sizes and numbers: quantification by single particle tracking,” *Environmental Science: Nano*, vol. 8, p. 723, 3 2021.
- [75] B. R. Groveman, C. D. Orrù, A. G. Hughson, L. D. Raymond, G. Zanusso, B. Ghetti, K. J. Campbell, J. Safar, D. Galasko, and B. Caughey, “Rapid and ultra-sensitive quantitation of disease-associated  $\alpha$ -synuclein seeds in brain and cerebrospinal fluid by  $\alpha$ Syn RT-QuIC,” *Acta Neuropathologica Communications*, vol. 6, p. 7, 12 2018.
- [76] M. Shahnawaz, T. Tokuda, M. Waraga, N. Mendez, R. Ishii, C. Trenkwalder, B. Mollenhauer, and C. Soto, “Development of a biochemical diagnosis of Parkinson disease by detection of  $\alpha$ -synuclein misfolded aggregates in cerebrospinal fluid,” *JAMA Neurology*, vol. 74, pp. 163–172, 2 2017.
- [77] B. Caughey, C. D. Orru, B. R. Groveman, M. Bongiani, A. G. Hughson, L. D. Raymond, M. Manca, A. Kraus, G. J. Raymond, M. Fiorini, M. Pocchiari, and G. Zanusso, “Detection and diagnosis of prion diseases using RT-QuIC: An update,” *Neuromethods*, vol. 129, pp. 173–181, 2017.
- [78] R. Morales, I. Moreno-Gonzalez, and C. Soto, “Cross-Seeding of Misfolded Proteins: Implications for Etiology and Pathogenesis of Protein Misfolding Diseases,” *PLoS Pathogens*, vol. 9, 9 2013.

- [79] S. Paciotti, G. Bellomo, L. Gatticchi, and L. Parnetti, "Are we ready for detecting  $\alpha$ -synuclein prone to aggregation in patients? The case of "Protein-Misfolding Cyclic Amplification" and "Real-Time Quaking-Induced Conversion" as diagnostic tools," *Frontiers in Neurology*, vol. 9, p. 415, 6 2018.
- [80] Z. Qin, Y. Sun, B. Jia, D. Wang, Y. Ma, and G. Ma, "Kinetic Mechanism of Thioflavin T Binding onto the Amyloid Fibril of Hen Egg White Lysozyme," *Langmuir*, vol. 33, pp. 5398–5405, 6 2017.
- [81] A. Sidhu, J. Vaneyck, C. Blum, I. Segers-Nolten, and V. Subramaniam, "Polymorph-specific distribution of binding sites determines thioflavin-T fluorescence intensity in  $\alpha$ -synuclein fibrils," *Amyloid*, vol. 25, pp. 189–196, 7 2018.
- [82] R. Atarashi, K. Satoh, K. Sano, T. Fuse, N. Yamaguchi, D. Ishibashi, T. Matsubara, T. Nakagaki, H. Yamanaoka, S. Shirabe, M. Yamada, H. Mizusawa, T. Kitamoto, G. Klug, A. McGlade, S. J. Collins, and N. Nishida, "Ultrasensitive human prion detection in cerebrospinal fluid by real-time quaking-induced conversion," *Nature Medicine*, vol. 17, pp. 175–178, 2 2011.
- [83] C. W. Yang, I. S. Hwang, Y. F. Chen, C. S. Chang, and D. P. Tsai, "Imaging of soft matter with tapping-mode atomic force microscopy and non-contact-mode atomic force microscopy," *Nanotechnology*, vol. 18, 2 2007.
- [84] "Protocol Guide: MTT Assay for Cell Viability and Proliferation | Sigma-Aldrich."
- [85] T. L. Riss, R. A. Moravec, A. L. Niles, S. Duellman, H. A. Benink, T. J. Worzella, and L. Minor, "Cell Viability Assays," *Assay Guidance Manual*, 7 2004.
- [86] C. M. St. Croix, S. H. Shand, and S. C. Watkins, "Confocal microscopy: comparisons, applications, and problems," *BioTechniques*, vol. 39, pp. S2–S5, 12 2005.
- [87] "FluoSpheres™ Carboxylate-Modified Microspheres, 0.02  $\mu$ m, dark red fluorescent (660/680), 2% solids."
- [88] "3000 Series Nanosphere™ Size Standards."
- [89] "Amine-Reactive Crosslinker Chemistry | Thermo Fisher Scientific - NL."
- [90] "Alexa Fluor™ 647 NHS Ester (Succinimidyl Ester)."
- [91] "Sulfhydryl-Reactive Crosslinker Chemistry | Thermo Fisher Scientific - NL."
- [92] L. Davis and G. Shen, "Accounting for Triplet and Saturation Effects in FCS Measurements," *Current Pharmaceutical Biotechnology*, vol. 7, pp. 287–301, 7 2006.
- [93] C. M. H. Ae, N. Starostin, A. E. Paul, W. Ae, and M. L. Mecartney, "A comparison of atomic force microscopy (AFM) and dynamic light scattering (DLS) methods to characterize nanoparticle size distributions," 2008.
- [94] T. Ishikawa, B. L. Zhu, and H. Maeda, "Effect of sodium azide on the metabolic activity of cultured fetal cells," *Toxicology and Industrial Health*, vol. 22, pp. 337–341, 9 2006.
- [95] A. Banerjee, J. Qi, R. Gogoi, J. Wong, and S. Mitragotri, "Role of nanoparticle size, shape and surface chemistry in oral drug delivery," *Journal of Controlled Release*, vol. 238, pp. 176–185, 9 2016.
- [96] G. Palazzo and D. Berti, "Diffusion and Aggregation," in *Colloidal Foundations of Nanoscience*, pp. 199–231, Elsevier Inc., 2014.
- [97] A. Martinez-Palomo, I. Meza, G. Beaty, and M. Cereijido, "Experimental modulation of occluding junctions in a cultured transporting epithelium," *Journal of Cell Biology*, vol. 87, pp. 736–745, 12 1980.
- [98] H. Baghirova, D. Karaman, T. Viitala, A. Duchanoy, Y.-R. Lou, V. Mamaeva, E. Pryazhnikov, L. Khirouq, C. de Lange Davies, C. Sahlgren, and J. M. Rosenholm, "Feasibility Study of the Permeability and Uptake of Mesoporous Silica Nanoparticles across the Blood-Brain Barrier," *PLOS ONE*, vol. 11,

- p. e0160705, 8 2016.
- [99] A. Avdeef, P. E. Nielsen, and O. Tsinman, "PAMPA - A drug absorption in vitro model: 11. Matching the in vivo unstirred water layer thickness by individual-well stirring in microtitre plates," *European Journal of Pharmaceutical Sciences*, vol. 22, pp. 365–374, 8 2004.
- [100] C. M. Van Itallie, A. S. Fanning, A. Bridges, and J. M. Anderson, "ZO-1 stabilizes the tight junction solute barrier through coupling to the perijunctional cytoskeleton," *Molecular Biology of the Cell*, vol. 20, pp. 3930–3940, 9 2009.
- [101] N. Navabi, M. A. McGuckin, and S. K. Lindén, "Gastrointestinal Cell Lines Form Polarized Epithelia with an Adherent Mucus Layer when Cultured in Semi-Wet Interfaces with Mechanical Stimulation," *PLoS ONE*, vol. 8, p. 68761, 7 2013.
- [102] I. Röhe, F. J. Hüttner, J. Plendl, B. Drewes, and J. Zentek, "Comparison of different histological protocols for the preservation and quantification of the intestinal mucus layer in pigs," *European Journal of Histochemistry*, vol. 62, pp. 63–70, 2 2018.
- [103] M. Abolbashari, G. Babaie, F. Magalhães, M. V. Correia, F. M. Araújo, A. S. Gerges, and F. Farahi, "Biological imaging with high dynamic range using compressive imaging technique," *Imaging, Manipulation, and Analysis of Biomolecules, Cells, and Tissues X*, vol. 8225, p. 82251X, 2 2012.
- [104] K. Cheng, A. Sloan, K. M. Avery, M. Coulthart, M. Carpenter, and J. D. Knox, "Exploring physical and chemical factors influencing the properties of recombinant prion protein and the real-time quaking-induced conversion (RT-QuIC) assay," *PLoS ONE*, vol. 9, 1 2014.
- [105] "Fluorescence Correlation Spectroscopy (FCS) | PicoQuant."
- [106] V. Buschmann, B. Krämer, F. Koberling, P. Gmbh, R. Macdonald, and S. Rüttinger, "Quantitative FCS: Determination of the Confocal Volume by FCS and Bead Scanning with the MicroTime 200,"
- [107] A. Loman, *Molecular Sizing using Fluorescence Correlation Spectroscopy (Thesis)*. PhD thesis, Georg-August-Universität Göttingen, 2010.
- [108] "Alexa Fluor™ 488 Phalloidin."
- [109] H. Lodish, A. Berk, S. L. Zipursky, P. Matsudaira, D. Baltimore, and J. Darnell, "The Actin Cytoskeleton," 2000.
- [110] "DAPI (4',6-Diamidino-2-Phenylindole, Dilactate)."
- [111] M. Oshiro, K. Ono, Y. Suzuki, H. Ota, T. Katsuyama, and N. Mori, "Immunohistochemical localization of heparan sulfate proteoglycan in human gastrointestinal tract," *Histochemistry and Cell Biology*, vol. 115, no. 5, pp. 373–380, 2001.
- [112] H. C. Christianson and M. Belting, "Heparan sulfate proteoglycan as a cell-surface endocytosis receptor," *Matrix Biology*, vol. 35, pp. 51–55, 4 2014.
- [113] E. Sandwall, P. O'Callaghan, X. Zhang, U. Lindahl, L. Lannfelt, and J. P. Li, "Heparan sulfate mediates amyloid-beta internalization and cytotoxicity," *Glycobiology*, vol. 20, pp. 533–541, 5 2010.
- [114] E. Ihse, H. Yamakado, X. M. Van Wijk, R. Lawrence, J. D. Esko, and E. Masliah, "Cellular internalization of alpha-synuclein aggregates by cell surface heparan sulfate depends on aggregate conformation and cell type," *Scientific Reports*, vol. 7, pp. 1–10, 12 2017.
- [115] B. B. Holmes, S. L. DeVos, N. Kfoury, M. Li, R. Jacks, K. Yanamandra, M. O. Ouidja, F. M. Brodsky, J. Marasa, D. P. Bagchi, P. T. Kotzbauer, T. M. Miller, D. Papy-Garcia, and M. I. Diamond, "Heparan sulfate proteoglycans mediate internalization and propagation of specific proteopathic seeds," *Proceedings of the National Academy of Sciences of the United States of America*, vol. 110, 8 2013.

- [116] R. Zeineddine and J. J. Yerbury, “The role of macropinocytosis in the propagation of protein aggregation associated with neurodegenerative diseases,” *Frontiers in Physiology*, vol. 6, no. OCT, p. 277, 2015.
- [117] J. P. Lim and P. A. Gleeson, “Macropinocytosis: An endocytic pathway for internalising large gulps,” *Immunology and Cell Biology*, vol. 89, pp. 836–843, 11 2011.
- [118] “R<0> values for some Alexa Fluor dyes—Table 1.6 | Thermo Fisher Scientific - NL.”
- [119] M. Ciarlet, S. E. Crawford, and M. K. Estes, “Differential Infection of Polarized Epithelial Cell Lines by Sialic Acid-Dependent and Sialic Acid-Independent Rotavirus Strains,” *Journal of Virology*, vol. 75, pp. 11834–11850, 12 2001.

## Appendices

### Appendix A: Sequence of $\alpha$ -Synuclein

Human	1	MDVFMKGLSKAKEGVVAAAEKTKQGVAAEAGKTKEGVLYVGSKTKEGVVHGVA	TVAE	TK	60
Pig	1	.....	T	.....	60
Cow	1	.....R.....	T	.....	60
Fish	1	.....	T	.....	56
Chicken	1	.....N.....R.....	T	.....	60
Human	61	EQVTNVGGAVVTGVTAVAQKTVEGAGSIAAATGFV			95
Pig	61	.....E.....		G	95
Cow	61	.....E.....		G	95
Fish	57	.....			91
Chicken	61	...S.....N.....L.			95
Human	96	KKDQLGK-NEEGAPOEGIL---E--D--MPVDPDNEAYEMPSEEGYQDYEP			140
Pig	96	.....-.....-.....-.....			140
Cow	96	...HM..-G...S.....-.....-.....			140
Fish	92	.....-.....-.....-.....			125
Chicken	96	.....A.Q....FL...MV---NNT.--I...E.....P..E.....			143

Figure A1: Amino acid sequence of human  $\alpha$ -Syn and  $\alpha$ -Syn of several animals consumed by humans. The red box indicates residue 53, where human  $\alpha$ -Syn contains alanine and  $\alpha$ -Syn of several animals threonine. Sequences retrieved from NCBI.

Appendix B: Confluence of Caco-2 cell layer on different seeding days

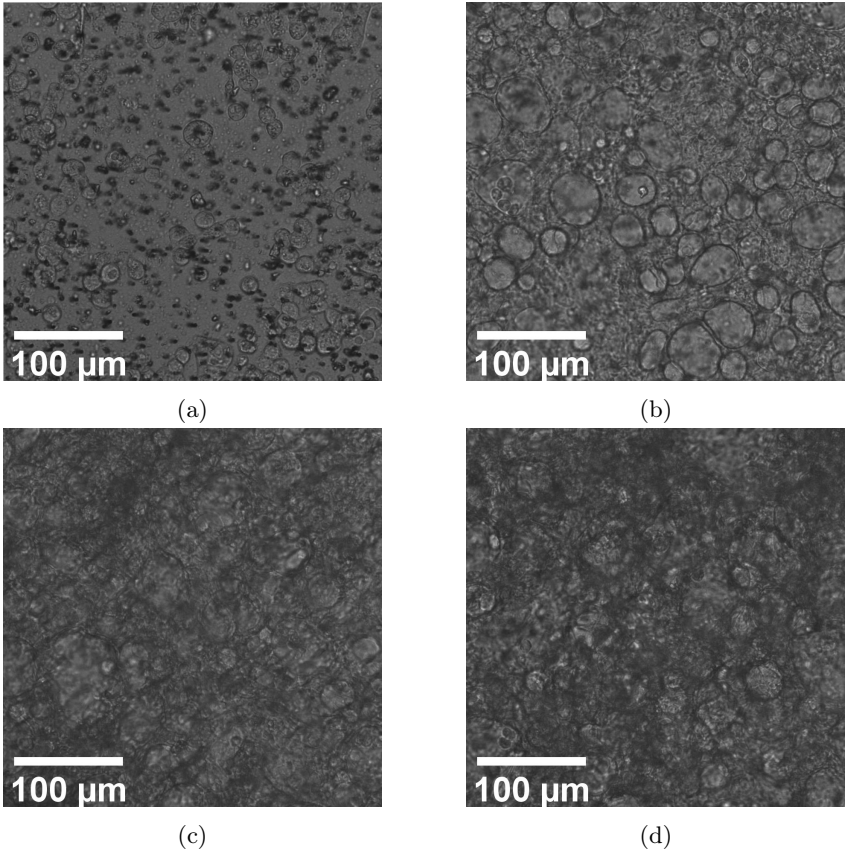


Figure B1: Wide field images of transwell membrane with Caco-2 cells cultured for (a) 1 day, (b) 7 days, (c) 14 days and (d) 21 days.

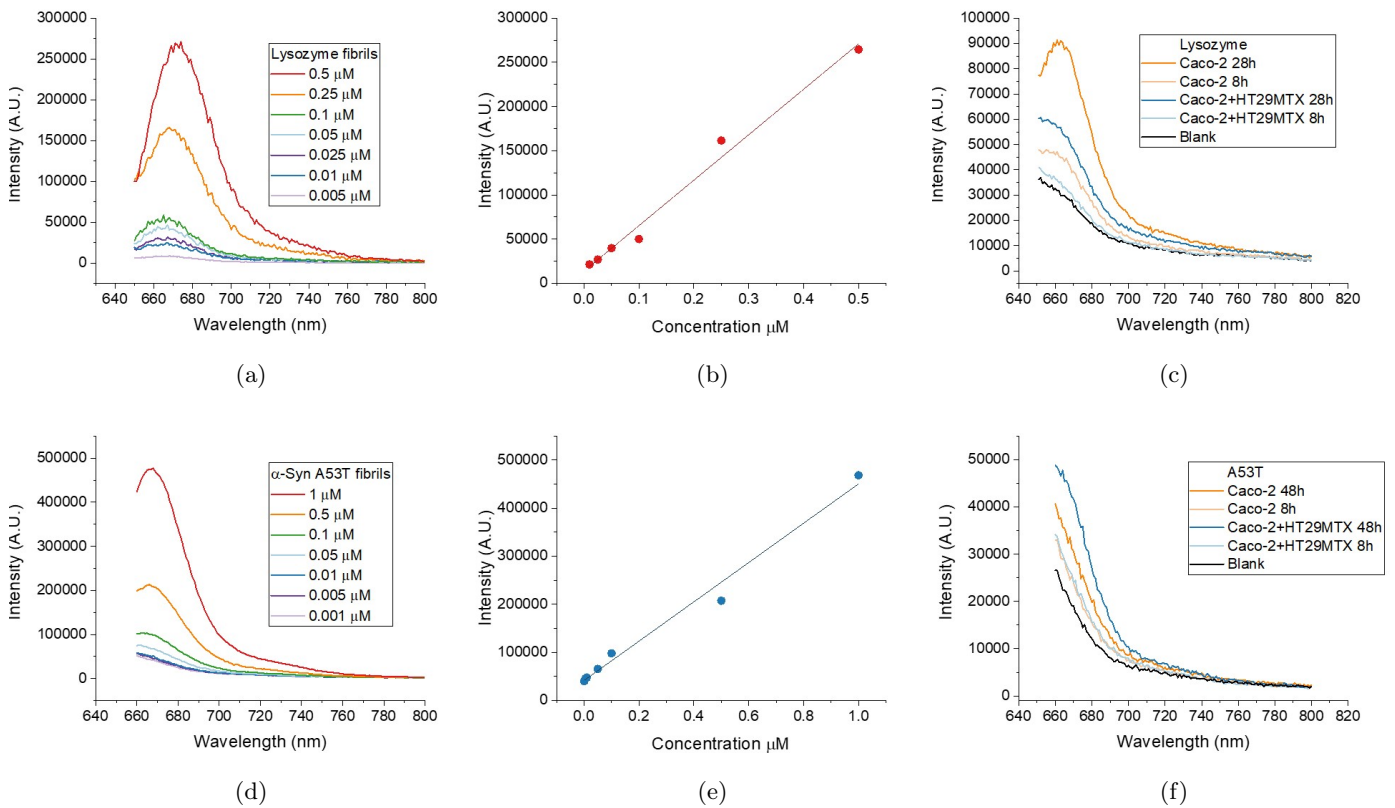
Appendix C: Emission spectra lysozyme and  $\alpha$ -Syn A53T fibrils

Figure C1: (a) and (d) Emission intensity graphs of calibration where (a) is for lysozyme and (d) is for  $\alpha$ -Syn A53T. (b) and (e) Emission intensity at 669 nm from Figure (a) and (d) where (b) is for Lysozyme and (e) for  $\alpha$ -Syn A53T. (c) and (f) Examples of increase in emission intensity in the basolateral compartment in the cell models, with (c) for lysozyme and (f) for  $\alpha$ -Syn A53T.  $R^2$  of calibration of emission intensity of lysozyme was 0.98 and for  $\alpha$ -Syn A53T 0.99.

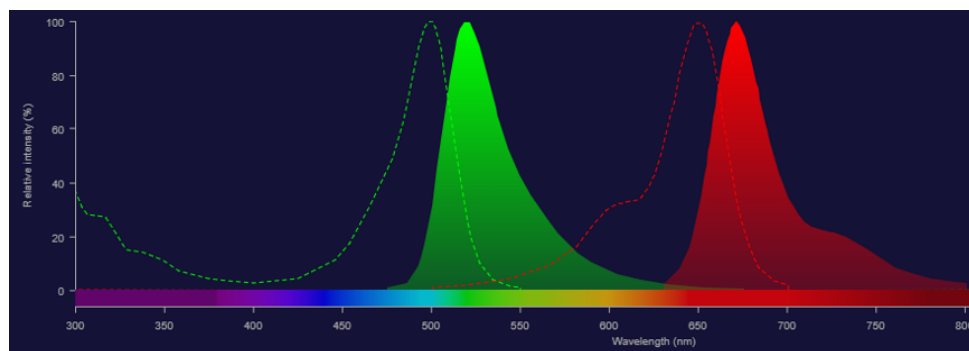
**Appendix D: Excitation and emission spectra AF488 and AF647**

Figure D1: Excitation (dashed line) and emission (solid) spectra AF488 (green) and AF647 (red)